BOR DERGİSİ
JOURNAL OF BORON
https://dergipark.org.tr/boron

İÇİNDEKİLER/CONTENTS

BORON 5(4), 163 - 169, 2020

BOR DERGiSi

JOURNAL OF BORON

https://dergipark.org.tr/boron

Mechanical and thermal properties of boric acid and paper mill sludge reinforced polyester composites

Hacı İbrahim Çeliker[1], Ahmet Çetin Başbozkurt[2], Ali Yaraş[3*]

[1]Bartin University, Department of Metallurgy and Material Engineering, 74100, Bartin, Turkey
ORCID ID orcid.org/0000-0002-8130-0931
[2]Bartin University, Department of Metallurgy and Material Engineering, 74100, Bartin, Turkey
ORCID ID orcid.org/0000-0002-9794-6235
[3]Bartin University, Department of Metallurgy and Material Engineering, 74100, Bartin, Turkey
ORCID ID orcid.org/ 0000-0003-1725-7788

ARTICLE INFO

Article history:
Received March 11, 2020
Accepted October 28, 2020
Available online December 29, 2020

Research Article

DOI: 10.30728/boron.702466

Keywords:
Boric acid,
Mechanical property,
Paper mill sludge,
Polymer composite,
Thermal insulation.

ABSTRACT

This study is aimed to produce polymer composite materials with low thermal conductivity coefficient and high mechanical strength. Therefore, different rates of boric acid and paper mill sludge were added to the polyester matrix and the composite materials were characterized in terms of mechanical and thermal properties. Based on the experimental results, the highest bending strength (21.83 MPa) was achieved in the presence of 5% paper mill sludge and 3% boric acid. Compared to the reference, the decomposition temperatures of composites increased with the addition of additives. Also, the densities of composites ranged from 1.141 g/cm^3 and 1.409 g/cm^3. The additives of paper mill sludge and boric acid decreased the thermal conductivity coefficient of composites and lowest coefficient of thermal conductivity was reported as 0.61 W/mK. Consequently, boric acid and paper mill sludge additions enhance the mechanical and thermal properties of polyester-based composite material.

1. Introduction

Polymeric composite materials are produced with different fibers and particles to improve the mechanical and thermal properties of polymers which have a wide usage area. In this context, there are many studies on the polymer properties by fiber and particle reinforcement in the literature [1-5]. For instance, boron nitride was added to polypropylene and boron nitride addition was found to increase the thermal conductivity of polypropylene [6]. In another study, weight loss of epoxy composites with different ratios of boric acid (H_3BO_3) was investigated [7]. Polymers have very low thermal conductivity values when compared to many other materials [8]. Improving the thermal conductivity properties of polymers may result in greater energy savings, especially in thermal insulation applications. In this study, H_3BO_3 was used to reduce the thermal conductivity coefficient of polymer material.

In paper manufacturing plants, some of the cellulose fiber and mineral additives are collected in tailings impoundments during production process and are called paper mill sludge (PMS). It is a problem both in terms of environment and factory economy. Therefore, paper manufacturers are making great efforts to solve this problem and evaluate it in different applications. Nowadays, PMS is either landfilling or disposed of by incineration treatment [9]. Researchers have focused on alternative methods due to the decrease of landfills, increasing storage costs, and because of no sustainable and eco-friendly of the incineration method [10,11].

PMS can also be used as filler in polymers because of containing kaolin, talc and calcium carbonate as well as cellulose fibers. Within the scope of material technologies, the studies on the utilization of cellulosic and inorganic materials in polymer composites are remarkable [12]. When viscose fiber and microcrystalline cellulose particles are added to the high density polyethylene, it is stated that cellulose has a clear effect on the thermal dimensional stability of polyethylene and the addition of viscose fiber and microcrystalline cellulose increases the tensile strength of polyethylene [13]. PMS and wood fibers are reinforced into polyethylene matrix in different rates. While there was no significant change in mechanical properties at low PMS rates, the bending strength and elastic modulus of the composite material decreased and impact strength increased, after PMS ratio reached a certain value [14]. The effect of particle size of PMS and extrusion temperature on the physical and mechanical properties of thermoplastic polymer composites were investigated. In the light of the experimental findings, when particle

---

*Corresponding author: aliyaras@bartin.edu.tr

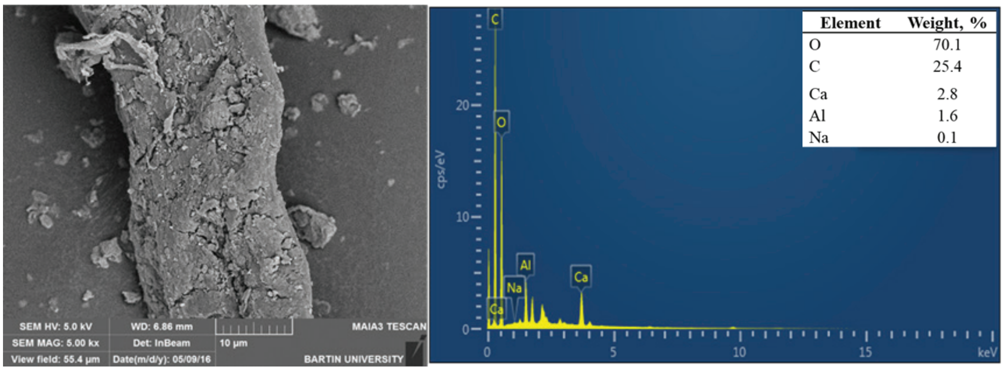

Element	Weight, %
O	70.1
C	25.4
Ca	2.8
Al	1.6
Na	0.1

Figure 1. SEM image and EDS results of paper mill sludge.

size decreased, swelling, water absorption, tensile and bending strengths of composite material improved and increase in extrusion temperature positively affected tensile and bending properties [15].

Energy saving has become a more critical subject for economic and environmental reasons. The total energy consumed in Turkey are known for use in buildings of 32%, about half of it is lost due to insufficient insulation of buildings. Therefore, the insulation of building walls is open to new studies as it enables energy saving [16]. Although there are many studies present in literature regarding to production and characterization of polyester composite materials, no study has been issued about the use of PMS as an additive in polyester polymer. In addition, the characterization of the material in terms of thermal conductivity will make an important contribution to the literature. Therefore, in present paper, it was planned to produce polymer composites with low thermal conductivity and high mechanical strength by adding H_3BO_3 and PMS to polyester matrix. The produced composite materials were characterized in terms of bending strength and thermal degradation, thermal conductivity coefficient and surface properties.

2. Materials and methods

2.1. Material properties

PMS was provided from OYKA paper and packaging factory in Caycuma/Zonguldak. It was dried to remove moisture at 110°C for 6 h and then grinded. PMS was coated with Au-Pd mixture and then SEM-EDS analysis was performed (Tescan Maia3 Xmu). SEM image and EDS results of PMS are presented in Figure 1. It is known that PMS contains a large amount of cellulose. Also, there are also impurities in PMS such as Ca and Al arising from the paper manufacturing process. Polyester based epoxy resin used as polymer matrix and H_3BO_3 of analytical purity were purchased from a commercial company.

TG-DTG curves of PMS are presented in Figure 2. TG-DTG analysis was carried out at 10°C/min. of heating rate under nitrogen atmosphere (Hitachi, STA 7300). At the end of 800°C, the total weight loss is 69.56%. Thermal degradation of PMS took place in three stages. A weight loss of approximately 3% occurred due to the removal of physical water until 150°C. At 160-600°C, 61.35% weight loss was observed with the thermal degradation of hemicellulose and cellulose. At the last stage (>600°C), the weight loss is 69.56% due to calcination of carbonates. As shown in Table 1, functional groups of PMS were also determined by FTIR analysis.

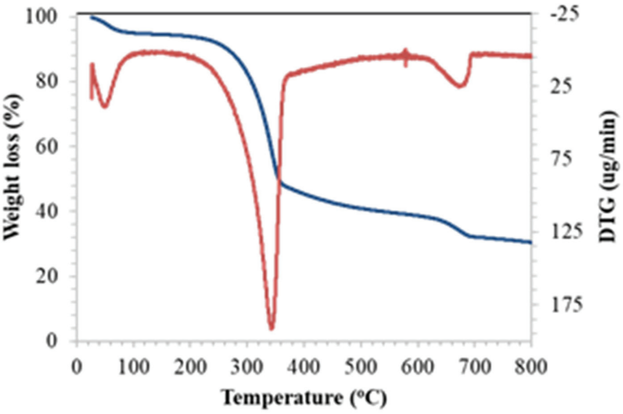

Figure 2. TG-DTG curves of paper mill sludge.

2.2. Composite material production and characterization

Composite material production was carried out using molds with dimensions of 15 cm x 4 cm x 4 cm. Samples were prepared according to the mixture ratios in Table 2. The catalyst (Butanox N60) of 1% was added to the mixtures to accelerate the chemical reaction. Lubricant (wax) was applied to the inner surfaces of the mold for easy removal of the sample. The stirring treatment was performed to ensure homogeneity of the prepared mixtures by a mechanical stirrer. Then, the prepared mixtures were molded and the samples were removed from the mold after being kept at ambient conditions for 1 h. Samples were cut on a cutting machine and brought to the appropriate dimensions for three-point flexural strength tests. All characterization experiments were carried out in triplicate.

Table 1. FTIR analysis of paper mill sludge.

Wavenumber (cm^{-1})	Functional group
3331	-OH stretching of cellulose
2918, 2850	C-H stretching of aromatic and aliphatic groups
1640	C-O (aldehyde group)
1417	calcium carbonate
1155	vibrations of C-O-C bond
1028	glucose stretching of C-O and OH
873	C-O-C bond

Table 2. Mixture ratios of prepared samples.

Sample	Polyester resin (wt. %)	PMS (wt. %)	Boric acid (wt. %)
Reference	100	-	-
A1	99	1	-
A2	97	3	-
A3	95	5	-
B1	99	-	1
B2	98	-	2
B3	97	-	3
C1	98	1	1
C2	95	3	2
C3	92	5	3

Three-point bending tests of the samples were performed using a test instrument (Universal) with a capacity of 50 kN. All tests were carried out under the test conditions of effective span of 50 mm and loading speed of 1 mm/s. The molded samples were cut to 50 mm x 20 mm x 20 mm and prepared for bending test. The samples were placed between the two supports. Then, tests were carried out until fracture occurred with the effect of an increasing force and three-point bending strength of composite materials was determined. The thermal behaviors of the composite materials were carried out using thermogravimetric analyzer (Hitachi STA 7300) at heating rate of 10°C/min under nitrogen atmosphere. Thermal conductivity values of the composite materials were measured at ambient temperature by a C-Therm TCi Thermal Conductivity Analyzer with modified transient plane source. The surface of the material was made flat and smooth for measurement. Then, the material surface was contacted with the sensor and the thermal conductivity coefficient (k) of the material is determined in W/mK units.

3. Results and discussion

3.1. Three-point bending tests

The bending test results are given in Figures 3-5. As seen in Figure 3, the bending strength of the polymer composites increased with PMS addition and the highest bending strength (11.53 MPa) was achieved in composite material containing 5% of PMS. It is possible to indicate that the presence of cellulosic fibers in PMS increases the strength of the polymer matrix. In literature, while the flexural strength of polyamide 6 based composites increased with the addition of carbon and glass fiber (from 1% to 5%), carbon fiber resulted in higher strength [17]. Another study indicates that the mechanical performance of the composite improves, as the broom grass fiber content in the polyester matrix increases. This is because the polyester matrix transmits and distributes the applied force to the fibers. Therefore, the composite material exhibits higher strength and can withstand a higher load than pure polyester [18,19].

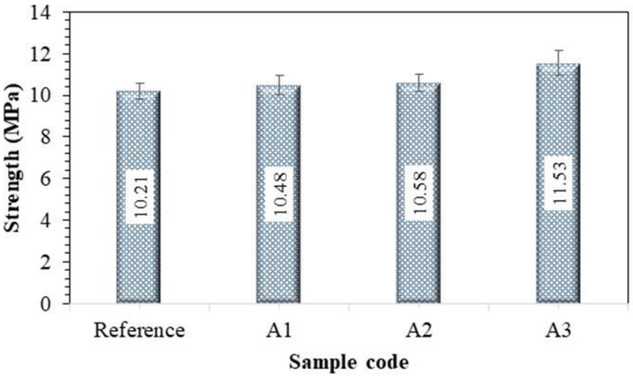

Figure 3. Effect of paper mill sludge amount on bending strength.

As shown in Figure 4, addition of H_3BO_3 up to 2% increased the bending strength, a decrease in the bending strength of the material occurred at higher concentrations. Accordingly, while the composite material containing 2% H_3BO_3 has the maximum strength of (16.64 MPa), it decreased to 14.01 MPa for the material with 3% H_3BO_3. Demirel et al. [20] added different amounts of H_3BO_3 (15%, 20% and 30%) to the polyester mixture containing 5% glass fiber. They reported that the mechanical strength of composites tended to decrease compared to pure polyester at the amount of H_3BO_3 studied. In the present article, lower amounts of H_3BO_3 were studied. And, an increase was observed up to 2%, while a partial decrease was observed in 3% H_3BO_3 addition. Similar trend in terms of mechanical strength was observed for all series of B and C.

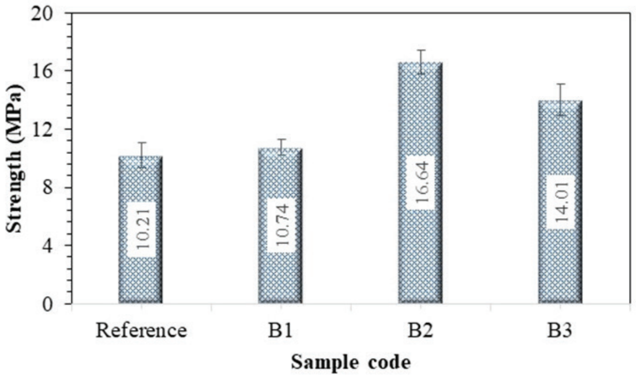

Figure 4. Effect of boric acid amount on bending strength.

According to Figure 5, the flexural strength increased to 21.83 MPa with the addition of 5% PMS and H_3BO_3 while the bending strength of the reference sample (no additive) was 10.21 MPa. However, the bending strength of the material containing 8% PMS and H_3BO_3 was reduced to 14.88 MPa. This is due to the change in the adhesion forces between the additives and the polyester. Consequently, the combined utilization of PMS and H_3BO_3 up to certain amount leads to a significant increase in bending strength. This suggests that PMS and H_3BO_3 can be evaluated to improve the mechanical properties of polyester composite materials. Another important point in bending tests is that the fracture occurs as brittle fracture. Digital images of fractured samples are given in Figure 6.

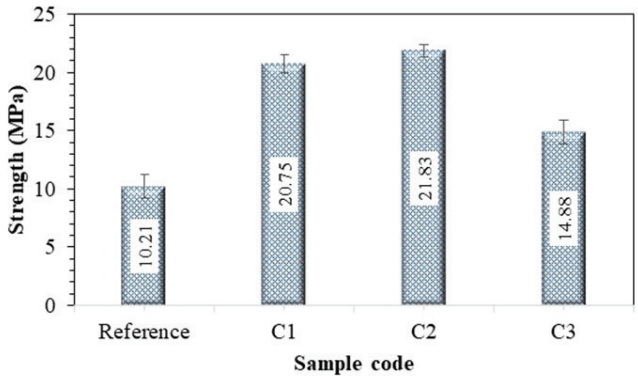

Figure 5. Effect of paper mill sludge and boric acid amount on bending strength.

Density of polyester material is 1.076 g/cm^3. The density of composites varies between 1.141 g/cm^3 and 1.409 g/cm^3. The densities of composites containing 1%(A1), 3%(A2) and 5%(A3) PMS were measured as 1.141, 1.158 and 1.198 g/cm^3, respectively. Also, the densities of samples with 1%(B1), 2%(B2) and 3%(B3) H_3BO_3 additives are 1.312, 1.348 and 1.392 g/cm^3, respectively. And, the samples of C1, C2 and C3 have density values of 1.341, 1.365 and 1.409 g/cm^3, respectively.

3.2. SEM analysis

SEM analyzes were performed to determine the surface morphology of the composite samples. In addition, the fracture surfaces of composite materials, the interaction between the additive and polymer matrix system and the distribution of the additives in the matrix were examined by SEM in Figure 7. The SEM image of the reference sample shows that the polyester resin is homogeneously dispersed. According to Figure 7(b), it is clearly seen that the presence of cellulosic fibers and these fibers break as a result of fracture. The lamellar occurring in different directions during the solidification and the presence of H_3BO_3 particles are shown in Figure 7(c). As seen in Figure 7(d), it is seen that the cellulose fibers are broken in the same direction as the broken polymer matrix. On the other hand, SEM images show the little polyester matrix on the surface of the broken fibers. It suggests that the adhesion between the polymer matrix and the fiber is poor [17,21].

3.3. Thermal gravimetric analysis (TGA)

Based on Figure 8, thermal degradation of the samples took place in two regions; region 1 (90°C-190°C) and region 2 (190°C-360°C). In region I, the physical water within the body is removed until 190°C temperature. The main weight loss occurred in the region II. According to DTG data, the characteristic temperatures (T_i, T_f and T_p) of DTG data for both regions are given in Table 3. Consequently, the additions of PMS and H_3BO_3 provided a relatively increased thermal resistance when compared to the reference. Similarly, the addition of H_3BO_3 (from 15% to 30%) to the polymer mixture (80% polyester and 5% glass fiber) caused an increase in the thermal decomposition temperatures of composites when compared to with pure polyester [20].

3.4. Thermal conductivity test

Based on the thermal conductivity test results in Table 4, the addition of additives caused decrease in heat conductivity coefficient. While the heat conductivity coefficient of the reference material was 0.245 W/mK, the heat conductivity coefficients of A3, B3 and C3 materials were measured as 0.212 W/mK, 0.161 W/mK and 0.209 W/mK, respectively. In literature, H_3BO_3 has been used as a reinforced material in the poly-

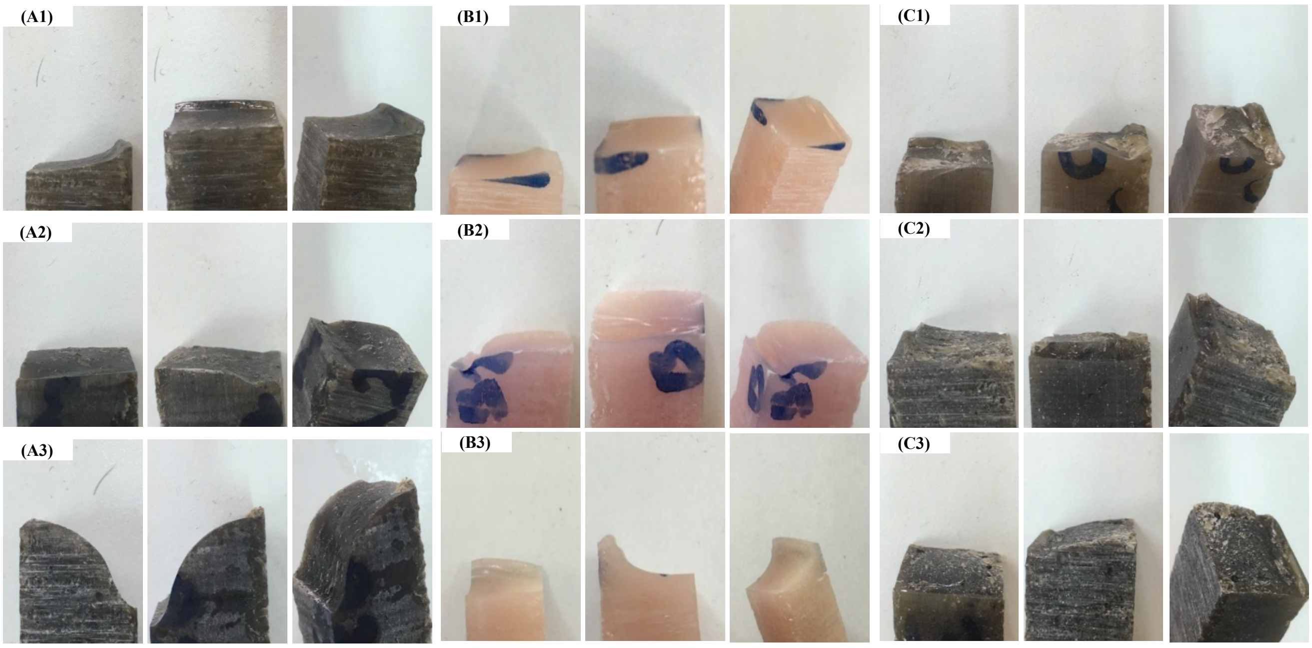

Figure 6. Digital images of the fractured surface of all samples.

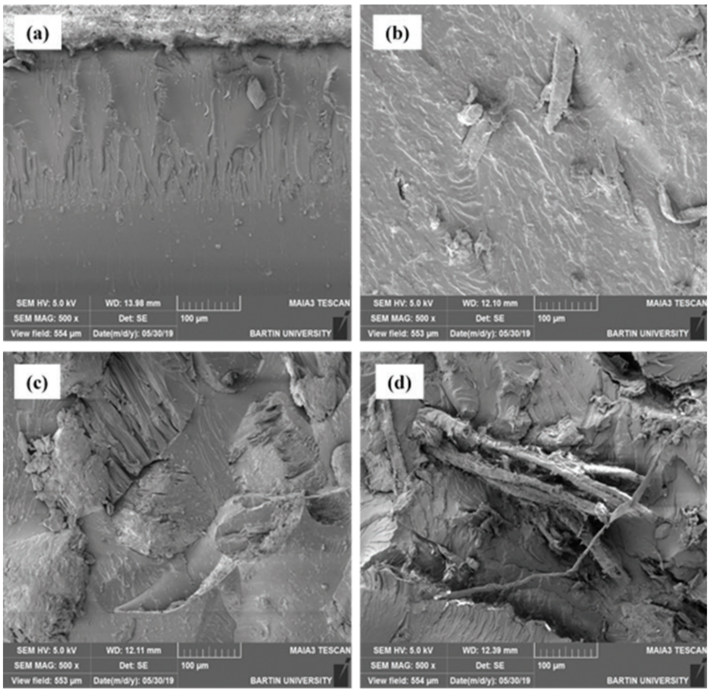

Figure 7. SEM images of fractured surfaces of samples reference (a), A3 (b), B3 (c) and C3 (d).

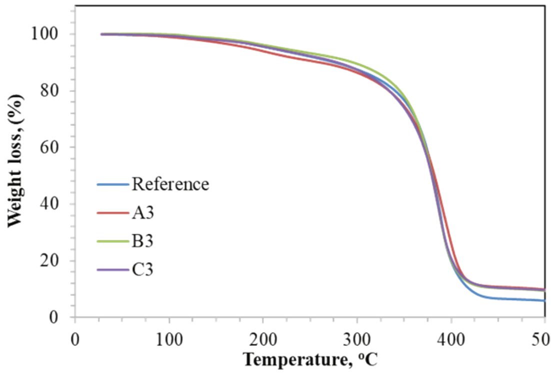

Figure 8. TGA curves of reference, A2, B3 and C3 samples.

Table 3. Characteristic peaks of thermal decomposition of reference, A3, B3 and C3.

Sample	Region I			Region II		
	T_i (°C)	T_f (°C)	T_p (°C)	T_i (°C)	T_f (°C)	T_p (°C)
Reference	80	160	125	200	295	255
A3	90	170	135	210	300	265
B3	95	175	140	215	305	270
C3	105	180	150	225	310	280

T_i = Initial temperature
T_f = Final temperature
T_p = Peak temperature

propylene matrix and improved the thermal insulation property by reducing the heat conductivity coefficient of the polymer composite material. It is attributed to the fact that the thermal conductivity of H_3BO_3 is lower than that of polypropylene [22]. In another study, thermal conductivity characteristics of polyamide 6 composites containing various fibers were investigated. The presence of carbon fiber increased the thermal conductivity of composites, however it slightly decreased with the addition of glass fiber [17]. This result shows the importance of fiber type on the thermal conductivity of composites. Also, the addition of carbon nanofillers to the epoxy polymer matrix resulted in a significant increase in thermal conductivity [23].

Table 4. Thermal conductivity coefficients of samples.

Sample	Thermal conductivity coefficient (W/mK)	Sample	Thermal conductivity coefficient (W/mK)
Reference	0.245 ± 0.008	**B2**	0.176 ± 0.024
A1	0.232 ± 0.01	**B3**	0.161 ± 0.013
A2	0.217 ± 0.021	**C1**	0.223 ± 0.013
A3	0.212 ± 0.006	**C2**	0.215 ± 0.02
B1	0.197 ± 0.017	**C3**	0.209 ± 0.018

4. Conclusions

In this study, PMS and H_3BO_3 were used as additive in polymer based composite material production and materials were characterized in terms of mechanical and thermal properties.

Based on the experimental results, the highest bending strength (21.83 MPa) was achieved in the presence of 5% PMS and 3% H_3BO_3. Compared to the reference, decomposition temperatures of composites increased with the addition of additives. Also, the densities of composites ranged from 1.141 g/cm^3 and 1.409 g/cm^3. The additives of PMS and H_3BO_3 decreased the thermal conductivity coefficient of composites and lowest coefficient of thermal conductivity was reported as 0.61 W/mK. Consequently, H_3BO_3 and PMS additions enhance the mechanical and thermal properties of polyester-based composite material.

The experimental results demonstrate the effectiveness of both H_3BO_3 and PMS in composite material production. In the following studies, we planned to use the compatibilizing agent between the polymer matrix and the additives, surface modification of PMS and the utilization of different boron compounds to achieve higher mechanical properties and further improve thermal insulation properties of the polymer composite materials.

Acknowledgement

This study was financially supported by the Scientific and Technological Research Council of Turkey (2209-A grant no: 1919B011703661).

References

[1] Zhang S., Cao X. Y., Ma Y. M., Ke Y.C., Zhang J. K., Wang F. S., The effects of particle size and content on the thermal conductivity and mechanical properties of Al_2O_3/high density polyethylene (HDPE) composites, Express. Polym. Lett., 5 (7), 581-590, 2011.

[2] Zhou W., Qi S., An Q., Zhao H., Liu N., Thermal conductivity of boron nitride reinforced polyethylene composites, Mater. Res. Bull., 42 (10), 1863-1873, 2007.

[3] Li S., Qi S., Liu N., Cao P., Study on thermal conductive BN/novolac resin composites, Thermochim. Acta, 523 (1-2), 111-115, 2011.

[4] Wang M., Kang Q., Pan N., Thermal conductivity enhancement of carbon fiber composites, Appl. Therm. Eng., 29 (2-3), 418-421, 2009.

[5] Naficy S., Garmabi H., Study of the effective parameters on mechanical and electrical properties of carbon black filled PP/PA6 microfibrillar composites, Compos. Sci. Technol., 67 (15-16), 3233-3241, 2007.

[6] Tekce H. S., Kumlutas D., Tavman I. H., Effect of particle shape on thermal conductivity of copper reinforced polymer composites, J. Reinf. Plast. Compos., 26 (1), 113-121, 2007 (in Turkish).

[7] Cheewawuttipong W., Fuoka D., Tanoue S., Uematsu H., Iemoto Y., Thermal and mechanical properties of polypropylene/boron nitride composites, Energy Procedia, 34, 808-817, 2013.

[8] Visakh P. M., Nazarenko O. B., Amelkovich Y. A., Melnikova T. V., Thermal properties of epoxy composites filled with boric acid, IOP Conf. Ser.: Mater. Sci. Eng., 81, 12095, 2015.

[9] Scott G. M, Smith A., Sludge characteristics and disposal alternatives for the pulp and paper industry. TAPPI Int. Environ. Conf., Atlanta-A.B.D., 269, 1995.

[10] Dorris G. M., The physical characterization of hydrated reburned lime and lime mud particles, J. Pulp Pap. Sci., 19 (6), 256-267, 1993.

[11] Bajpai P., Biokraft pulping of eucalyptus with selected lignin-degrading fungi, J. Pulp Pap. Sci., 27 (7), 235-239, 2001.

[12] Küçükdoğan N., Halis S., Sütçü M., Sarıkanat M., Seki Y., Sever K., Kağıt üretim atığı katkılı yüksek yoğunluklu polietilen (yype) kompozitlerin mekanik özelliklerinin incelenmesi, PAJES, 23 (8), 949-953, 2017.

[13] Pöllänen M., Suvanto M., Pakkanen T. T., Cellulose reinforced high density polyethylene composites-Morphology, mechanical and thermal expansion properties, Compos. Sci. Technol., 76, 21-28, 2013.

[14] Huang H. B., Du H. H., Wang W. H., Shi J. Y., Characteristics of paper mill sludge-wood fiber-high-density polyethylene composites, Polym. Compos., 33 (9), 1628-1634, 2012.

[15] Son J., Kim H., Lee P., Role of paper sludge particle size and extrusion temperature on performance of paper sludge-thermoplastic polymer composites, J. Appl. Polym. Sci., 82 (11), 2709-2718, 2001.

[16] Akkurt S., Sütçü M., Başoğlu K., Isı yalıtım özellkleri iyileştirilmiş yapı tuğlalarının geliştirilmesinde kağıt üretim atıklarının kullanılması etkileri, X. Ulusal Tesisat Mühendisliği Kongresi, İzmir-Türkiye, 899-908, 13-16 Nisan 2011.

[17] Li M., Wan Y., Gao Z., Xiong G., Wang X., Wan C., Luo H., Preparation and properties of polyamide 6 thermal conductive composites reinforced with fibers, Mater. Des., 51, 257-261, 2013.

[18] Rao K. M. M., Rao K. M., Prasad A. V. R., Fabrication and testing of natural fibre composites: Vakka, sisal, bamboo and banana, Mater. Des., 31 (1), 508-513, 2010.

[19] Ramanaiah K., Prasad A. V. R., Reddy K. H. C., Thermal and mechanical properties of waste grass broom fiber-reinforced polyester composites, Mater. Des., 40, 103-108, 2012.

[20] Demirel M., Pamuk V., Dilsiz N., Investigation of flame retardancy and physical-mechanical properties of zinc borate/boric acid polyester composites, J. Appl. Polym. Sci., 115 (5), 2550-2555, 2010.

[21] Li J., Cai C. L., The carbon fiber surface treatment and addition of PA6 on tensile properties of ABS composites, Curr. Appl. Phys., 11 (1), 50-54, 2011.

[22] Pehlivanlı Z. O., H_3BO_3/PP kompozitlerinin ısı iletim katsayılarının incelenmesi, Gazi Üniversitesi Fen Bilim. Derg. Part C Tasarım ve Teknol., 4 (3), 91-96, 2016.

[23] Yang S. Y., Lin W. N., Huang Y. L., Tien H. W., Wang J. Y., Ma C. C. M., Li S. M., et al., Synergetic effects of graphene platelets and carbon nanotubes on the mechanical and thermal properties of epoxy composites, Carbon, 49 (3), 793-803, 2011.

BORON 5 (4), 170 - 175, 2020

BOR DERGİSİ
JOURNAL OF BORON
https://dergipark.org.tr/boron

Leaching behaviour of lithium, cesium and rubidium from a clay sample of Kırka borate deposit in sulfuric acid solutions

Abdullah Obut[1*], İlhan Ehsani[2], Zeynep Aktosun[3], Abdulkerim Yörükoğlu[4], İsmail Girgin[5], Abidin Temel[6], Hacı Deveci[7]

[1]Hacettepe University, Mining Engineering Department, 06800, Ankara, Turkey, ORCID ID orcid.org/0000-0003-2979-322X
[2]Hacettepe University, Mining Engineering Department, 06800, Ankara, Turkey, ORCID ID orcid.org/0000-0001-9741-8777
[3]Boron Research Institute, 06530, Ankara, Turkey, ORCID ID orcid.org/0000-0001-9019-0183
[4]Boron Research Institute, 06530, Ankara, Turkey, ORCID ID orcid.org/0000-0003-3194-3901
[5]Boron Research Institute, 06530, Ankara, Turkey, ORCID ID orcid.org/0000-0002-7611-9070
[6]Hacettepe University, Geological Engineering Department, 06800, Ankara, Turkey, ORCID ID orcid.org/0000-0002-8051-4065
[7]Karadeniz Technical University, Mining Engineering Department, 61080, Trabzon, Turkey, ORCID ID orcid.org/0000-0003-4105-0912

ARTICLE INFO

Article history:
Received June 24, 2020
Accepted October 30, 2020
Available online December 29, 2020

Research Article

DOI: 10.30728/boron.757308

Keywords:
Cesium,
Kırka borate deposit,
Lithium,
Rubidium,
Sulfuric acid leaching.

ABSTRACT

In this study, the leaching behaviour of lithium, together with cesium and rubidium, from a clay sample of Kırka borate deposit in sulfuric acid solutions was investigated with chemical, XRD, FTIR, DTA analyses methods and specific surface area measurements. It was observed that the leaching behaviours of lithium, cesium and rubidium were quite similar in character in that their extent of leaching tended to improve with increasing sulfuric acid concentration, especially in the range of 0.1 to 2 mol·dm^{-3}, at the highest leaching temperature of 363 K. Further increase of the acid concentration to 4 mol·dm^{-3} H_2SO_4 appeared to have a limited improvement in their extent of leaching. Under the optimum conditions, 2 mol·dm^{-3} H_2SO_4 concentration and 363 K leaching temperature, the leaching ratios reached for lithium (Li), cesium (Cs) and rubidium (Rb) were 97.2%, 83.7% and 65.2%, respectively. The results of XRD, FTIR and DTA analyses applied to the clay sample and the leaching residue obtained after leaching of the clay sample under the optimum conditions collectively showed that almost complete destruction of crystalline smectite structure(s) in the clay sample caused by acid leaching resulted in the formation of amorphous silica phase in the leaching residue. During this transformation, as expected, the specific surface area of the clay sample increased, from 59 to 406 m^2/g. The results obtained in this preliminary study may be exploited for the treatment of very high tonnages of clay containing processing waste of Kırka boron plant as potential Li (Cs and/or Rb) resource.

1. Introduction

Lithium (Li), as the lowest density metal (0.534 g/cm^3), is the 25th most abundant (20 mg/kg) element in the earth's crust and does not occur free in nature. It is used extensively in batteries, glasses and ceramics, lubricants, and also used in metallurgical and nuclear industries. Recently, the academic and industrial interest in Li has significantly increased because of the ever-increasing demand for electric/hybrid vehicles, power storage systems and smart devices (phones, tablets, computers) that use rechargeable Li-ion batteries, which have unique high specific energy densities (100-265 W·h/kg) and life span cycles (400-1200). On the other hand, primary Li production is mostly done from two natural sources, e.g. pegmatite deposits and salt-lake brines, and therefore, diversification of Li resources is particularly important for meeting the increasing demand for Li in the battery industry around the world [1-8].

Although economically no exploitable Li resources are present in Turkey, there are some lakes (up to 325 mg·dm^{-3} Li) and clays (0.17-0.58% Li_2O, in different borate deposits) containing noticeable amounts of Li [9]. There appear a few studies on the leaching of Li from the clays of the Kırka borate deposit in acid solutions. Mordoğan et al. [10] investigated the leaching of Li from the ulexite zone clay sample (with 0.56% Li_2O) of the Kırka borate deposit containing dolomite, montmorillonite and hectorite in sulfuric acid (up to about 3.26 mol·dm^{-3} H_2SO_4) solutions. They found that the leaching of Li improved with increasing the acid concentration and the Li leaching ratio of about 92% was achieved at an acid concentration of approximately 1.63 mol·dm^{-3} H_2SO_4. They also demonstrated

---

*Corresponding author: aobut@hacettepe.edu.tr the beneficial effect of increasing the temperature from 293 K to 353 K on the rate and extent of leaching of Li, i.e. leaching ratio of over 90% Li was reached at 353 K compared with about 65% at 293 K within the same period of leaching time (0.5 hour). These investigators also noted that acid leaching was not particularly selective for Li dissolution (99%) with a substantial dissolution of iron (42.97%), magnesium (58.10%) and calcium (35.04%) under the optimum conditions of leaching. On the other hand, Lee et al. [11] reported a leaching ratio of 89% for Li from a smectitic clay sample (having 0.39% Li_2O) of the Kırka borate deposit in 0.25 mol·dm^{-3} hydrochloric acid solution for 10 hours of leaching time. Earlier studies [10,11] appear to focus essentially on the leaching of Li and the other components such as cesium (Cs) and rubidium (Rb) mostly being overlooked. In this regard, Baydır and Erdoğan [12] studied the extraction of Rb from the montmorillonite waste sample (containing >1000 μg/g Rb) of the Kırka deposit in hydrochloric and nitric acid solutions and they observed that Rb could not be leached to the desirable extent in solutions of up to 1 mol·dm^{-3} HCl or HNO_3 concentration.

In this study, the leaching behaviour of Li, together with Cs and Rb, from a clay sample (1.28% Li_2O) of the Kırka borate deposit in aqueous H_2SO_4 solutions was investigated in order to collect new data for possible hydrometallurgical processing of clay containing processing waste of the Kırka boron plant. The hand-picked clay sample from the Kırka borate deposit was used to determine the leaching behaviour of Li as well as Cs and Rb from the clay sample in sulfuric acid solutions. Furthermore, the characterization of the sample, as well as the leaching residue, was carried out to provide an insight into the leaching peculiarities of the clay sample.

2. Materials and methods

A light-green coloured clay sample taken from the Kırka borate deposit (Eskisehir, Turkey) was used in the leaching experiments after grinding in a mortar. The particle size distribution (Malvern Mastersizer 3000) of the ground sample showed that 80% and 100% passing sizes of the sample were 17 μm and 76 μm, respectively (Figure 1). The chemical composition of the ground sample, determined by XRF analysis (AcmeLabs, Bureau Veritas), was given in Table 1. In addition, Cs and Rb (by Perkin Elmer ELAN 9000 ICP-MS) contents of the sample were also determined as 544 and 179 mg/kg, respectively.

The XRD (Panalytical Empyrean, CuKα radiation, measured after equilibrating with room atmosphere) patterns of the whole-rock (Figure 2) and the clay fractions (Figure 3) of the sample, which were prepared according to Gündoğdu and Yılmaz [13], have indicated that the sample is composed predominantly of smectite group clay mineral(s) and contained feldspar as the impurity. The very small intensity peak at about 1.00 nm, observed especially in the XRD patterns of air-dried and glycolated clay fractions, may be an indication of the presence of different clay mineral(s) in the studied sample.

A representative leaching experiment was started by the addition of a calculated amount of clay sample into a 250 cm^3 Pyrex reactor containing aqueous sulfuric acid solution at the pre-determined concentration and the temperature. The leaching experiment continued for one hour under constant speed magnetic stirring to keep all solid particles in suspension. The leaching

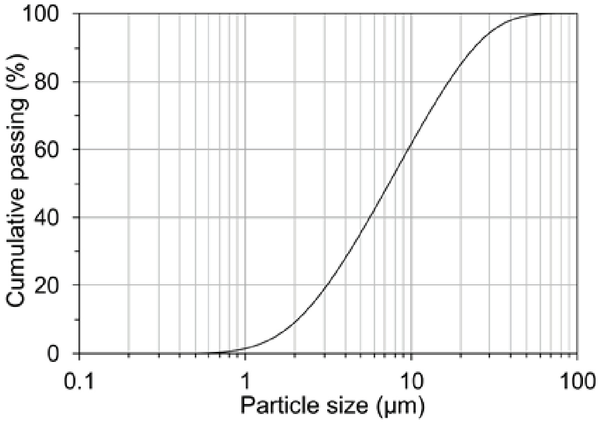

Figure 1. The particle size distribution of the sample.

Table 1. The chemical composition (wt.-%) of the sample.

Component	Chemical Composition (wt.-%)	Component	Chemical Composition (wt.-%)
SiO_2	60.58	**SrO**	0.59
Al_2O_3	14.91	**Na_2O**	0.49
MgO	7.82	**B_2O_3 $^{a)}$**	0.35
K_2O	2.73	**TiO_2**	0.16
Fe_2O_3	2.50	**P_2O_5**	0.02
Li_2O $^{a)}$	1.28	**MnO**	0.01
CaO	1.25	**L.O.I. $^{b)}$**	7.50

$^{a)}$ by Thermo Scientific iCAP 7000 ICP-OES
$^{b)}$ Loss on ignition

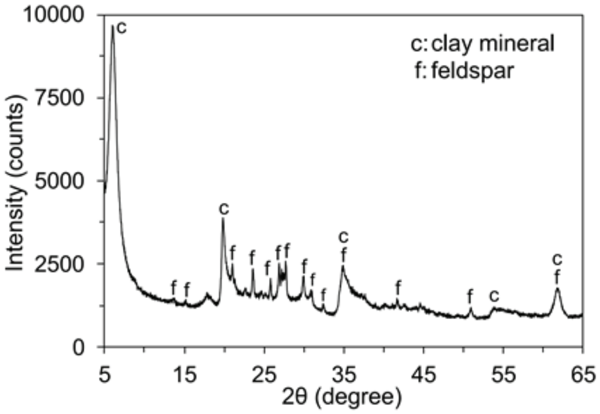

Figure 2. The whole-rock XRD pattern of the sample.

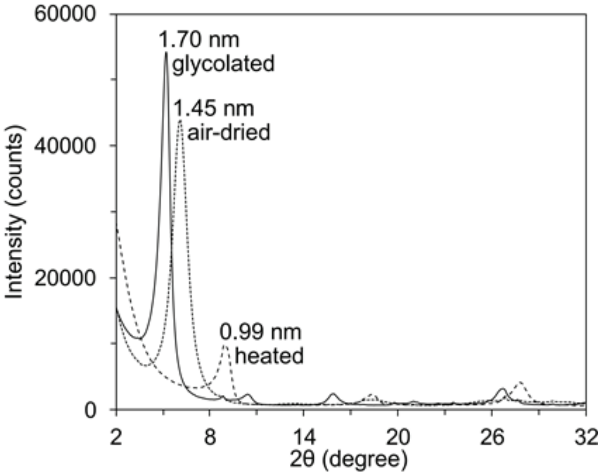

Figure 3. The XRD patterns of clay fractions of the sample.

conditions, i.e. acid concentration (0.1, 1, 2 and 4 mol·dm^{-3} H_2SO_4), temperature (298, 323 and 363 K), leaching time (1 h) and solid/liquid ratio (1 g/10 cm^3), were selected according to the findings in preliminary tests and previous studies in the literature [10,14,15]. After the completion of a leaching experiment, the solid leaching residue was separated from the loaded leaching solution, which was analyzed for Li, Rb and Cs to reveal the leaching behaviours of these metals from the studied clay sample. In addition, the XRD patterns (Panalytical Empyrean, CuKα radiation, measured after equilibrating with room atmosphere), the B.E.T. specific surface areas (Quantachrome Autosorb-1, by nitrogen adsorption following degassing for 2 hours at 378 K), the FT-IR spectra (Varian 660-IR, KBr pellet method) and the DTA curves (Setaram Labsys, under static air atmosphere at a heating rate of 0.167 K/s, measured after equilibrating with room atmosphere) of the clay sample and the leaching residue were also determined to provide an insight into the leaching behaviour of the clay sample in sulfuric acid solutions.

3. Results and discussion

The effects of sulfuric acid concentration on the leaching ratios of Li, Cs and Rb were given in Figures 4 to 6, respectively. As shown in Figures 4 to 6, the lowest leaching ratios of these metals were obtained at the lowest leaching temperature tested (298 K). Increasing the temperature from 298 K to 323 K improved their leaching from the sample and the highest leaching ratios were obtained at the highest leaching temperature of 363 K. The leaching ratio of Li, which is probably present in crystal structure of the smectite component of the sample according to Mordoğan et al. [10] and Lee et al. [11], increased substantially from 3.4 to 97.2% with increasing acid concentration from 0.1 to 2 mol·dm^{-3} H_2SO_4 at 363 K. Almost complete leaching of Li (99.7%) from the clay sample was achieved in 4 mol·dm^{-3} H_2SO_4 solution at 363 K. A similar leaching behaviour in character with positive influence of increasing acid concentration was also observed for Cs and Rb at 363 K. The leaching ratios of Cs and Rb varied from 83.7% for Cs and 65.2% for Rb in 2 mol·dm^{-3} H_2SO_4 solution to 92.4% for Cs and 68.9% for Rb in 4 mol·dm^{-3} H_2SO_4 solution at 363 K. Based on these leaching data, 2 mol·dm^{-3} H_2SO_4 concentration and 363 K leaching temperature were selected as the optimum conditions for dissolution of these metals from the clay sample.

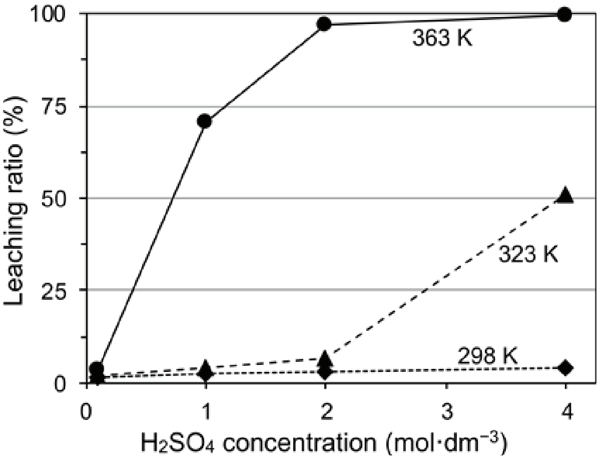

Figure 4. The effects of sulfuric acid concentration on the leaching of lithium.

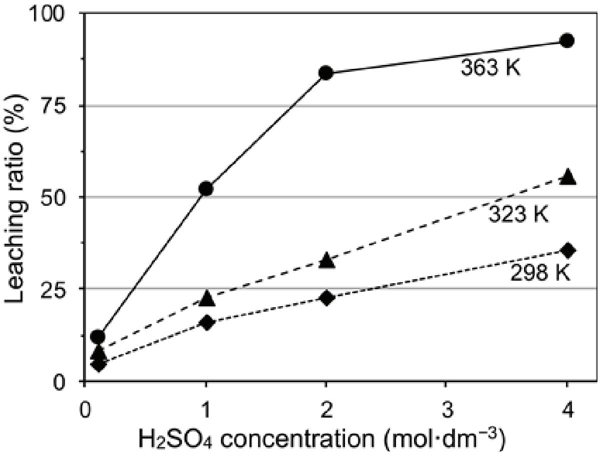

Figure 5. The effects of sulfuric acid concentration on the leaching of cesium.

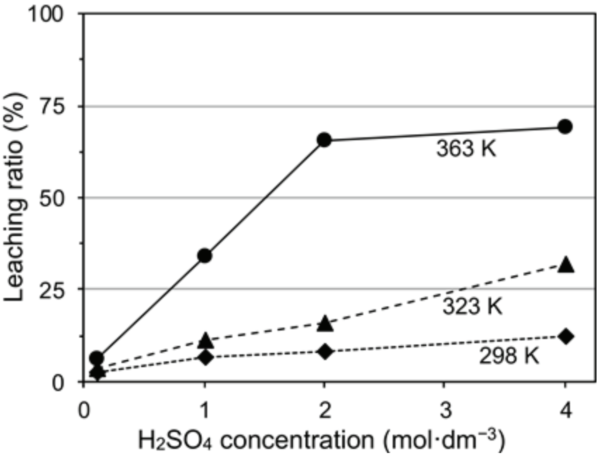

Figure 6. The effects of sulfuric acid concentration on the leaching of rubidium.

There are only a few literature studies on the acid leaching of Li from different clay samples of the Kırka borate deposit. In this respect, Mordoğan et al. [10] obtained a Li leaching ratio of 99% from a -500 μm Kırka ulexite zone clay sample containing approximately 0.56% Li_2O in ~1.63 mol·dm^{-3} H_2SO_4 solution within 2 hours at 353 K. Lee et al. [11] reported 89% dissolution of Li from a -74 μm clay sample of the Kırka deposit with approximately 0.39% Li_2O content after leaching in 0.25 mol·dm^{-3} HCl solution for 10 hours at solid/liquid ratio of 1 g/200 cm^3. In addition, Baydır and Erdoğan [12] observed that Rb could not be leached to the desirable extent in water or acid solutions (0.1 to 1 mol·dm^{-3} HCl and 0.1 to 1 mol·dm^{-3} HNO_3) from 'montmorillonite waste' sample of the Kırka deposit, which was identified to be potassium feldspar containing 1148-1690 μg/g Rb.

On the other hand, Mordoğan et al. [10] and Helvaci et al. [9] stated that most of Kırka smectites occur as hectorite. In the literature, sulfuric acid leaching of hectorite samples appears to have received limited interest. Komadel et al. [14] reported a 50% extraction of Li from a hectorite sample having approximately 1.09% Li_2O (solid/liquid ratio: 1 g/200 cm^3) in 1 mol·dm^{-3} H_2SO_4 at 293 K for 2.7 hours. However, they reported complete extraction of Li when the leaching time was extended to 8 hours under the same conditions. van Rompaey et al. [16] indicated the influence of leaching time on the dissolution of Li from a hectorite sample (0.94% Li_2O). These researchers noted that the leaching of Li increased from 25 to 70% with extending the leaching time from 2.25 to 6 hours under the conditions of 1 g/200 cm^3 solid/liquid ratio, 2 mol·dm^{-3} H_2SO_4 concentration and 293 K temperature.

The XRD pattern of the leaching residue obtained after leaching under optimum conditions (in 2 mol·dm^{-3} H_2SO_4 at 363 K) was given in Figure 7. The disappearance of basal smectite peak at 2θ value of ~6.03° (see Figure 2) and the newly formed hump-type peak centered between 2θ(°)=22-23 indicated near-total dissolution of the main smectite component of the sample leaving an amorphous silica phase in the residue. On the other hand, the XRD peaks belonging to feldspar in the sample were still present in the pattern of leaching residue, indicating its higher resistance to sulfuric acid leaching. The very small intensity peak observed in the XRD pattern of the leaching residue at a 2θ value of approximately 19.9° may be an indication of the presence of trace amounts of undissolved smectite phase. The results of XRD analyses and the extensive metal leaching ratios obtained in 2 mol·dm^{-3} H_2SO_4 at 363 K for Li (97.2%) and Cs (83.7%) may suggest that these two metals probably associated with the clay mineral(s) in the sample. On the other hand, a comparatively lower leaching ratio of Rb (65.2%) may suggest that Rb probably related to the feldspar phase in the sample [12, www.mindat.org]. Further detailed investigations are apparently needed to find out the exact source(s) of these metals in the studied clay sample.

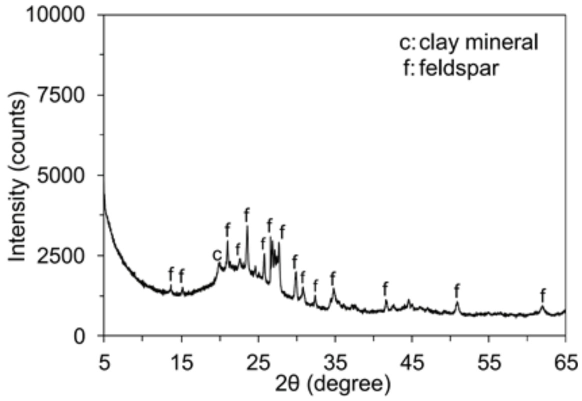

Figure 7. The XRD pattern of the leaching residue.

The formation of amorphous silica phase following acid leaching of smectites, especially hectorites, also appeared to be observed in other studies. Madejová et al. [17] reported a complete conversion of a hectorite sample to an amorphous silica phase after leaching for 1 h in a 0.5 mol·dm^{-3} HCl solution at 293 K. Steudel et al. [15] also obtained amorphous silica in the leaching residue formed after leaching of a clay sample containing 93.9% hectorite, 3.1% calcite, 2.1% analcime and 0.7% ankerite in 5 mol·dm^{-3} H_2SO_4 for 1.5 h at 353 K (solid/liquid ratio: 1 g/100 cm^3).

The leaching of the clay sample in 2 mol·dm^{-3} H_2SO_4 at 363 K for 1 h appeared to lead to a significant increase in the B.E.T. specific surface area of the sample from 59 to 406 m^2/g. This increase is probably due to the transformation of the main crystalline smectite component of the sample to an amorphous silica phase. Such an increase in the surface area of smectites following acid leaching was also observed by Steudel et al. [15]. They reported that the specific surface area of a hectorite sample increased from 48 to 280 m^2/g after leaching for 1.5 h in 5 mol·dm^{-3} H_2SO_4 at 353 K.

In addition to the findings in the XRD and B.E.T. analyses, the formation of a hydrous amorphous silica phase could also be substantiated using FTIR analyses. The FTIR spectrum (Figure 8a) of the residue obtained after leaching under the optimum conditions showed absorptions at 796 cm^{-1}, a shoulder between at 970-980 cm^{-1}, at 1086 cm^{-1}, a shoulder near 1200 cm^{-1}, at 1635 cm^{-1} and 3440 cm^{-1}, all belong to water and silicon-oxygen bonds in hydrous amorphous silica phases, as indicated in the literature [14,15,17].

The DTA curves of the sample and the residue (obtained under the leaching conditions of 2 mol·dm^{-3} H_2SO_4, 363 K and 1 h) were presented in Figure 8b. The DTA curve of the sample showed a large endothermic dehydration peak at 403 K with a shoulder at 467 K and small intensity high-temperature dehy-

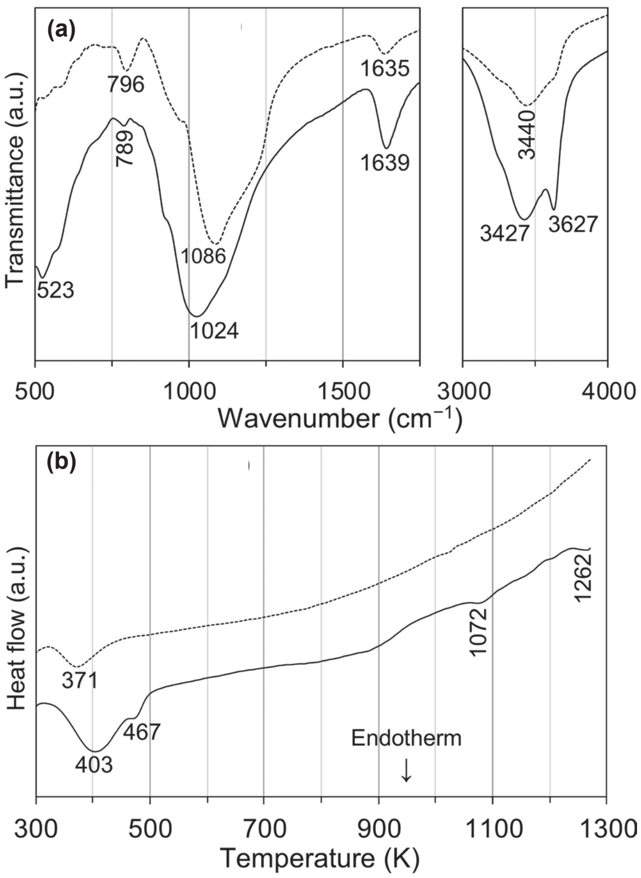

Figure 8. The FTIR spectra (a) and the DTA curves (b) of the sample (full lines) and the leaching residue (dotted lines).

droxylation (and probable recrystallization or new phase formation) peaks above 873 K, both are characteristic for smectites [18,19]. The destruction of the smectite phase in the sample and the formation of the hydrous amorphous phase in the leaching residue could be observed by the disappearance of dehydration and high-temperature peaks in the DTA curve of the leaching residue [20]. Futhermore, the appearance of a single endothermic dehydration peak with no visible distinct high-temperature peak(s) in the DTA curve is also an indication of the presence of a hydrous amorphous phase in the residue [21].

4. Conclusions

In this work, the leaching behaviours of Li, Cs and Rb from a clay sample taken from the Kırka borate deposit in sulfuric acid solutions were investigated. Various characterization methods were applied to the clay sample and the leaching residue. A similar trend for leaching of Li, Cs and Rb was observed at the highest leaching temperature of 363 K in response to the increase in sulfuric acid concentration. The lowest leaching ratios of these elements were found to occur in all acid concentrations tested at 298 K. Increasing the temperature from 298 K to 363 K had a profound effect on the leaching of Li, Cs and Rb. Under the optimum conditions (i.e. 2 mol·dm^{-3} H_2SO_4 and 363 K), the leaching ratio values obtained for Li, Cs and Rb were 97.2, 83.7 and 65.2%, respectively. The XRD, FTIR and DTA analyses indicated that in the acid leaching under optimum conditions, the crystalline smectite structure(s) in the clay sample was destructed and a hydrous amorphous silica phase was formed, with a concomitant increase in the specific surface area (from 59 to 406 m^2/g). The findings of this preliminary study may be exploited in the further hydrometallurgical processing of the vast amount of clay containing processing waste that has been generated and already accumulated over the years in the Kırka boron plant.

Acknowledgements

This study was supported by Boron Research Institute (BOREN, Project no: 2019-30-06-30-005).

References

[1] Vikström H., Davidsson S., Höök M., Lithium availability and future production outlooks, Appl. Energy, 110, 252-266, 2013.

[2] Meshram P., Pandey B. D., Mankhand T. R., Extraction of lithium from primary and secondary sources by pretreatment, leaching and separation: A comprehensive review, Hydrometallurgy, 150, 192-208, 2014.

[3] Choubey P. K., Kim M. S., Srivastava R. R., Lee J. C., Lee J. Y., Advance review on the exploitation of the prominent energy-storage element: Lithium. Part I: From mineral and brine resources, Miner. Eng., 89, 119-137, 2016.

[4] Swain B., Recovery and recycling of lithium: A review, Sep. Purif. Technol., 172, 388-403, 2017.

[5] Li H., Eksteen J., Kuang G., Recovery of lithium from mineral resources: State-of-the-art and perspectives-A review, Hydrometallurgy, 189, 105129, 2019.

[6] Tadesse B., Makuei F., Albijanic B., Dyer L., The beneficiation of lithium minerals from hard rock ores: A review, Miner. Eng., 131, 170-184, 2019.

[7] Gu H., Guo T., Wen H., Luo C., Cui Y., Du S., Wang N., Leaching efficiency of sulfuric acid on selective lithium leachability from bauxitic claystone, Miner. Eng., 145, 106076, 2020.

[8] Karrech A., Azadi M. R., Elchalakani M., Shahin M. A., Seibi A. C., A review on methods for liberating lithium from pegmatites, Miner. Eng., 145, 106085, 2020.

[9] Helvaci C., Mordogan H., Çolak M., Gündogan I., Presence and distribution of lithium in borate deposits and some recent lake waters of west-central Turkey, Int. Geol. Rev., 46, 177-190, 2004 (in Turkish).

[10] Mordoğan H., Akdağ M., Helvacı C., Lithium recover from low-grade lithium-bearing clays by H_2SO_4 and roast-water leach processes, Geosound, 24, 141-150, 1994 (in Turkish).

[11] Lee W. J., Yoon S. J., Chon C. M., Heo C. H., Lee G. J., Lee B. H, Cicek M., Lithium extraction from smectitic clay occurring in lithium-bearing boron deposits in Turkey, J. Miner. Soc. Korea, 29, 167-177, 2016 (in Korean).

[12] Baydır A. T., Erdoğan Y., Dissolution of the rubidium from Eti Mine Kırka Boron Management waste, AKU-J. Sci. Eng., 13, 025702, 2013 (in Turkish).

[13] Gündoğdu M. N., Yılmaz O., Methods of clay mineralogy, Proc. 1st Nat. Clay Symp., Adana-Turkey, 319-330, 1984 (in Turkish).

[14] Komadel P., Madejová J., Janek M., Gates W. P., Kirkpatrick R. J., Stucki J. W., Dissolution of hectorite in inorganic acids, Clays Clay Miner., 44, 228-236, 1996.

[15] Steudel A., Batenburg L. F., Fischer H. R., Weidler P. G., Emmerich K., Alteration of swelling clay minerals by acid activation, Appl. Clay Sci., 44, 105-115, 2009.

[16] Van Rompaey K., Van Ranst E., De Coninck F., Vindevogel N., Dissolution characteristics of hectorite in inorganic acids, Appl. Clay Sci., 21, 241-256, 2002.

[17] Madejová J., Bujdák J., Janek M., Komadel P., Comparative FT-IR study of structural modifications during acid treatment of dioctahedral smectites and hectorite, Spectrochim. Acta, Part A, 54, 1397-1406, 1998.

[18] Grim, R. E., Clay Mineralogy, 2nd Edition, McGraw-Hill, New York, A.B.D., 1968.

[19] Guggenheim S., Van Groos A. F. K., Baseline studies of the clay minerals society source clays: Thermal analysis, Clays Clay Miner., 49, 433-443, 2001.

[20] Yalçın S., Özbelge Ö., Acid activation of bentonite, Proc. 2nd Nat. Clay Symp., Ankara-Turkey, 229-250, 1985 (in Turkish).

[21] Ehsani İ., Turianicová E., Baláž M., Obut A., Effects of sulphuric acid dissolution on the physical and chemical properties of a natural and a heated vermiculite, Acta Montan. Slovaca, 20, 110-115, 2015.

BORON 5(4), 176 - 182, 2020

BOR DERGİSİ
JOURNAL OF BORON
https://dergipark.org.tr/boron

Kolemanit, tinkal, üleksit ve bor atığında atomik absorpsiyon spektroskopi yöntemi ile Fe, Ni, Co ve Zn eser elementlerinin tayini

Argun Türker[1*], **Orhan Acar**[2]

[1]**Gazi Üniversitesi, Fen Fakültesi, Kimya Bölümü, 06500 Ankara, Türkiye, ORCID ID orcid.org/0000-0002-5876-9512**
[2]**Gazi Üniversitesi, Fen Fakültesi, Kimya Bölümü, 06500 Ankara, Türkiye, ORCID ID orcid.org/0000-0002-0969-2627**

MAKALE BİLGİSİ

Makale Geçmişi:
İlk gönderi 22 Mayıs 2020
Kabul 11 Kasım 2020
Online 29 Aralık 2020

Araştırma Makalesi

DOI: 10.30728/boron.756254

Anahtar kelimeler:
Atomik absorpsiyon spektroskopisi,
Bor atığı,
Kolemanit,
Tinkal,
Üleksit.

ÖZET

Bu çalışmada, Türkiye’de en bol bulunan bazı bor minerallerinde (kolemanit, tinkal ve üleksit) ve bor atığında Cu, Fe, Ni, Co ve Zn eser elementleri alevli atomik absorpsiyon spektrometresi kullanılarak tayin edilmiştir. Bor minerallerinin çözülmesi için uygun çözücü belirlendikten sonra numuneler çözülmüş ve numune çözeltilerinde elementler tayin edilmiştir. Yöntemin geçerli kılınması amacıyla yöntemin doğruluğu ve kesinliği standart referans maddeler (NIST Montana soil 2711 ve NIST Estuarine sediment 1646a) analiz edilerek kontrol edilmiştir. Ayrıca yöntem için çalışılan her elemente ait doğrusal çalışma aralığı, gözlenebilme sınırı (LOD) ve tayin sınırı (LOQ) değerleri de belirlenmiştir. Tayin edilen elementlerin bor mineralleri ve bor atığındaki derişim aralıkları Cu, Fe, Ni, Co ve Zn için sırasıyla <LOD - 5,4 µg/g, 7,6 - 458 µg/g, 2,3 - 8,2 µg/g, 1,6 - 111 µg/g ve <LOD - 5,02 µg/g olarak bulunmuştur.

Determination of Fe, Ni, Co and Zn trace elements in colemanite, tinkal, ulexite and boron waste by atomic absorption spectroscopy method

ARTICLE INFO

Article history:
Received May 22, 2020
Accepted November 11, 2020
Available online December 29, 2020

Research Article

DOI: 10.30728/boron.756254

Keywords:
Atomic absorption spectroscopy,
Boron waste,
Colemanite,
Tinkal,
Ulexite.

ABSTRACT

In this study, Cu, Fe, Ni, Co and flame Zn trace elements were determined in boron minerals most abundant in Turkey (colemanite, tinkal and ulexite) and boron waste using atomic absorption spectrometry. After determining the suitable solvent for the dissolution of boron minerals, the samples were dissolved and the elements were determined in the sample solutions. In order to validate the method, the accuracy and precision of the method was checked by analyzing standard reference materials (NIST Montana soil 2711 and NIST Estuarine sediment 1646a). In addition, linear working range, limit of detection (LOD) and limit of quantification (LOQ) values for each element studied were determined for the method. The concentration ranges of the elements determined in boron minerals and boron waste are <LOD - 5.4 µg/g, 7.6-458 µg/g, 2.3-8.2 µg/g, 1.6-111 µg/g and <LOD - 5.02 µg/g for Cu, Fe, Ni, Co and Zn, respectively.

1. Giriş (Introduction)

Süper iletken gibi ileri teknoloji sanayi ürünleri, ilaç sanayi ürünleri, gübreler, gıdalar nükleer santrallarda kullanılan malzemeler ve diğer birçok ürün içerdikleri eser elementlerden az veya çok miktarda, olumlu veya olumsuz olarak etkilenirler. İster numunenin yapısından kaynaklansın isterse safsızlık olarak gelsin derişimi %0,01’den küçük olan bileşenlere eser bileşen adı verilmektedir. Eser elementlerin son ürünlerdeki ve canlı organizmalardaki miktarları çevre koşullarına ve bu malzemelerin üretiminde kullanılan ham maddenin saflığına göre değişmektedir. Her malzemenin kullanıldığı alana bağlı olarak kabul edilebilecek bir eser element derişimi vardır. Örneğin bir gübrede eser elementlerin daha yüksek derişimlerine izin verilebilirken, bir ilaç veya gıda alanında bu değerler çok daha düşüktür. Bazı durumlarda bir malzemenin veya canlı organizmanın işlevini yerine getirilebilmesi için bünyesinde eser elementlerin belirli miktarlarda olması da gerekir. Bu nedenle, son ürünün elde edildiği ham maddeler, ürünlerin doğrudan veya dolaylı olarak temas halinde bulunduğu ortamlardaki eser elementler sürekli tayin edilmeli ve kontrol altında tutulmalıdır [1-4]. Eser elementin malzemede bulunması bazı durumlarda malzemeye istenen bir özellik katarken bazı du-

---

*Sorumlu yazar: argunturker@gazi.edu.tr

rumlarda zararlı etki gösterir. Bu etkiler eser elementin malzemedeki derişimine göre de değişebilir. Örneğin düşük oranlarda yararlı etki gösteren bir element belirli derişimin üzerinde olumsuz etki yapabilir. Bu nedenle eser elementler sağlık için genel olarak günümüzde birinci derecede kirleticiler arasında sınıflandırılırlar. Ancak, tüm eser elementleri zararlı olarak sınıflandırmak da doğru değildir. Bazı eser elementler insan, hayvan ve bitki yaşamında önemli görevleri de yerine getirmektedir. WHO eser elementleri 3 sınıfta toplamıştır [5]. Bunlar (1) gerekli elementler (Cu, Zn, Se, Co, I, Mn, Mo gibi) (2) olası gerekli elementler ve (3) potansiyel olarak toksik elementler. Birinci gruptaki elementler az alındığında işlevlerini yerine getirememekte, fazla alındıklarında ise zehirlenmeler olmaktadır [5]. Sağlık için tamamen zararlı kabul edilen elementler Al, As, Ba, Cd, Hg, Pb, Sb, Sr, Th, Tl, Hg ve Cr(VI) gibi elementlerdir [6]. Bu elementler farlı yollarla çevreye yayılarak canlılar üzerinde olumsuz etki gösterebilmektedirler [6,7]. Bu elementlerin çevredeki, gıdalardaki ve minerallerdeki derişim değerlerinin bilinmesi ve sürekli kontrol edilmeleri önemlidir.

Eser elementlerin tayininde günümüzde genellikle spektroskopik (atomik absorpsiyon spektrometresi, atomik emisyon spektrometresi, nötron aktivasyon analizi, X ışınları floresans spektrometresi, atomik floresans spektrometresi ve kütle spektrometresi vb.) ve elektroanalitik yöntemler (diferansiyel puls polarografisi, anodik veya katodik sıyırma voltametrisi vb.) gibi yöntemler kullanılmaktadır [8-10].

Ülkemizde bol miktarda bulunması ve stratejik bir mineral olması nedeniyle bor minerallerin minerolojik yapıları çok fazla çalışılmış ve ana bileşenlerin oranları belirlenmiştir [11-16]. Buna karşın bu minerallerdeki eser elementlerle ilgili yeteri kadar çalışma yapılmamıştır. Çeşitli numunelerdeki bor tayini de birçok makalede yer almıştır [17-22]. Bor minerallerinde bulunan eser düzeydeki elementlerin tayini için hem Türkiye'de hem de dünyada sınırlı sayıda çalışma vardır. Erdoğan vd. indüktif olarak eşleşmiş plazma optik emisyon spektroskopisi (ICP-OES) ile üleksit, tinkal ve kolemanitte bazı ana ve eser elementlerin tayinini gerçekleştirmişlerdir [23]. Üç mineralde Dy, Ti, Bi, C, B, Ba, Co, Cs, U, Nb, Ru, Th, W, Be, P, Pt, Au, V, Yb, Er, Zr, Tl, Pb, Li, K, Ca, Sr, Sc, S, Ni ve Cu tayin edilmiş ve sonuçlar ppm cinsinden verilmiştir. Bazı elementler için herhangi bir değer verilmemiş, sonuçların doğruluğu ve kesinliği ile ilgili veri verilmemiş ve yorum yapılmamıştır. Yine Erdoğan ve arkadaşları ICP-OES ile tinkal ve kolemanit atıklarında element tayini yapmışlardır. Bu çalışmada da yukarıda sözü edilen elementler tayin edilmiştir [24]. Tinkal atığında bulunan değerler ppm cinsinden şu şekilde verilmiştir: B: 71270; Ti: 638,4; Cs:19900; Th: 690,8; Al: 70190; Er: 26,36; Zr: 676,4; Li: 172,9; Ca: 112200; Ni: 69,70 ve Na: 312500 ppm. Kolemanit atığında da B: 44930; Ti: 98,06; Cs: 19810; Ru: 51,67; Al: 36470; Yb: 1,737; U: 76,49 ve Ca: 323500 ppm olarak verilmiştir. Her iki çalışma da II. Uluslararası Bor Sempozyumunda sunulmuş, ancak herhangi dergide yayımlanmamıştır.

Bir başka çalışmada, Ertan ve Erdoğan, Emet-Espey bölgesinde Eti Maden işletmesi tarafından farklı bölgelerden alınan bor atığı numunelerinde eser element tayini yapmışlardır [12]. Özellikle bor içeren kil numunelerinde, önemli miktarlarda değerli eser elementlerin olduğu gözlenmiştir. Li, Rb, Cs, Ti, Mn, As ve Na derişimleri dikkat çekici olarak bulunmuştur. Espey bölgesindeki tüm atıklarda Mn, As ve Na derişimleri yakın sonuçlar gösterirken; Li, Rb, Cs gibi eser elementlerin derişimleri killi atıklarda bağıl olarak daha fazla bulunmuştur. Bu sonuca göre özellikle kil içerikli bor atıklarından Li, Rb, Cs elementlerin kazanılabileceği yorumu yapılmıştır. F. Özmal doktora tezinde Hisarcık-Espey bölgesinde bor atıklarında eser elementlerin tayinini yapmış ve atıklardaki lityumun değerlendirilmesi konusunu irdelemiştir [13]. Kılıç, Yüksek Lisans tezinde, Eti Maden Kırka Bor İşletmesindeki, konsantratör tesisi ve açık ocak işletmesinde oluşan atıklardan alınan numunelerin analizi ve sınıflandırılmasını çalışmıştır [25]. Koçak ve Koç, Dünyanın en büyük kolemanit ve üleksit yatağı olan Bigadiç borat yataklarında ana ve eser element jeokimyasını çalışmışlardır [11]. Çalışmada ayrıca bor minerallerinin jeolojisi incelenmiş ve bu minerallerin volkanik yapıda olduğu belirlenmiştir. Karabulut ve Budak, kolemanit mineralinde radioizotop X-ışını floresans analizi ile bazı elementlerin tayinini gerçekleştirmişlerdir [26]. Bu çalışmada Balıkesir ili Bigadiç yöresi kolemanit cevherindeki As, Sr, In, Sn, Sb, I, Cs ve Ba elementleri enerji dağılımlı X-ışını Floresans (EDXRF) sistemi kullanılarak tayin edilmiştir. Bir başka çalışmada, Kalfa ve arkadaşları Kırka-Eskişehir'deki Etibank Boraks Fabrikasından çıkan boraks atığında, enerji dağılımlı X-ışını floresans (EDXRF) tekniği ile Al, Fe, Zn, Sn ve Ba tayin etmişlerdir [27].

Bu çalışmada, Türkiye'de bol bulunan ve ham madde olarak çok kullanılan kolemanit, tinkal ve üleksit minerallerinde ve ayrıca bor atığında Cu, Fe, Ni, Co, Zn, elementlerin atomik absorpsiyon spektroskopisi ile tayinlerinin yapılması ve minerallerin sonraki aşamada kullanılmasında bu elementlerin etkilerinin neler olabileceğinin ortaya konulması amaçlanmıştır. Literatür taramasından da görüleceği üzere bor minarallerindeki eser elementlerin tayinleri ağırlıklı olarak X ışını floresans spektrometresi veya indüktif olarak eşleşmiş optik emisyon spektrometresi gibi daha pahalı ve her laboratuvarda bulunmayan cihazlarla yapılmıştır. Bu çalışmada ise hemen hemen her kimya laboratuvarında bulunan, kullanımı kolay ve ucuz olan alevli atomik absorpsiyon spektrometresi kullanılmıştır. Deneysel değişkenlerin en uygun değerleri belirlendikten sonra bu koşullarda tayinler gerçekleştirilmiştir. Tayinlerin doğruluğu ve kesinliği de standart referans maddeler (SRM: NIST Montana soil 2711 ve NIST Estuarine sediment 1646a) ve bilinen analitik teknikler uygulanarak araştırılmıştır. Bu çalışmada, kesinlik, doğruluk, doğrusal çalışma aralığı, gözlenebilme sınırı ve tayin sınırı gibi geçerli kılma değişkenleri belirlenerek diğer çalışmalarda olmayan geçerli kılma çalışması yapılmış ve böylece sonuçların güvenilirliği analitik açıdan gösterilmiştir.

2. Malzemeler ve yöntemler (Materials and methods)

2.1. Cihazlar (Apparatus)

Bu çalışmada Varian (Mulgrave Virginia, Avusturalya) Spectra AA240FS döteryum zemin düzeltmeli alevli atomik absorpsiyon spektrometresi (FAAS) kullanılmıştır. Işın kaynağı olarak Varian marka oyuk katot lambaları kullanılmıştır. Alevli AAS yöntemiyle Fe, Zn, Cu, Ni ve Co tayini için aletsel değişkenler Tablo 1'de verilmiştir.

2.2. Reaktifler (Reagents)

Aksi belirtilmedikçe bu çalışmada analitik saflıkta reaktifler ve iyonları giderilmiş saf su (deiyonize su, öz direnci 18 MΩ.m) kullanılmıştır. Standart çalışma çözeltileri (Co, Cu, Fe, Ni ve Zn) ticari olarak atomik absorpsiyon cihazı için satın alınan stok metal çözeltilerinden (1000 mg/L, Merck) hazırlanmıştır. Numunelerin çözülmesinde derişik hidroklorik asit (HCl, d=1,19 g/mL, Merck) ve derişik nitrik asit (HNO_3, d=1,42 g/mL, Merck) kullanılmıştır.

Uygulanan yöntemin doğruluğunu ve kesinliğini kontrol etmek amacıyla Montana Soil 2711 ve Estuarine sediment 1646a standart referans maddeleri kullanılmış ve bulunan sonuçlar değerlendirilmiştir.

2.3. Numunelerin ve standart referans maddelerin analize hazırlanması (Preparation of samples and standard reference materials for analysis)

Bu çalışmada, bor atığı, kolemanit [$Ca_2B_6O_{11}.5H_2O$], tinkal [$Na_2B_4O_7.10H_2O$] ve üleksit [$NaCaB_5O_9.8H_2O$] mineralleri kullanılmıştır. Kolemanit, tinkal ve bor atığı Kırka'dan, üleksit de Bigadiç'ten tane iriliği 75 μm'ye öğütülmüş olarak temin edilmiştir. Kullanılan bor atığının (Kırka İşletmeleri 5. göl atığı) ve bor minerallerinden kolemanit, tinkalin kimyasal analizleri önceki çalışmada [28] belirlenmiş ve Tablo 2'de verilmiştir.

Yaklaşık 10 g kolemanit ve 5 g üleksit 0,001 g yaklaşımla tartılarak ayrı ayrı iki cam behere konulmuştur. Her bir behere 100 mL saf su, 30 mL derişik HCl ve 10 mL derişik HNO_3 ile hazırlanmış olan asit karışımı ilave edilmiştir. Karışım 120 dakika boyunca ısıtıcıda 100ºC'de karıştırılarak ısıtılmıştır. Sürenin sonunda soğutulan çözeltiler, ayrı 250 mL'lik ölçülü balonlara sık gözenekli süzgeç kâğıdı ile süzülmüş ve çözeltilerin hacmi saf su ile 250 mL'ye tamamlanmıştır.

Yaklaşık 15 g tinkal (boraks) 0,001 g yaklaşımla tartılarak bir behere konulmuştur. Üzerine 100 mL saf su ve 5 mL derişik HNO_3 eklenmiştir. 15 dakika ısıtıcıda 100ºC'de karıştırılarak ısıtılmıştır. Soğutulan çözelti 250 mL'lik bir ölçülü balona aktarılmış ve hacim saf su ile 250 mL'ye tamamlanmıştır. Tinkal tamamen çözündüğü için herhangi bir süzme işlemi yapılmamıştır.

Yaklaşık 10 g bor atığı 0,001 g yaklaşımla tartılarak bir behere alınmıştır. Üzerine 100 mL saf su ve 10 mL derişik HNO_3 eklenmiş ve 60 dakika boyunca ısıtıcıda 100ºC'de karıştırılarak ısıtılmıştır. Çözelti soğutulduktan sonra 250 mL'lik bir ölçülü balona kaba süzgeç kâğıdı ile süzülmüş ve hacmi deiyonize su ile 250 mL'ye tamamlanmıştır.

Standart referans maddeler literatürde yer alan yönteme göre çözülmüştür [29]. Standart referans maddelerin çözülmesi için yaklaşık 0,5 g Montana 2711 ve yaklaşık 0,8 g Estuarine sediment 1646a standart referans maddeleri 0,001 g yaklaşımla tartılarak ayrı ayrı beherlere alınmıştır. Öncelikle çözme için her iki standart referans madde içeren beherlere 5 mL derişik HCl ve 5 mL derişik HNO_3 eklenmiş ve 2 saat bekletilmiştir. Ardından çözeltiler ısıtıcı tablada beher içerisinde 2-3 mL çözelti kalıncaya kadar buharlaştırma yapılmıştır. Çözünmeden kalan maddeler için ise beherlere 2 mL derişik HNO_3 ve 2 mL kütlece %60'lık $HClO_4$ eklenmiştir. Çözeltiler tekrar 2-3 mL kalacak şekilde ısıtıcı tablada buharlaştırılmıştır. Bu işlemlerden sonra çözünmeden kalan kısım sık gözenekli süzgeç kâğıdı ile süzülmüştür. Süzme işleminden sonra Montana 2711 standart referans maddesi 50 mL'lik bir ölçülü balona, Estuarine sediment 1646a standart referans maddesi ise 25 mL'lik bir ölçülü balona alınarak damıtık ve iyonları giderilmiş su ile işaret çizgisine kadar tamamlanmıştır.

Tablo 1. FAAS yöntemiyle Fe, Zn, Cu, Ni ve Co tayininde aletsel değişkenler (Instrumental variables in the determination of Fe, Zn, Cu, Ni and Co by FAAS method).

Element	Çalışılan Dalga Boyu, nm	Yarık Genişliği, nm	Lamba Akımı, mA	Asetilen Akış Hızı, L/min	Hava Akış Hızı, L/min	Zemin Düzeltmesi
Co	240,7	0,2	7	2	13,5	Var
Cu	324,8	0,5	4	2	13,5	Var
Fe	248,3	0,2	5	2	13,5	Var
Ni	232,0	0,2	4	2	13,5	Var
Zn	213,9	1,0	5	2	13,5	Var

Tablo 2. Kolemanit, tinkal ve bor atığının kimyasal analizi (Chemical analysis of colemanite, tincal and boron waste) [26].

Bileşen	Kolemanit (% m/m)	Bor Atığı (% m/m)	Tinkal (% m/m)
B_2O_3	40,00 ± 0,05	22,9	En az 36,47
CaO	27,00 ± 1	11,8	-
SiO_2	4,00 – 6,50	9,06	-
SO_4	0,60 en çok	0,11	135 ppm
As	35 ppm en çok	-	-
Fe_2O_3	0,08 en çok	0,10	15 ppm (Fe olarak)
Al_2O_3	0,40 en çok	0,47	-
MgO	3,00 en çok	12,63	-
SrO	1,50 en çok	0,59	-
Na_2O	0,35	4,48	En az 16,24
K.K[a)]	22,13	40,59	46,77

[a)] KK: Kızdırma kaybı.

Standart referans maddeler literatürde yer alan yönteme göre çözülmüştür [29]. Standart referans maddelerin çözülmesi için yaklaşık 0,5 g Montana 2711 ve yaklaşık 0,8 g Estuarine sediment 1646a standart referans maddeleri 0,001 g yaklaşımla tartılarak ayrı ayrı beherlere alınmıştır. Öncelikle çözme için her iki standart referans madde içeren beherlere 5 mL derişik HCl ve 5 mL derişik HNO_3 eklenmiş ve 2 saat bekletilmiştir. Ardından çözeltiler ısıtıcı tablada beher içerisinde 2-3 mL çözelti kalıncaya kadar buharlaştırma yapılmıştır. Çözünmeden kalan maddeler için ise beherlere 2 mL derişik HNO_3 ve 2 mL kütlece %60'lık perklorik asit ($HClO_4$) eklenmiştir. Çözeltiler tekrar 2-3 mL kalacak şekilde ısıtıcı tablada buharlaştırılmıştır. Bu işlemlerden sonra çözünmeden kalan kısım sık gözenekli süzgeç kâğıdı ile süzülmüştür. Süzme işleminden sonra Montana 2711 standart referans maddesi 50 mL'lik bir ölçülü balona, Estuarine sediment 1646a standart referans maddesi ise 25 mL'lik bir ölçülü balona alınarak damıtık ve iyonları giderilmiş su ile işaret çizgisine kadar tamamlanmıştır.

3. Sonuçlar ve tartışma (Results and discussion)

3.1 Yöntemin geçerli kılınması (Validation of the method)

Gerçek numune analizine geçmeden önce uygulanacak analiz yönteminin geçerli kılınması için geçerli kılma değişkenlerinin (doğruluk, kesinlik, doğrusal çalışma aralığı, gözlenebilme sınırı ve tayin sınırı) belirlenmesi için çalışmalar yapılmıştır.

3.1.1 Kalibrasyon grafikleri ve doğrusal çalışma aralığı (Calibration graphs and linear working range)

Çözeltileri hazırlanan numunelerde; Fe, Cu, Co, Ni ve Zn elementleri normal kalibrasyon grafiği yöntemi uygulanarak alevli AAS ile tayin edilmiştir. Kalibrasyon yöntemi uygulanırken tayin edilecek elementlerin uygun derişim aralığında standart çözeltileri hazırlanmıştır. Buna göre Fe için 10 mg/L'lik standart çözeltisi seyreltilerek 0,5; 1,0; 1,5 ve 2,0 mg/L'lik çözeltiler hazırlanmıştır. Cu, Co, Ni ve Zn için yine 10 mg/L'lik standart çözeltileri seyreltilerek 0,1; 0,2; 0,3 ve 0,4 mg/L'lik çözeltiler hazırlanmıştır. Tayin elementleri için elde edilen kalibrasyon eşitlikleri, bu eşitliklerin korelasyon katsayıları ve doğrusal çalışma aralığı Tablo 3'te verilmiştir. Doğrusal çalışma aralığının alt sınırı olarak tayin sınırı (Tablo 5'te bir element için belirlenen en yüksek LOQ) değerleri alınmıştır. Tayin sınırından daha küçük derişimlerin analitik açıdan yeterli doğruluk ve kesinlikle tayin edilemediği kabul edilir. Doğrusal çalışma aralığının üst sınırı Fe için 5 mg/L, diğer elementler için 2 mg/L olarak belirlenmiştir.

3.1.2 Yöntemin doğruluğu ve kesinliği (Accuracy and precision of the method)

Yöntemin doğruluğu ve kesinliğini belirlemek için, mineral yapısına benzeyen toprak belgeli standart referans maddeler (SRM) (NIST Montana soil 2711 and NIST Estuarine 1614a) analiz edilmiştir. SRM'ler dörder kez analiz edilerek tayin elementlerinin ortalama derişimleri belirlenmiş ve sonuçlar Tablo 4'te verilmiştir. Tablo 4'te görüldüğü gibi, elementler için bulunan derişimler, tayin elementleri için SRM'lerde verilen belgelenmiş değerleri ile uyumludur. Sonuçların yüzde bağıl hatası, tüm elementler için %5'ten düşük bulunmuştur. Bu düzeydeki bir bağıl hata, söz konusu derişimler için analitik açıdan kabul edilebilir düzeydedir. Yöntemin doğruluğu belirlendikten sonra bor minerallerinde element tayinleri yapılmıştır.

Kesinlik, aynı koşullar altında tekrarlanan deney sonuçlarının birbirine yakınlığının, yani sonuçların tek-

Tablo 3. Kalibrasyon eşitlikleri, korelasyon katsayıları ve doğrusal çalışma aralığı (Calibration equations, correlation coefficients and linear working range).

Element	Kalibrasyon Eşitliği [a)]	Korelasyon Katsayısı R^2	Doğrusal Çalışma Aralığı, µg/L
Zn	A = 0,3448 x C + 0,0007	0,9796	0,009 - 2000
Cu	A = 0,073 x C - 0,0032	0,9994	0,57 - 2000
Ni	A = 0,0489 x C - 0,0008	0,9976	0,71 - 2000
Co	A = 0,0498 x C + 0,0028	0,9996	0,73 - 2000
Fe	A = 0,0489 x C - 0,0023	0,9999	3,68 - 5000

[a)] Burada, A, absorbans, C element derişimi (mg/L)'dir.

rarlanabilirliğinin bir ölçüsüdür. Kesinlik, yüzde bağıl standart sapma (%BSS) ile matematiksel olarak belirlenebilir [30]. BSS, tekrarlanan deneylerden elde edilen sonuçların standart sapmasının sonuçların ortalamasına bölünmesiyle hesaplanır. SRM numunelerindeki elementlerin derişimleri dört tekrarlı ölçümden elde edilmiştir. Dört ölçüm sonucunun ortalama değerleri ve %95 güven seviyesinde güven aralıkları ve %BSS değerleri Tablo 4'te verilmiştir. Tablo 4'ten görüldüğü gibi, SRM'lerde tayinleri yapılan elementlerin %BSS'ları %3'ten düşük bulunmuştur. Bu kesinlik değeri, bor numune çözeltilerinde elementlerin çalışılan derişimleri için yeterli bir kesinlik olarak düşünülebilir.

3.1.3 Gözlenebilme sınırı ve tayin sınırı tayini ***(Limit of detection and limit of quantification)***

Yöntem için gözlenebilme sınırı (LOD) ve tayin sınırı (LOQ) tayini için numuneleri çözmek için kullanılan asit karışımları kullanılarak tanık çözeltiler hazırlanmıştır. Hazırlanan tanık çözeltilerin absorbansları elementlerin absorpsiyon yaptığı dalga boylarında 10 kez ölçülerek ortalama absorbans değeri ve bu değerlerin standart sapması (sb) hesaplanmıştır. Tanık çözelti için hesaplanan standart sapma ve elementler için çizilen kalibrasyon grafiği doğrularının eğiminden (m) yararlanılarak aşağıdaki bağıntılar yardımıyla gözlenebilme sınırı (LOD) ve tayin sınırı (LOQ) derişimleri hesaplanmıştır.

$$C_{LOD} = \frac{3s_b}{m} \tag{1}$$

$$C_{LOQ} = \frac{10s_b}{m} \tag{2}$$

Tayin edilen elementler için LOD ve LOQ değerleri Tablo 5'te verilmiştir.

3.2 Bor mineralleri ve bor atığı analizi ***(Analysis of boron minerals and boron waste)***

Yöntemin geçerli kılma değişkenleri belirlenip yöntem geçerli kılındıktan sonra bor mineralleri ve bor atığı çözeltilerinde Fe, Cu, Co, Ni ve Zn elementler tayin edilmiştir. Belirlenen deneysel koşullarda ve kalibrasyon grafiği yöntemi ile numune çözeltilerinde bulunan Fe, Cu, Co, Ni ve Zn derişimleri uygun seyreltme faktörleri ve numune miktarı dikkate alınarak mineraldeki derişimlere dönüştürülmüştür. Her analiz 4 kez tekrarlanmış ve ortalama değerler %95 güven seviyesinde güven aralığı ile birlikte verilmiştir. Bor minerallerinde ve atığında bulunan element derişimleri Tablo 6'da verilmiştir.

Tablo 4. Standart referans maddelerde element tayinleri (Determination of elements in standard reference materials).

Standart Referans Madde (SRM)	Element	Belgeli Değer (µg/g)	Bulunan Değer[a)] (µg/g)	Bağıl Hata (%)	% BSS
Montana soil 2711	Cu	114 ± 2	110 ± 4	-3,5	2,3
	Fe (%)	2,89 ± 0,06	2,86 ± 0,07	-1,0	1,5
	Co	10	10,5 ± 0,4	5,0	2,4
	Ni	20,6 ± 1,1	21,5 ± 0,7	4,4	2,0
	Zn	350,4 ± 4,8	341 ± 15	-2,7	2,8
Estuarine sediment 1646a	Cu	10,01 ± 0,34	9,9 ± 0,4	-1,1	2,5
	Fe (%)	2,89 ± 0,039	2,96 ± 0,04	2,4	1,3
	Co	5	4,9 ± 0,2	-2,2	2,6
	Ni	23	24 ± 1	4,3	2,6
	Zn	48,9 ± 1,6	47,2 ± 1,5	-3,5	2,0

[a)] Sonuçlar, % 95 güven seviyesinde 4 ölçümün ortalamasıdır, $\bar{x} \pm \frac{3{,}18 \times s}{\sqrt{N}}$ (burada s standart sapma; N ölçüm sayısı; 3,18 güven seviyesi ve serbestlik derecesine bağlı Student t değeridir)

Tablo 5. Bor minerallerinde ve atığında alevli AAS’de tayin edilen elementler için LOD ve LOQ değerleri (N=10) (LOD and LOQ values for the elements determined in flame AAS in boron minerals and waste (N=10)).

Element	Tinkal a)		Kolemanit a)		Üleksit a)		Bor atığı a)	
	LOD	LOQ	LOD	LOQ	LOD	LOQ	LOD	LOQ
Co	0,22	0,73	0,16	0,53	0,16	0,53	0,18	0,60
Cu	0,17	0,57	0,09	0,31	0,09	0,31	0,05	0,17
Ni	0,11	0,37	0,21	0,70	0,21	0,70	0,16	0,53
Fe	1,10	3,67	0,95	3,17	0,95	3,17	0,82	2,73
Zn	0,002	0,007	0,002	0,007	0,002	0,007	0,003	0,01

a) Sonuçlar µg/L olarak verilmiştir.

Tablo 6. Bor minerallerinde ve atığında Fe, Cu, Co, Ni, Zn, Cd ve Pb derişimleri (Fe, Cu, Co, Ni, Zn, Cd and Pb concentrations in boron minerals and waste).

Element	Derişim a), µg/g			
	Tinkal	Üleksit	Kolemanit	Bor atığı
Co	1,6 ± 0,1	111 ± 1	8,8 ± 0,1	3,0 ± 0,9
Cu	< LOD	3,3 ± 0,6	5,4 ± 0,1	2,71 ± 0,05
Ni	2,3 ± 0,1	6,2 ± 0,2	8,2 ± 0,2	5,3 ± 0,3
Fe	7,6 ± 0,1	8,4 ± 0,2	458 ± 4	77,7 ± 0,4
Zn	< LOD	5,02 ± 0,08	4,85 ± 0,06	2,9 ± 0,6

a) Sonuçlar, %95 güven seviyesinde 4 ölçümün ortalamasıdır, $\bar{x} \pm \frac{ts}{\sqrt{N}}$ (burada s standart sapma; N ölçüm sayısı; t güven seviyesi ve serbestlik derecesine bağlı Student t değeridir)

4. Sonuçlar (Conclusions)

Eser elementlerin bor mineralleri ve atıklarındaki derişimleri bu minerallerin son kullanım alanı açısından önemlidir. Bu nedenle bu çalışmada bu tür eser elementlerin derişimlerinin ölçülmesi amaçlanmıştır. Literatürde yer alan çalışmaların çoğunda söz konusu minerallerin kristal yapısı aydınlatılmaya çalışılmış, başlıca ana bileşenlerin derişimleri belirlenmiştir. Bor minerallerindeki eser elementlerin tayinleri ile ilgili sınırlı sayıda çalışma söz konusudur. Bu çalışmada analitik değerlendirme ölçütlerinden olan tayinin doğruluğu, kesinliği, çalışma aralığı, gözlenebilme ve tayin sınırları verilmiştir. Yöntemin doğruluğunu belirlemek için toprak standart referans maddeleri (Montana soil 2711 ve Estuarine sediment 1646a) analiz edilmiştir. Bulunan sonuçların analitik açıdan kabul edilebilir hata oranları çerçevesinde standart referans maddenin belgelendirilmiş değerleri ile uyumlu olduğu gözlenmiştir. Bağıl hata oranı her iki toprak referans maddesindeki tayin edilen tüm elementler için %5’ten düşüktür. Bu değer, bu düzeydeki derişimler için kabul edilebilir bir bağıl hata olup, analizin doğruluğunun bir göstergesidir.

Bulunan element derişimleri dikkate alındığında, incelenen elementler arasında tinkal, kolemanit ve bor atığında en bol bulunan element demirdir (tinkalde 7,6 µg/g, üleksitte 8,4 µg/g, kolemanitte 458 µg/g ve bor atığında 77,7 µg/g). Üleksitte ise en bol bulunan element kobalttır (111 µg/g). Bor atığında ve kolemanitteki demir ile üleksitteki Co dışında diğer elementlerin tümü 10 µg/g’ın altındadır.

İncelenen elementler açısından bor atığının, bor mineralleriyle çok farklı olmadığı görülmüştür. Bu nedenle bor atığının da minerallerin kullanıldığı bazı sektörlerde kullanılabileceği söylenebilir.

Teşekkür (Acknowledgment)

Bor mineralleri ve bor atığının temini konusunda katkılarından dolayı Bor Araştırma Enstitüsü (BOREN)'ne teşekkür ederiz.

Kaynaklar (References)

[1] Silva C. D., Santana G. P., Paz S. P. A., Determination of La, Ce, Nd, Sm, and Gd in mineral waste from cassiterite beneficiation by wavelength-dispersive X-ray fluorescence spectrometry, Talanta, 206, 120254, 2020.

[2] Leng C. B., Wang W., Ye L., Zhang X. C., Genesis of the late Ordovician Kukaazi Pb-Zn deposit in the western Kunlun orogen, NW China: New insights from in-situ trace elemental compositions of base metal sulfides, J. Asian Earth Sci., 184, 103995, 2019.

[3] Vanderschueren R., Montalvo D., De Ketelaere B., Delcour J. A., Smolders E., The elemental composition of chocolates is related to cacao content and origin: A multi-element fingerprinting analysis of single origin chocolates, J. Food Compos. Anal., 83, 103277, 2019.

[4] Smrzka D., Zwicker J., Bach W., Feng D., Himmler T., Chen D., Peckmann J., The behavior of trace elements in seawater, sedimentary pore water, and their incorporation into carbonate minerals: a review, Facies, 65 (4), 41-88, 2019.

[5] World Health Organization, Trace-Elements in Human Nutrition, WHO Expert Committee, Geneva, Switzerland, 532, 9-46, 1973.

[6] Bogden J. D., The Essential Trace Elements and Minerals. In: Bogden J.D., Klevay L.M. (eds) Clinical Nutrition of the Essential Trace Elements and Minerals, Nutrition and Health., NJ, A.B.D., 2000.

[7] Bhattacharya P. T., Misra S. R., Hussain, M., Nutritional aspects of essential trace elements in oral health and disease: An extensive review, Scientifica (Cairo), 5464373, 2016.

[8] Jaime S. M., Bruno M. S., Carlos F. F. A., Leonir A. C., Ednei G. P., Marcia F. M., Fabio A., Duarte determination of trace elements in Sergio mirim: an evaluation of sample preparation methods and detection techniques, Environ. Sci. Pollut. Res., 27, 21914-21923, 2020.

[9] Özzeybek G., Alacakoç B., Kocabas M. Y., Bakirdere E. G., Chormey D. S., Bakirdere S., Trace determination of nickel in water samples by slotted quartz tube-flame atomic absorption spectrometry after dispersive assisted simultaneous complexation and extraction strategy, Environ. Monit. Assess., 498, 190, 2018.

[10] Kılıç H. D., Deveci S., Dönmez K. B., Çetinkaya E., Karadağ S., Doğu M., Application of stripping voltammetry method for the analysis of available copper, zinc and manganese contents in soil samples, Int. J. Environ. Anal. Chem., 98, 308-322, 2018.

[11] Koçak, I., Koç S., Major and trace element geochemistry of the Bigadiç Borate deposit, Balikesir, Turkiye, Geochem. Int., 50, 926-951, 2012.

[12] Ertan B., Erdoğan Y., Emet-Espey bölgesindeki borlu killerde eser element tayini, Dumlupınar Üniv. Fen Bilim. Ens. Derg., 33, 25-32, 2014.

[13] Özmal F., Hisarcık-Espey bölgesinde bor endüstri atıklarında eser elementlerin tayini ve lityumun değerlendirilmesi, Doktora Tezi, Dumlupınar Üniversitesi Fen Bilimleri Enstitüsü, Kütahya, 2012.

[14] Helvacı C., Mordoğan H., Çolak M., Gündoğan I., Presence and distribution of lithium in borate deposits and some recent lake waters of west-central Turkey, Int. Geol. Rev., 46 (2), 177-190, 2004.

[15] Erdoğan Y., Mecit A., Demirbaş A., Abalı Y., Analyses of boronic ores and sludges and solubilities of boron minerals in CO_2-saturated water, Resour. Conserv. Recycl., 24, 275-283, 1998.

[16] Durak H., Genel Y., Alban T. C., Kuşlu S., Çolak S., Optimization of the dissolution of tincal ore in phosphoric acid solutions at high temperatures, Chem. Eng. Commun., 202, 245-251, 2015.

[17] Türker A., Türker A. R., A critical review on the determination of boron in various matrices, Boron, 4 (1), 31-38, 2019.

[18] Kmiecik E., Tomaszewska B., Wator K., Bodzek M., Selected problems with boron determination in water treatment processes. Part I: comparison of the reference methods for ICP-MS and ICP-OES determinations, Environ. Sci. Pollut. Res., 23, 11658-11667, 2016.

[19] Peng G.L., He Q., Li H., Mmereki D., Lu Y., Zheng Y., Zhong Z., Lin J., Determination of boron in water samples by dispersive liquid-liquid microextraction based on the solidification of a floating organic drop coupled with a fluorimetric method, Analyst, 141 (7), 2313-2318, 2016.

[20] Floquet C. F. A., Lindvig T., Sieben V. J., MacKay B. A., Mostowfi F., Rapid determination of boron in oilfield water using a microfluidic instrument, Anal. Methods, 9 (12), 1948-1955, 2017.

[21] Abad C., Florek S., Becker-Ross H., Huang M. D., Heinrich H. J., Recknagel S., Vogl J., et al., Determination of boron isotope ratios by high-resolution continuum source molecular absorption spectrometry using graphite furnace vaporizers, Spectrochim. Acta Part B, 136, 116-122, 2017.

[22] Liv L., Nakiboglu N., Voltammetric determination of boron using poly xylenol orange-modified pencil graphite electrode, Anal. Lett., 51, 170-185, 2018.

[23] Erdoğan Y., Yenikaya C., Büyükkıdan N., Kalfa O. M., Determination of the elements in ulexite, tincal and colemanite by ICP-OES spectrometer, II. Uluslararası Bor Sempozyumu, Eskişehir-Türkiye, 541-543, 23-25 Eylül, 2004.

[24] Erdoğan Y., Yenikaya C., Büyükkıdan N., Atar N., Özmal F., Determination of elements in boron industry wastes by ICP-OES spectrometer, II. Uluslararası Bor Sempozyumu, Eskişehir, Türkiye, 525-526, 23-25 Eylül, 2004.

[25] Kılıç E., Eti Maden Kırka Bor İşletmesi Atıklarının Analizi ve Sınıflandırılması, Yüksek Lisans Tezi, Dumlupınar Üniversitesi, Fen Bilimleri Enstitüsü, Kütahya, 2010.

[26] Karabulut A., Budak G., Radioisotope X-ray fluorescence analysis of some elements in colemanite ore, Spectrochim. Acta Part B, 55 (1), 91-95, 2000.

[27] Kalfa O. M., Üstündağ Z, Özkirim İ, Kadioglu Y. K., Analysis of tincal ore waste by energy dispersive X-ray fluorescence (EDXRF) technique, J. Quant. Spectrosc. Radiat., 103 (2), 424-427, 2007.

[28] Çelik A. G., Yörükoğlu A., Sürdem S., Türker A., Erdoğan Y., Bor katkılı pomza tuğla üretimi, fizikomekanik ve kimyasal özelliklerinin belirlenmesi, Boron, 4 (2), 107-118, 2019.

[29] Acar O., Determination of cadmium, chromium, copper and lead in sediments and soil samples by electrothermal atomic absorption spectrometry using zirconium containing chemical modifiers, Anal. Sci., 22, 731-735, 2006.

[30] Trindade A. C., Araújo S. A., Amorium F. A. C., Silva D. S., Alves J. P. S., Trindade J. S., Aguiar R. M., et al., Development of a method based on slurry sampling for determining Ca, Fe and Zn in coffee samples by flame atomic absorption spectrometry. Food Anal. Methods, 13, 203-211, 2020.

BORON 5 (4), 183 - 191, 2020

BOR DERGİSİ
JOURNAL OF BORON
https://dergipark.org.tr/boron

Orta ve şiddetli seviyelerde bor toksisitesinin *Arabidopsis thaliana*’da miR393 ekspresyonu üzerine etkisi

Ceyhun Kayıhan[*]

Başkent Üniversitesi, Fen Edebiyat Fakültesi, Moleküler Biyoloji ve Genetik Bölümü, 06790, Ankara, Türkiye
ORCID ID orcid.org/0000-0003-1684-4147

MAKALE BİLGİSİ

Makale Geçmişi:
İlk gönderi 20 Ağustos 2020
Kabul 11 Kasım 2020
Online 29 Aralık 2020

Araştırma Makalesi

DOI: 10.30728/boron.783209

Anahtar kelimeler:
Arabidopsis thaliana,
Bor,
Ekspresyon,
miR393,
Toksisite.

ÖZET

Bitkilerde korunmuş olan mikroRNA (miRNA) ailelerinden biri olan miR393, birçok kritik gelişimsel süreçlerde rol oynamaktadır. Bu çalışmada, Stem-Loop (SL) kantitatif ters transkripsiyon polimeraz zincir reaksiyonu yöntemi ile 1 mM (1B) ve 3 mM (3B) borik aside maruz kalan *Arabidopsis thaliana*'da miR393’ün ekspresyon seviyeleri belirlenmiştir. Ayrıca, miR393’ün *A. thaliana*’da hedeflediği genler ve bu genlerin Gen Ontoloji (GO) zenginleştirme analizi yapılmıştır. *A. thaliana* bitkisinde toksik seviyelerde bor uygulamaları sonrası, *A. thaliana* fidelerinin gelişiminlerinde gerileme ve fidelerin yaprak uçlarında kloroz gözlemlenmiştir. *A. thaliana*’da 1B uygulaması miR393 ekspresyonu 2,9 kat artırırken, 3B uygulaması 2,7’lik bir artışa sebep olmuştur. miR393’ün 5’ ve 3’ ucundaki olgun dizilere göre başlıca hedef genleri; auxin sinyal F-box, S-adenosil-L-metiyonin-bağımlı metiltransferaz süper familya proteinlerini, Kinezin benzeri kalmodulin-bağlanma proteinlerini, Lösin-zengin reseptör benzeri protein kinaz familya proteinlerini, 1-deoksi-D-ksilüloz 5-fosfat sentaz enzimini, ARM tekrar süper familya proteinlerini ve myb-benzeri HTH transkripsiyonel regülatör familya proteinlerini kodlayan genler ve bHLH ve WRKY33 transkripsiyon faktörleridir.Öte yandan, miR393’ün hedeflediği genlerin GO zenginleştirme analizine göre başlıca Biyolojik Süreçleri şu şekildedir: Oksin ile aktifleşmiş sinyal yolağı, oksin uyarısına hücresel cevap, çeşitli gelişim süreçleri ve farklı hücresel cevaplardır. Moleküler Fonksiyonlar ise, oksin bağlayıcı, inositol heksakisfosfat bağlayıcı ve hormon ve alkol bağlayıcı şeklinde kategorize edilebilir. Sonuç olarak, bor toksisitesi altında tespit edilen büyüme geriliği, miR393 hedefli oksin regülasyonu ve bHLH gibi ilişkili transkripsiyon faktörleri ile ilgili olabilir.

Effect of of boron toxicity on miR393 expression at moderate and severe levels in *Arabidopsis thaliana*

ARTICLE INFO

Article history:
Received August 20, 2020
Accepted November 11, 20200
Available online December 29, 2020

Research Article

DOI: 10.30728/boron.783209

Keywords:
Arabidopsis thaliana,
Boron,
Expression,
mir393,
Toxicity.

ABSTRACT

miR393, one of the microRNA (miRNA) families preserved in plants, plays a role in many critical developmental processes. In this study, expression levels of miR393 were determined in *Arabidopsis thaliana* exposed to 1 mM (1B) and 3 mM (3B) boric acid by Stem-Loop (SL) quantitative reverse transcription polymerase chain reaction method. In addition, genes targeted by miR393 in *A. thaliana* and Gene Ontology (GO) enrichment analysis of these genes were performed. After application of toxic levels of B in *A. thaliana* plant, a decrease in the growth of *A. thaliana* seedlings and chlorosis on the leaf tips of the seedlings were observed. While 1B application caused a 2.9 fold increase in miR393 expression, 3B application caused a 2.7 fold increase in this expression. According to the mature sequences at the 5 'and 3' ends of miR393, the main target genes are; genes coding Auxin signaling F-box, S-adenosyl-L-methionine-dependent methyltransferases superfamily protein, kinesin-like calmodulin-binding protein, Leucine-rich receptor-like protein kinase family protein, 1-deoxy-D-xylulose 5-phosphate synthase 3, ARM repeat superfamily protein, myb-like HTH transcriptional regulator family protein and bHLH, and WRKY33 transcription factors. On the other hand, according to the GO enrichment analysis, the main Biological Processes of the genes targeted by miR393 are as follows: The auxin-activated signaling pathway, the cellular response to auxin, various developmental processes, and different cellular responses. Molecular functions can be categorized as auxin binding, inositol hexakisphosphate binding and hormone and alcohol binding. As a result, growth retardation detected under boron toxicity may be related to miR393 targeted auxin regulation and associated transcription factors such as bHLH.

---

[*]Sorumlu yazar: ckayihan@baskent.edu.tr

1. Giriş (Introduction)

Bor (B), bitkiler için mutlak gerekli mikro besin elementidir [1]. Bununla birlikte, yüksek bor seviyesi, dünyadaki önemli abiyotik stres faktörlerinden biridir ve bitki gelişimi ile mahsul verimini olumsuz etkilemektedir [2]. Birçok ülke, özellikle kurak veya yarı kurak topraklara sahip olanlar, aşırı bor sebebiyle verim kaybından muzdariptir [3]. Bor, büyüme için gerekli seviyenin çok az üstünde bile olsa, birçok bitki için kolayca toksik olabilir [4]. Bor toksisitesi, hücre duvarı yapısında değişikliklere ve borun biyolojik moleküllerin ribozlarına bağlanması nedeniyle, hücre bölünmesinin ve gelişiminin bozulasına neden olur [5]. Tipik olarak, toksik bor, gövde ve kök büyümesinde inhibisyona ve eski yaprakların uçlarında ve kenarlarında klorotik veya nekrotik bölgelerle ayırt edilen yaprak yanmasına yol açar [6,7]. Çoğu bitki türünde, bor kökler tarafından emildikten sonra, ksileme yüklenir ve transpirasyon akışı yoluyla gövdeye geçer ve yeniden dağıtılmadan eski yapraklarda birikir; bu nedenle yapraklardaki bor içeriği ile toksisite semptomlarının şiddeti arasında doğrudan bir ilişki vardır [8]. Bor toksisitesi altında köke ve gövdeye özgü akuaporinleri kodlayan genlerin aşağı regülasyonu, hücreden hücreye su hareketinde azalmaya ve gövdelere su akışında azalmaya neden olmaktadır [9]. Bu nedenle, yaprak ve gövdede bor toksisite semptomları köklerden daha şiddetlidir. Borun toksik etkileri devam ederse, boron cis konfigürasyonlu moleküllerde çoklu hidroksil gruplarına karşı yüksek reaktivitesi nedeniyle azot ve şeker metabolizmasının baskılanma durumu gelişir [10]. Bu sitotoksik etkiler, metabolik bozukluğa ve oksidatif strese neden olur [10]. Öte yandan, aşırı bor varlığında, bitki inhibisyonu nedenlerinden bir diğeri foto-oksidatif strestir [5] ve oksidatif stres sonucu reaktif oksijen türlerinin (ROS) aşırı birikimi, pigmentleri, lipidleri, nükleik asitleri, proteinleri ve inaktive edici enzimleri oksitleyerek hücre ölümüne neden olabilir [11]. Bitkiler, ROS birikimine karşı antioksidan enzimleri içeren süpürücü mekanizmalarına sahiptir. İlişkili olarak, domateste, antosiyaninin ve flavonoidin artmış seviyesi [12], fesleğende daha yüksek fenolik içerik [13], ve nohutta ve soya fasülyesinde, süperoksit dismutaz (SOD; EC 1.15.1.1), katalaz (CAT; EC 1.11.1.6), ve askorbat peroksidaz (APX; EC 1.11.1.11) aktivitelerinde anlamlı artışlar [14], toksik bor koşulları altında belirlenmiştir.

Bor toksisitesine karşı bitki toleransı, türler hatta çeşitler arasında bile büyük farklılıklar göstermektedir [3]. Bitkilerde bor toksisitesine karşı toleransın altında yatan mekanizmalar hala tartışmalıdır. Otsu bitki türleri için önerilen en yaygın kabul gören teori, bor dışa akış taşıyıcıları yoluyla hücreler arası bor seviyelerinin azaltılmasıdır. Örneğin; arpada (*Hordeum vulgare*), köklerdeki bor dışa akım taşıyıcısı *BOR1*'in yukarı regülasyonu, borun topraktan emilimini azaltır [15]. Buna karşın; *BOR1*'e homolog olan *BOR2*'nin yapraklardaki yukarı regülasyonu, borun simplastlardan apoplastlara taşınmasına neden olur [16]. Benzer şekilde, köklerdeki başka bir dışarı akış taşıyıcısı olan nodulin benzeri iç proteinin (NIP) aşağı regülasyonu da borun köklerden gövdelere taşınmasını azaltarak, yer üstü bitki parçalarında bor birikimini azaltmaktadır [17]. Öte yandan, yakın bir zamanda yapılan fizyolojik bir çalışma fesleğenin bor toksisitesine karşı tolerans mekanizmalarında yaprak antosiyaninleri tarafından foto korumanın rol oynadığı göstermiştir [18]. Bu durum, bor toksisitesine karşı farklı mekanizmaların rol oynayabileceğini göstermiştir.

Omiks teknolojileri ile yapılan son moleküler çalışmalar, toksik borun yanıtları ve biyolojik yolaklarla olası ilişkileri hakkında önemli bilgiler sağlamıştır [19,20]. Önemli olarak, bu çalışmalarda, bor homeostazisinin WRKY, MYB ve NAC gibi transkripsiyon faktörlerindeki değişiklikler ile düzenlendiğini öne sürülmüştür. Ayrıca, temel heliks-döngü-heliks aile proteininin (bHLH) ekspresyon seviyesi, bor toksisitesi altında hassas ve tolerant buğday çeşitlerinin yaprak ve kök dokularında aşağı yönlü regüle olduğu ve bu transkripsiyon faktörünün, bitkilerdeki bor toksisitesi yanıtına katılabileceği bildirilmiştir [20]. Bununla birlikte, stres sırasında genlerin nasıl regüle olduğu sorusunu cevaplamak, yeni genler bulmak kadar önemlidir [21]. Bundan dolayı, mikroRNA’lar (miRNA), post-transkripsiyonel seviyede gen ekspresyonunun anahtar düzenleyicileri olarak, stres ağını keşfetmek için iyi adaylardır. Bu kodlanmayan küçük RNA’lar, 21 ila 24 nükleotid uzunluğunda, bitkilerde geniş bir dağılıma sahiptir. Bu miRNA’lar, bitkilerde, doğrudan hedef mRNA’yı susturarak ya da hedef mRNA'nın translasyonunu inhibe ederek genlerin ekspresyonlarını negatif yönlü regüle ederler [22]. Kanıtlar, bitki miRNA'larının bitki büyümesinin ve gelişiminin düzenlenmesinde ve ayrıca biyotik ve abiyotik streslere yanıtta çok önemli bir rol oynadığını göstermektedir [23]. Örneğin, *A. thaliana*'da miR399'un *UBC24* transkript seviyesini düzenleyerek fosfor (P) homeostazını sağladığı deneysel olarak kanıtlanmıştır [24]. Buna karşın, miR395, sırasıyla *APS* ve *SULTR2;1*'i hedefleyerek, sülfat (S) birikimi ve dağılımını düzenlenmesine aracılık etmektedir [25]. Benzer şekilde, artan kanıtlar, bitki miRNA'larının bor streslerine yanıtta çok önemli bir rol oynadığını göstermektedir [26]. Örneğin, daha önce yapılan bir çalışmada, narenciye yapraklarında miR397a’nın ksilemin ikincil hücre duvarı biyosentezini düzenleyerek bor toksisitesinin bitkiye olan etkisinin azaltılmasında rol oynadığı bildirilmiştir [27]. Bu nedenle, bitkide bor toksisitesine cevaben değişen miRNA’ların belirlenmesi tolerans mekanizmasının belirlenmesi için önem arz etmektedir. Bu çalışmada, literatürde ilk defa oksin reseptörleri *TIR1*, *AFB1*, *AFB2* ve *AFB3*’ü ve aşağı yönlü regüle olduğu daha önce belirlenen bHLH transkripsiyon faktörünü hedefleyen miR393’ün ekspresyon seviyeleri 1 mM (1B) ve 3 mM (3B) borik aside maruz kalan *A. thaliana*'da olgun miRNAları tespit etmek ve çoğaltmak için önemli bir strateji olan Stem-loop (SL) kantitatif ters transkripsiyon polimeraz zincir reaksiyonu yöntemi [28,29] ile belirlenmiştir. Bu yöntemde, bir saç tokası yapısı olarak tasarlanan SL primeri, miRNA'ya komplementer olan 3' çıkıntıya sahiptir. Daha sonra, miRNA-spesifik primerler ve bir evrensel primer, olgun miRNA'nın polimeraz zincir reaksiyonu (PZR) ile amplifikasyonu için kullanılır [30]. Ayrıca, bu çalışmada miR393'ün *A. thaliana*'da diğer hedeflediği genler ve bu genlerin Gen Ontoloji (GO) Zenginleştirme analizi yapılmıştır.

2. Malzemeler ve yöntemler (Materials and methods)

2.1. Büyüme koşulları ve bor uygulamaları (Growth conditions and boron treatments)

Büyütme koşulları ve bor uygulamaları için Arabidopsis (*A. thaliana* Columbia ekotipi) tohumlarının, önce %70'lik etil alkol ile 2 dakika, ardından %15'lik sodyum hipoklorit çözeltisi ile 10 dakika yıkanarak yüzeyleri sterilize edilmiştir. Ardından tohumlar distile su ile 3 kez durulanmıştır ve normal (100 µM) ve toksik (1 mM ve 3 mM H_3BO_3) B konsantrasyonları içeren MS besiyerine [31] transfer edilmiştir. 3 günlük, 4°C'deki vernelizasyonun ardından çimlenme ve büyüme 22°C'de iklim kabininde, 16/8-h ışık fotoperiyodu ile gerçekleştirilmiştir. İki haftanın ardından fideler hasat edilmiştir ve ileri analizler için kullanılmıştır.

2.2. Kantitatif gerçek zamanlı PZR koşulları (Quantitative real-time PCR conditions)

İki haftalık *A. thaliana* fidelerinden TRIzol reaktifi (Ambion) ile toplam RNA izole edilmiştir. İzolasyon protokolü şu şekildedir: 0,2 gram *A. thaliana* yaprakları sıvı nitrojen ile havanda öğütülmüş ve toz haline gelen yaprak örneği önceden soğutulmuş eppendorf tüplerine transfer edilmiştir. Ardından, 1 ml TRIzol reaktifi tüplere eklenmiş ve 15 dakika boyunca oda sıcaklığında tüpler vorteks ile karıştırılmış ve devamında tüpler 5 dakika boyunca oda sıcaklığında maksimum hızda santrifüjlenmiştir. Santrifüj sonrası elde edilen süpernatanttan 900 µl yeni tüplere aktarılmış ve üzerine 180 µl kloroform eklenmiş ve tüpler vortekslenerek 3 dakika boyunca oda sıcaklığında inkübe edilmiştir. İnkübasyon sonunda tüpler, 4°C'de maksimum hızda 15 dakika santrifüjlenmiştir. Elde edilen süpernatanttan 450 µl yeni tüplere aktarılmış ve üzerine 200 µl kloroform eklenmiştir. Tüpler vorteklenerek oda sıcaklığında 3 dakika boyunca inkübe edilmiştir. Ardından, tüpler, oda sıcaklığında 5 dakika boyunca maksimum santrifüjlenmiştir ve üst fazdan 400 µl alınarak yeni tüpe transfer edilmiştir ve üzerine eşit hacimde izopropanol eklenmiş ve tüpler birkaç kez tersyüz edilerek, 10 dakika boyunca oda sıcaklığında inkübe edilmiştir. Tüpler 10 dakika boyunca oda sıcaklığında maksimum hızda santrifüjlenmiş ve elde edilen pelet 1 ml %75'lik etanol ile 3 dakika boyunca yıkanmıştır. Daha sonra, 5 dakika boyunca oda sıcaklığın maksimum hızda santrifüjlene pelet 10 dakika boyunca kurumaya bırakılmıştır. Son olarak, kurutulan pelet üzerine 50 µl Dietil Pirokarbonat'lı su eklenmiş ve 65°C'de 15 dakika boyunca inkübe edilerek çözülmüştür. RNA'nın sağlamlığı ve kalitesini kontrol etmek için agaroz jel elektroforezi kullanılmıştır. Ardından RNA saflığı ve konsantrasyonu NanoDrop (Denovix, ABD) ile belirlenmiştir. İzole edilen toplam RNA'lar kullanıma kadar -80°C'de saklanmıştır.

miRBase veritabanı, miR393 sekansını elde etmek üzere kullanılmıştır. SL-geri transkripsiyon ve ileri primerler [32] protokolüne uygun bir şekilde özel olarak tasarlanmıştır. miR393 için primer sekansları Tablo 1'de verilmiştir. miR393 ekspresyonu, kantitatif gerçek zamanlı PZR (qRT-PCR) metodu ile belirlenmiştir [33]. Öncelikle, 1 µg RNA, RNaz içermeyen su, 2 µL SL primeri içeren 12 µL'lik karışımlar hazırlanmıştır. Bu karışımlar, 5 dakika 65°C'de, ardından 2 dakika buzda inkübe edilmiştir. Sonrasında, 5X reaksiyon tamponu, RiboLock RNaz inhibitörü (20 U/µL), 10 mM dNTP ve ters transkriptaz karışımlara eklenmiştir. Karışımlar 30 dakika boyunca 16°C'de inkübe edilmiştir ve 60 döngü boyunca 30°C'de 30 s, 42°C'de 30 s ve 50°C'de 1 s olarak şekilde atımlı geri transkripsiyona maruz bırakılmıştır. Ardından tüpler 70°C'de 5 dakika inkübe edilmiştir. qRT-PCR analizleri için, 1 µL cDNA, 7 µL 2X Master Mix (Thermo Scientific) ve final konsantrasyon 0,3 µM olacak şekilde primerler eklenerek total hacim nükleazsız su ile 15 µL'ye tamamlanmıştır. qRT-PCR koşulları, 95°C'de 10 dakika ilk denatürasyon, ardından 40 döngü 95°C'de 15 s, 59°C'de 30 s, 72°C'de 30 s olarak belirlenmiştir. Erime eğrisi (melting curve) 40 döngü sonrası 60-95°C'de analiz edilmiştir. Normalizasyon aktin (*ACT2*) geni kullanılarak gerçekleştirilmiştir [20] ve $2^{-\Delta\Delta Ct}$ her bir karşılaştırmada ekspresyon kat farklılıklarını belirlemek üzere kullanılmıştır.

Tablo 1. miR393 ekspresyon analizi için kullanılan primerler (Primers used for miR393 expression analysis).

Primer İsmi	5' – 3' yönünde sekans
miR393-SL-RT	GTCGTATCCAGTGCAGGGTCCGAGGTATTCGCACTGGATACGACGGATCA
miR393_F	CGTAATTCCAAAGGGATCGCAT
Universal_R	GTGCAGGGTCCGAGGT
ACT2_F	CTTGACCTTGCTGGACGTGA
ACT2_R	AATTTCCCGCTCTGCTGTTG

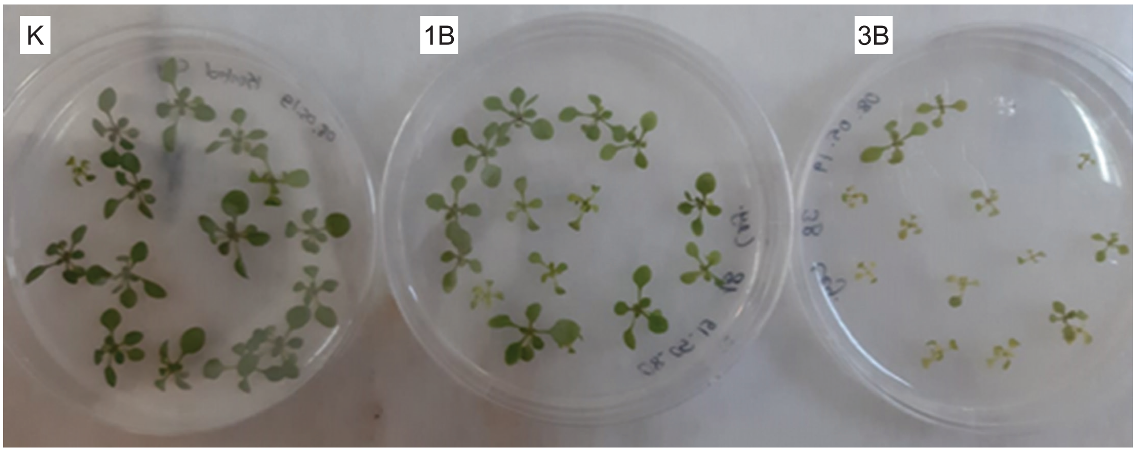

Şekil 1. Toksik B uygulamalarına maruz kalmış *Arabidopsis thaliana* fidecikleri. K: kontrol, 1B: 1 mM H_3BO_3 uygulaması, 3B: 3 mM H_3BO_3 uygulaması.(*Arabidopsis thaliana* seedlings exposed to toxic B treatments. K: control, 1B: 1 mM H_3BO_3 treatment, 3B: 3 mM H_3BO_3 treatment).

2.3. miR393 hedef genlerinin bilgisayımsal tahmini ve GO zenginleştime analizi (Computational prediction of target genes of miR393 and GO enrichment analysis)

A. thaliana'da miR393'ün hedeflerini belirlemek için, olgun miRNA dizileri miRBase veri tabanı kullanılarak (sürüm 22.1, http://www.mirbase.org/) belirlenmiştir [34]. Daha sonra, bu olgun miR393 dizileri kullanılarak miR393 hedef genleri psRNATarget veri tabanında belirlenmiştir (version 2, http://plantgrn.noble.org/psRNATarget/) [35].

miR393'ün belirlenen hedef genlerinin GO zenginleştime analizi 10.08.2020 tarihinde güncellenen PANTHER veritabanı kullanılarak (sürüm 14, http://geneontology.org/) yapılmıştır [36]. Referans liste *A. thaliana* seçilerek yapılmıştır. GO biyolojik süreç ve moleküler fonksiyon sonuçları test tipi Fisher's exact ve doğrulama FDR seçilerek yapılmıştır (P<0,05).

2.4. İstatistiksel analizler (Statistical analyses)

qRT-PCR deneyleri, dört biyolojik tekrar olarak gerçekleştirilmiştir (n=4). Veriler istatistiksel olarak t-testinin parametrik olmayan versiyonu kullanarak analiz edilmiştir. Öte yandan, yaprak alanı verileri, dört biyolojik tekrar ve her tekrardan en az 10 bitki olacak şekilde Java tabanlı ImageJ programı kullanılarak elde edilmiştir. Yaprak alanı verileri, *SPPS* istatistik programı kullanılarak Tek Yönlü Varyans Analizi (ANOVA) ile analiz edilmiştir. Veriler, ortalama ve standart hata birlikte olacak şekilde verilmiştir.

3. Bulgular (Results)

A. thaliana bitkisinde toksik seviyelerde bor uygulamaları sonrası, *A. thaliana* fidelerinin gelişimlerinde gerileme ve fidelerin yaprak uçlarında kloroz gözlemlenmiştir (Şekil 1). Hatta beklendiği üzere, yaprak alanı verilerine göre bor toksisitesinin artan konsantrasyonuna karşılık, *A. thaliana* yapraklarında kısmi sararma ve büyüme geriliği artmıştır (Şekil 2). Öte yandan, *A. thaliana*'da 1B uygulaması miR393 ekspresyonu 2,9 kat artırırken, 3B uygulaması 2,7'lik bir artışa sebep olmuştur (Şekil 3).

miR393'ün 5' ve 3' ucundaki olgun dizilere göre (5p ve 3p) başlıca hedef genleri; auxin sinyal F-box, S-adenosil-L-metiyonin- bağımlı metiltransferaz süper familya proteinlerini kodlayan genler, Kinezin benzeri kalmodulin-bağlanma proteinlerini kodlayan genler, Lösin-zengin reseptör benzeri protein kinaz familya proteinlerini kodlayan genler, 1-deoksi-D-ksilüloz 5-fosfat sentaz enzimini kodlayan gen, ARM tekrar süper familya proteinlerini kodlayan genler, myb-benzeri HTH transkripsiyonel regülatör familya proteinlerini kodlayan genler ve bHLH, ve WRKY33 transkripsiyon faktörleridir (Tablo 2). Öte yandan, miR393'ün hedefle-

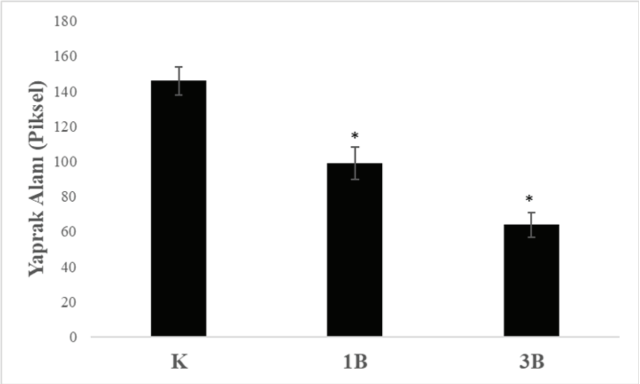

Şekil 2. Toksik B uygulamaları altında Arabidopsis thaliana'nın yaprak alanında (piksel) değişim. K: Kontrol, 1B: 1 mM H_3BO_3 uygulaması, 3B: 3 mM H_3BO_3 uygulaması. Ondört bağımsız biyolojik tekrardan gelen ortalama ve standart hata gösterilmektedir (p<0,05). Hata çubukları üzerindeki yıldız işareti (*) kontrole göre istatistiksel olarak anlamlı olduğunu göstermektedir. (Changes in leaf area (pixel) in *Arabidopsis thaliana* under toxic B treatments. K: control, 1B: 1 mM H_3BO_3 treatment, 3B: 3 mM H_3BO_3 treatment. The mean and standard error from fourteen independent biological replicates are shown (p<0.05). An asterisk above the error bars represents significant differences between control and B-toxicity–treated samples.).

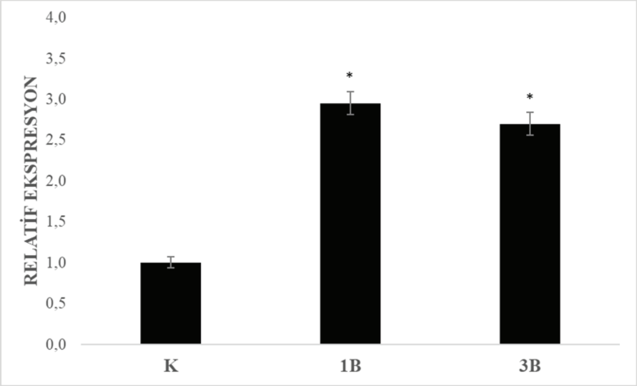

Şekil 3. *Arabidopsis thaliana*'da toksik B uygulamaları altında miR393'ün ekspresyon seviyelerindeki değişim. K: Kontrol, 1B: 1 mM H_3BO_3 uygulaması, 3B: 3 mM H_3BO_3 uygulaması. Üç bağımsız biyolojik tekrardan gelen ortalama ve standart hata gösterilmektedir (p<0,05). Hata çubukları üzerindeki yıldız işareti (*) kontrole göre istatistiksel olarak anlamlı olduğunu göstermektedir. (Changes in expression level of miR393 in *Arabidopsis thaliana* under toxic B treatments. K: control, 1B: 1 mM H_3BO_3 treatment, 3B: 3 mM H_3BO_3 treatment. The mean and standard error from three independent biological replicates are shown (p<0.05).) An asterisk above the error bars represents significant differences between control and B-toxicity–treated samples.

diği genlerin GO zenginleştirme analizine göre başlıca Biyolojik Süreçleri şu şekildedir: Polen matürasyonu, Oksin ile aktifleşmiş sinyal yolağı, Oksin uyarısına hücresel cevap, SCF-bağımlı proteozomal ubikuitin-bağımlı protein katabolik süreç, Stamen gelişimi, Floral organ gelişimi, Gelişimsel matürasyon, Proteazom aracılı ubikuitin bağımlı protein katabolik süreç, Çiçek gelişimi, Oksin yanıtı, Hormon aracılı sinyal yolağı, Hormon uyarısına hücresel cevap, Organik maddeye hücresel cevap, Hücresel makromolekül katabolik süreç, Hormon cevabı, Endojen uyaran cevabı ve Organik madde cevabı (Tablo 3). miR393'ün hedeflediği genlerin Gen Ontoloji (GO) Zenginleştirme analizine göre Moleküler Fonksiyonları, Oksin bağlayıcı, İnositol heksakisfosfat bağlayıcı ve Hormon ve alkol bağlayıcı şeklinde kategorize edilebilir (Tablo 4).

4. Tartışma (Discussion)

Bitki miRNA'ların 2002'de önemli bir post-transkripsiyonel düzenleyici olarak bulunuşunun ardından [37] bitki büyüme ile gelişiminde önemli rollerinin önerilmesiyle [38], çevresel strese cevaba olan katkılarının ileri ki çalışmalarla incelenmesi [39,40] miRNA'ları gündemde önemli bir yere getirmiştir. Bu çalışmalarda miRNA'ların bitkilerdeki birçok çevresel stresin adaptif cevabında bulunduğunu öne sürülmüştür [41,42]. Literatürde ilk olacak şekilde, arpa [43] ve turunçgillerde [44] bor toksisitesine cevapta bazı miRNA'nın değiştiği belirlenmiştir. Ayrıca, çok yakın zamanda, toksik bor koşullarına maruz kalan *A. thaliana*'da jasmonat ve etilen mekanizmalarıyla ilişkili olan transkripsiyon faktörlerinin hedeflendiği miRNA'ların ekspresiyon seviyeleri belirlenmiştir [45]. Buna göre; miR159, miR319, miR394 ve miR172 ekspresyon seviyeleri orta seviyede bor toksisitesi altında dramatik bir şekilde artarken, daha şiddetli B toksisitesi uygulaması altında ilginç bir şekilde bu miRNA'ların ekspresyonu kontrol koşullarına göre değişmediği önerilmiştir. Bu çalışmada ise; literatürde ilk defa miR393'ün ekspresyon seviyesi *A. thaliana*'da 1 ve 3 mM B koşulları altında belirlenmiştir. Buna göre *A. thaliana*'da orta ve şiddetli seviyelerde toksik bor uygulamaları, miR393'ün ekspresiyonunu yaklaşık 3 kat arttırmıştır. *A. thaliana*'da mirR393'ün başlıca hedefleri oksin reseptörlerini kodlayan F-box genleri (Transport Inhibitor Response Protein1 (*TIR1*), Auxin Signaling F Box Protein 2 (*AFB2* ve *AFB3*)) ve bHLH transkripsiyon faktörüdür [46-48] (Tablo 3). İlişkili olarak, bir önceki çalışmamızda bHLH ekspresyon

Tablo 2. miR393'ün olası hedeflediği genlerden bazıları. ath-miR393a-5p: UCCAAAGGGAUCGCAUUGAUCC, ath-miR393a-3p: AUCAUGCUAUCUCUUUGGAUU, AGI: Arabidopsis Genome Initiative, (Some of the possible target genes of miR393).

miRNA	Hedef Gen AGI Kodu	Beklenen Değer	Hedef Gen Tanımı
ath-miR393a-5p	AT1G12820	1.0	auxin sinyal F-box 3 (AFB3)
ath-miR393a-5p	AT3G26810	1.0	auxin sinyal F-box 2 (AFB2)
ath-miR393a-5p	AT3G62980	1.0	F-box/RNI benzeri süper familya protein (TIR1)
ath-miR393a-3p	AT1G26850	2.0	S-adenosil-L-metiyonin- bağımlı metiltransferaz süper familya p
ath-miR393a-5p	AT4G03190	2.0	GRR1-benzeri protein 1 (GRH1)
ath-miR393a-5p	AT3G23690	2.5	basic helix-loop-helix (bHLH) DNA-bağlanma süper familya pr
ath-miR393a-3p	AT5G65930	3.0	Kinezin benzeri kalmodulin-bağlanma proteini
ath-miR393a-3p	AT3G19420	3.0	PTEN 2
ath-miR393a-5p	AT2G38470	3.0	WRKY DNA-bağlanma protein 33 (WRKY33)
ath-miR393a-5p	AT5G65700	3.0	Lösin-zengin reseptör benzeri protein kinaz familya proteini (BA
ath-miR393a-5p	AT2G24210	3.0	Terpen sentaz 10 (TPS10)
ath-miR393a-5p	AT5G11380	3.0	1- deoksi-D-ksilüloz 5-fosfat sentaz 3 (DXPS3)
ath-miR393a-3p	AT1G61350	3.5	ARM tekrar süper familya proteini
ath-miR393a-3p	AT3G23020	3.5	Tetrarikopeptid tekrar (TPR) benzeri süper familya proteini
ath-miR393a-3p	AT3G13040	3.5	myb-benzeri HTH transkripsiyonel regülatör familya proteini

Tablo 3. miR393'ün hedeflediği genlerin GO zenginleştirme biyolojik süreç analizi (GO enrichment biological process analysis of genes targeted by miR393).

GO: Biyolojik Süreç	Kat Zenginleştirme	İşlenmemiş p-değeri
Polen matürasyonu	> 100	9.42E-10
Oksin ile aktifleşmiş sinyal yolağı	> 100	2.48E-08
Oksin uyarısına hücresel cevap	90.93	1.23E-07
SCF-bağımlı proteozomal ubikuitin-bağımlı protein katabolik süreç	72.53	2.92E-07
Androecium gelişimi	72.53	7.77E-09
Stamen gelişimi	72.53	7.77E-09
Floral whorl development	39.46	1.48E-07
Floral organ gelişimi	31.34	4.51E-07
Gelişimsel matürasyon	30.93	7.90E-06
Proteazom aracılı ubikuitin bağımlı protein katabolik süreç	24.18	2.04E-05
proteazomal protein katabolik süreç	22.82	2.56E-05
Çiçek gelişimi	21.51	2.78E-06
Üreme sürgün sistem gelişimi	20.64	3.39E-06
Oksin yanıtı	20.38	3.95E-05
Hormon aracılı sinyal yolağı	18.00	6.54E-06
Polen gelişmi	17.61	6.92E-05
Gametofit gelişimi	16.52	9.88E-06

Tablo 4. miR393'ün hedeflediği genlerin GO zenginleştirme moleküler fonksiyon analizi. (GO enrichment molecular function analysis of genes targeted by miR393).

GO: Moleküler Fonksiyon	Kat Zenginleştirme	İşlenmemiş p-değeri
Oksin bağlayıcı	> 100	6.40E-11
Inositol heksakisfosfat bağlayıcı	> 100	1.14E-09
Hormon bağlayıcı	> 100	7.54E-09
Alkol bağlayıcı	> 100	1.58E-08

seviyesi, bor toksisitesi altında hassas ve tolerant buğday çeşitlerinin yaprak ve kök dokularında aşağı yönlü regüle olduğu ve bu transkripsiyon faktörünün, bitkilerdeki bor toksisitesi yanıtına katılabileceği bildirilmiştir [20]. miR393 ve hedef genlerinin düzenleyici modülünün kök yapısının kontrolü [49], yaprak gelişiminin düzenlenmesi [50] ve normal bitki büyümesinin sağlanması [51] gibi oksin cevabını manipüle eden birçok fonksiyonu olduğu keşfedilmiştir [52]. Bu miRNA'nın aynı zamanda biyotik ve abiyotik stres ile yakından ilişkili olduğu belirlenmiştir [53,54]. Pirinçte yapılan benzer araştırmalar, miR393'ün biyolojik fonksiyonlarının ve oksin yolağı ile düzenlenme mekanizmasının yüksek bitkilerde korunmuş olduğunu kanıtlamıştır [55-57]. B toksisitesine benzer şekilde, miR393'ün *A. thaliana*'da [53], pirinçte [58] ve şeker kamışında (*Saccharum spp.*) [59] kuraklık stresi sırasında yukarı yönlü regüle olduğu bildirilmiştir.

miR393'ün hedefi, *A. thaliana*'da oksin reseptörü olan TIR1'i kodlar. TIR1 enzimi ubikitinasyon yolu ile Aux/IAA proteinlerinin degredasyonunu destekleyerek oksin sinyallenmesinin pozitif bir regülatörüdür [60]. Yakın zamanda yapılan bir çalışmada miR393'ün aşırı eksprese edildiği pirinç fidelerinin büyümesinin 1 günlük kuraklık uygulamasıyla kontrol bitkilerine kıyasla bastırıldığı bildirmiştir [57]. miR393'ü aşırı eksprese eden pirinçler aynı zamanda sentetik oksin analog uygulamalarına karşı aşırı duyarlılık göstermiştir [57]. Bu nedenle, artan miR393 seviyeleri, oksin sinyallenmesini aşağı regüle eder ve kuraklık stresi altında bitki büyümesini azaltabilir. Ayrıca, miR393'ün inhibe edildiği transgenik *A. thaliana* bitkisinde yaban tipe göre *AtTIR1*, *AtAFB1*, *AtAFB2*, ve *AtAFB3* ekspresyonları artmış ve bu transgenik bitkilerin tuz ve absisik ait streslerine karşı dirençleri artmıştır [61]. Dolayısıyla, *A. thaliana* bitkisinde miR393'ün kısmı de olsa fonksiyon kaybı tuz stresine karşı tolerans kazandırmıştır [61]. Kuraklık stresine ve tuz streslerine benzer şekilde, bor toksisitesi altında tespit edilen büyüme geriliği, miR393 hedefli oksin reseptör regülasyonu ve bHLH transkripsiyon faktörü ile ilişkili olabilir. Bu nedenle, miR393 inhibisyonuna yönelik yaklaşımlar, bor toksisitesine karşı tolerant bitkiler yetiştirme amacıyla kullanılabilir.

5. Sonuçlar (Conclusions)

Sonuç olarak, bor toksisitesinin artan konsantrasyonuna karşılık, *A. thaliana* yapraklarında kısmi sararma ve büyüme geriliği artmıştır. Öte yandan, *A. thaliana*'da 1B ve 3B uygulamaları, miR393 ekspresyonunu 3 kata yakın artışa sebep olmuştur. Bor toksisitesi altında tespit edilen büyüme geriliği, miR393 hedefli oksin reseptör regülasyonu ve bHLH transkripsiyon faktörü ile ilişkili olabilir. Dolayısıyla, miR393 inhibisyonuna veya *AtTIR1*, *AtAFB1*, *AtAFB2*, ve *AtAFB3* aşırı ekspresyonuna yönelik yaklaşımlar bor toksisitesine karşı tolerant bitkiler yetiştirme amacıyla kullanılabilir.

Teşekkür (Acknowledgement)

Bu çalışmanın oluşmasında desteklerinden dolayı Dr. Doğa Selin KAYIHAN'a ve öğrencilerim Su Naz MUTLU, Irmak YILMAZ ve Melis Vuslat TUNÇ'a teşekkür ederim.

Kaynaklar (References)

[1] Warington K., The effect of boric acid and borax on the broad bean and certain other plants, Ann. Bot., 37, 629-672, 1923.

[2] Landi M., Degl'Innocenti E., Pardossi A., Guidi L., Antioxidant and photosynthetic responses in plants under boron toxicity: a review, Am. J. Agric. Biol. Sci., 7 (3), 255-270, 2012.

[3] Nable R. O., Ba~nuelos G. S., Paull J. G., Boron toxicity, Plant Soil, 193, 181-198, 1997.

[4] Mengel K., Kirkby E. A., Principles of Plant Nutrition, 5th edition, Springer, Hollanda, 2001.

[5] Reid R., Hajes J. E., Post A., Stangoulis J. C. R., Graham R. D., A critical analysis of the causes of boron toxicity in plants, Plant Cell Environ., 25, 1405-1414, 2004.

[6] Bennett W. F., Nutrient Deficiencies and Toxicities in Crop Plants, 1st Edition, APS, A.B.D., 1993.

[7] Fitzpatrick K. L., Reid R. J., The involvement of aquaglyceroporins in transport of boron in barley roots, Plant Cell Environ., 32, 1357-1365, 2009.

[8] Reid R., Understanding the boron transport network in plants, Plant Soil, 385, 1-13, 2014.

[9] Macho-Rivero M. A., Herrera-Rodríguez M. B., Brejcha R., Schäffner A. R., Tanaka N., Fujiwara T., González-Fontes A., et al., Boron toxicity reduces water transport from root to shoot in Arabidopsis plants. Evidence for a reduced transpiration rate and expression of major PIP aquaporin genes, Plant Cell Physiol., 59, 841-849, 2018.

[10] Princi M. P., Lupini A., Araniti F., Longo C., Mauceri A., Sunseri F. Abenavoli M. R., Plant Metal Interaction, Chap. 5: Boron Toxicity and Tolerance in Plants: Recent Advances and Future Perspectives, Elsevier, 2016.

[11] Blokhina O., Virolainen E., Fagerstedt K. V., Antioxidants, oxidative damage and oxygen deprivation stress: a review, Ann. Bot., 91, 179-194, 2003.

[12] Cervilla L. M., Blasco B., Rios J. J., Rosales M. A., Sanchez-Rodriguez E., Rubio-Wilhelmi M. M., Romero L., et al., Parameters symptomatic for boron toxicity in leaves of tomato plants, J. Bot., 1-17, 2012.

[13] Pardossi A., Romani M., Carmassi G., Guidi L., Landi M., Incrocci L., Maggini R., et al., Boron accumulation and tolerance in sweet basil (*Ocimum basilicum L.*) with green or purple leaves, Plant Soil, 395, 375-389, 2015.

[14] Ardıc M., Sekmen A. H., Tokur S., Ozdemir F., Turkan I., Antioxidant response of chickpea plants subjected to boron toxicity, Plant Biol., 11, 328-338, 2009.

[15] Reid R. J., Identification of boron transporter genes likely to be responsible for tolerance to boron toxicity in wheat and barley, Plant Cell Physiol., 48, 1673-1678, 2007.

[16] Reid R. J., Fitzpatrick K. L., Redistribution of boron in leaves reduces boron toxicity, Plant Signaling Behav., 4 (11), 1091-1093, 2009.

[17] Schnurbusch T., Hayes J., Hrmova M., Baumann U., Ramesh S. A., Tyerman S. D., Langridge P., et al., Boron toxicity tolerance in barley through reduced expression of the multifunctional aquaporin *HvNIP2;1*, Plant Physiol., 153, 1706-1715, 2010.

[18] Landi M., Guidi L., Pardossi A., Tattini M., Gould, K. S., Photoprotection by foliar anthocyanins mitigates effects of boron toxicity in sweet basil (*Ocimum basilicum*), Planta, 240, 941-953, 2014.

[19] Öz M. T., Yilmaz R., Eyidoğan F., de Graaff L., Yücel M., Öktem H. A., Microarray analysis of late response to boron toxicity in barley (*Hordeum vulgare* L.) leaves, Turk. J. Agric. For., 33, 191-202, 2009.

[20] Kayihan C., Öz M. T., Eyidogan F., Yucel M., Öktem H. A., Physiological, biochemical, and transcriptomic responses to boron toxicity in leaf and root tissues of contrasting wheat cultivars, Plant Mol. Biol. Rep., 35, 97-109, 2017.

[21] Zhang B., MicroRNA: a new target for improving plant tolerance to abiotic stress, J. Exp. Bot., 66, 1749-1761, 2015.

[22] Ma X., Cao X., Mo B., Chen X., Trip to ER: MicroRNA-mediated translational repression in plants, RNA Biol., 10, 1586-1592, 2013.

[23] Jones-Rhoades M. W., Bartel D. P., Bartel B., MicroRNAs and their regulatory roles in plants, Annu. Rev. Plant Biol., 57, 19-53, 2006.

[24] Kraft E., Stone S. L., Ma L., Su N., Gao Y., Lau O. S., Deng X. W., et al., Genome analysis and functional characterization of the E2 and RING-type E3 ligase ubiquitination enzymes of Arabidopsis, Plant Physiol., 139, 1597-1611, 2005.

[25] Liang G., Yang F., Yu D., MicroRNA395 mediates regulation of sulfate accumulation and allocation in *Arabidopsis thaliana*, Plant J., 62 (6), 1046-1057, 2010.

[26] Lu Y. B., Yang L. T., Qi Y. P., Li Y., Li Z., Chen Y. B., Huang Z. R., et al., Identification of boron-deficiency-responsive microRNAs in *Citrus sinensis* roots by illumina sequencing, BMC Plant Biol., 14, 123, 2014.

[27] Huang J. H., Qi Y. P., Wen S. X., Guo P., Chen X. M., Chen L. S., Illumina microRNA profiles reveal the involvement of miR397a in Citrus adaptation to long-term boron toxicity via modulating secondary cell-wall biosynthesis, Sci. Rep., 6, 22900, 2016.

[28] Kramer M. F., Stem-loop RT-qPCR for miRNAs, Curr. Protoc. Mol. Biol., 95 (1), 5-10, 2011.

[29] Gautam V., Singh A., Singh S., Sarkar A. K., An efficient LCM based method for tissue specific expression analysis of genes and miRNAs, Sci. Rep., 6, 21577, 2016.

[30] Balcells I., Cirera S., Busk P. K., Specific and sensitive quantitative RT-PCR of miRNAs with DNA primers, BMC Biotech., 11, 70, 2011.

[31] Murashige T., Skoog F., A revised medium for rapid growth and bio assays with tobacco tissue cultures, Physiol. Plant., 15, 473-497, 1962.

[32] Varkonyi-Gasic E., Wu R., Wood M., Walton E. F., Hellens R. P., Protocol: a highly sensitive RT-PCR method for detection and quantification of microRNAs, Plant Methods, 3, 12, 2007.

[33] Kayıhan D. S., Kayıhan C., Çiftçi Y. Ö., Excess boron responsive regulations of antioxidative mechanism at physio-biochemical and molecular levels in *Arabidopsis thaliana*, Plant Physiol. Biochem., 109, 337-345, 2016.

[34] Kozomara A., Birgaoanu M., Griffiths-Jones S., miRBase: from microRNA sequences to function, Nucleic Acids Res., 47 (D1), D155-D162, 2019.

[35] Dai X., Zhuang Z., Zhao P. X., psRNATarget: a plant small RNA target analysis server (2017 release), Nucleic Acids Res., 46 (W1), W49-W54, 2018.

[36] Mi H., Muruganujan A., Ebert D., Huang X., Thomas P. D., PANTHER version 14: more genomes, a new PANTHER GO-slim and improvements in enrichment analysis tools, Nucleic Acids Res., 47 (D1), D419-D426, 2019.

[37] Llave C., Xie Z., Kasschau K. D., Carrington J. C., Cleavage of Scarecrow-like mRNA targets directed by a class of Arabidopsis miRNA, Science, 297 (5589), 2053-2056, 2002.

[38] Bartel D., MicroRNAs: genomics, biogenesis, mechanism, and function, Cell, 116 (2), 281-297, 2004.

[39] Jones-Rhoades M. W., Bartel D. P., Computational identification of plant microRNAs and their targets, including a stress induced miRNA, Mol. Cell, 14 (6), 787-799, 2004.

[40] Zhang B. H., Pan X. P., Wang Q. L., Cobb G. P., Anderson T. A., Identification and characterization of new plant microRNAs using EST analysis, Cell Res., 15, 336-360, 2005.

[41] Hsieh L. C., Lin S. I., Shih A. C. C., Chen J. W., Lin W. Y., Tseng C. Y., Li W. H., et al., Uncovering small RNA-mediated responses to phosphate deficiency in *Arabidopsis* by deep sequencing, Plant Physiol., 151, 2120-2132, 2009.

[42] Wu J., Zhang Y., Zhang H., Huang H., Folta K. M., Lu J., Whole genome wide expression profiles of *Vitis amurensis* grape responding to downy mildew by using Solexa sequencing technology, BMC Plant Biol, 10, 234, 2010.

[43] Ozhuner E., Eldem V., Ipek A., Okay S., Sakcali S., Zhang B., Boke H., et al., Boron stress responsive microRNAs and their targets in barley, PLoS ONE, 8 (3), e59543, 2013.

[44] Huang J. H., Qi Y. P., Wen S. X., Guo P., Chen X. M., Chen L. S., Illumina microRNA profiles reveal the involvement of miR397a in citrus adaptation to long-term boron toxicity via modulating secondary cell-wall biosynthesis, Sci. Rep., 6, 22900, 2016.

[45] Kayihan D. S., Kayihan C., Çiftçi Y. O., Moderate level of toxic boron causes diferential regulation of microRNAs related to jasmonate and ethylene metabolisms in *Arabidopsis thaliana*, Turk. J. Bot., 43, 167-172, 2019.

[46] Kepinski S., Leyser O., The Arabidopsis F-box protein TIR1 is an auxin receptor, Nature, 435 (7041), 446-451, 2005.

[47] Dharmasiri N., Dharmasiri S., Estelle M., The F-box protein TIR1 is an auxin receptor, Nature, 435 (7041), 441-445, 2005.

[48] Dharmasiri N., Dharmasiri S., Weijers D., Lechner E., Yamada M., Hobbie L., Ehrismann J. S., et al., Plant development is regulated by a family of auxin receptor F box proteins, Dev. Cell, 9 (1), 109-119, 2005.

[49] Vidal E. A., Araus V., Lu C., Parry G., Green P. J., Coruzzi G. M., Gutierrez R. A., Nitrate-responsive miR393/AFB3 regulatory modüle controls root system architecture in *Arabidopsis thaliana*, Proc. Natl. Acad. Sci. USA, 107 (9), 4477-4482, 2010.

[50] Si-Ammour A., Windels D., Arn-Bouldoires E., Kutter C., Ailhas J., Meins F., Vazquez F., miR393 and secondary siRNAs regulate expression of the TIR1/AFB2 auxin receptor clade and auxin-related development of *Arabidopsis* leaves, Plant Physiol., 157, 683-691, 2011.

[51] Chen Z. H., Bao M. L., Sun Y. Z., Yang Y. J., Xu X. H., Wang J. H., Han N., et al., Regulation of auxin response by miR393-targeted transport inhibitör response protein 1 is involved in normal development in Arabidopsis, Plant Mol. Biol., 77 (6), 619-629, 2011.

[52] Windels D., Bielewicz D., Ebneter M., Jarmolowski A., Szweykowska-Kulinska Z., Vazquez F., miR393 is required for production of proper auxin signalling outputs, PLoS One, 9, e95972, 2014.

[53] Sunkar R., Zhu J. K., Novel and stress-regulated microRNAs and other small RNAs from Arabidopsis, Plant Cell, 16, 2001-2019, 2004.

[54] Navarro L., Dunoyer P., Jay F., Arnold B., Dharmasiri N., Estelle M., Voinnet O., et al., A plant miRNA contributes to antibacterial resistance by repressing auxin signaling, Science, 312, 436–439, 2006.

[55] Gao P., Bai X., Yang L., Lv D., Pan X., Li Y., Cai H., et al., osa-MIR393: a salinity- and alkaline stress-related microRNA gene, Mol. Biol. Rep., 38, 237-242, 2011.

[56] Bian H., Xie Y., Guo F., Han N., Ma S., Zeng Z., Wang J., et al., Distinctive expression patterns and roles of the miRNA393/TIR1 homolog modüle in regulating flag leaf inclination and primary and crown root growth in rice (*Oryza sativa*), New Phytol., 196, 149-161, 2012.

[57] Xia K., Wang R., Ou X., Fang Z., Tian C., Duan J., Wang Y., et al., *OsTIR1* and *OsAFB2* downregulation via *OsmiR393* overexpression leads to more tillers, early flowering and less tolerance to salt and drought in rice, PLoS One, 7, e30039, 2012.

[58] Zhao B., Liang R., Ge L., Li W., Xiao H., Lin H., Ruan K., et al., Identification of drought-induced microRNAs in rice, Biochem. Biophys. Res. Commun., 354, 585-590, 2007.

[59] Ferreira T. H., Gentile A., Vilela R. D., Costa G. G., Dias L. I., Endres L., Menossi M., microRNAs associated with drought response in the bioenergy crop sugarcane (*Saccharum spp.*), PLoS One, 7, e46703, 2012.

[60] Dharmasiri S., Estelle M., The role of regulated protein degradation in auxin response, Plant Mol. Biol., 49, 401-409, 2002.

[61] Long R., Li M., Li X., Gao Y., Zhang T., Sun Y., Kang J., et al., A novel miRNA sponge form efficiently inhibits the activity of miR393 and enhances the salt tolerance and ABA insensitivity in *Arabidopsis thaliana*, Plant Mol. Biol. Rep., 35, 409-415, 2017.

BOR DERGİSİ
JOURNAL OF BORON
https://dergipark.org.tr/boron

Enhancing the mechanical features of poly(vinyl alcohol) nanofibers with the addition of boron nitride

Hazal Gergeroğlu[1*], Neslihan Sakar[2], Hamed Ghorbanpoor[3], Çağlar Özer[4]

[1]Dokuz Eylul University, Department of Nanoscience and Nanoengineering, 35340, Izmir, Turkey,
ORCID ID orcid.org/0000-0001-8369-9221
[2]Dokuz Eylul University, Department of Nanoscience and Nanoengineering, 35340, Izmir, Turkey,
ORCID ID orcid.org/0000-0002-9541-194X
[3]Ankara Yildirim Beyazit University, Department of Biomedical Engineering, 06010, Ankara, Turkey,
ORCID ID orcid.org/ 0000-0002-2665-8172
[4]Dokuz Eylul University, Department of Nanoscience and Nanoengineering, 35340, Izmir, Turkey,
ORCID ID orcid.org/ 0000-0002-8127-741X

ARTICLE INFO

Article history:
Received February 28, 2020
Accepted November 17, 2020
Available online December 29, 2020

Research Article

DOI: 10.30728/boron.696373

Keywords:
Body armor,
Boron nitride,
Composite nanofibers,
Electrospinning,
Nanoindentation.

ABSTRACT

Improvement of nano-sized products with boron additives with remarkable properties has become a popular trend for many different application areas. Here, we have reported an efficient poly(vinyl alcohol) (PVA) based composite nanofiber which was functionalized with the hexagonal boron nitride (h-BN) via electrospinning technique, for the first time as far as known, for body-armor and protective clothing applications. PVA-based composite nanofibers containing h-BN with a diameter of approximately 326 nm have shown significant mechanical features compared to pure PVA nanofibers with a diameter of about 223 nm. Mechanical features were investigated by nanoindentation and the results of nanoindentation demonstrated that the elastic modulus of PVA nanofibers increased by 77%, and hardness values of polymeric nanofibers reached ten times more, by the addition of h-BN. FTIR and XRD characterizations approved that there is no chemical change of h-BN when it was integrated into the PVA based composite nanofibers. We exceptionally believe that the achieved results offer a potential lightness and cost-effective strategy for body armor and protective clothing applications in contrast to boron carbide-based body armor products, which have main problems such as weightiness and high-priced.

1. Introduction

Recently, the focus has been on the development of boron-based high-tech products, and the expansion of boron-based materials and additives [1-4]. In this sense, when advanced boron compounds are examined, nowadays boron nitride (BN), which offers a wide range of application potential and has outstanding properties, is remarkable [4,5]. Structurally like the carbon system, BNs are synthetic materials that, although discovered in the19th century, did not develop into a commercial material until the 20th century. It is mostly found in hexagonal (h-BN), cubic (c-BN), and amorphous structures [5,6]. h-BN has many different applications in engineering and refractory fields such as catalysis, contaminant removal in very harsh environments, and hydrogen storage due to its extraordinary features such as high resistance to acidic chemical corrosion, non-toxic, refractory features in vacuum up to 2000°C, lightweight, workability, high electrical resistance, and good thermal conductivity [4,6,7]. On the other hand, the nanostructure chemical composition refers to the order of atoms (atomic structure) and the dimension of a solid in one, two, or three. Thus, nanostructures have chemical and physical features that are characteristic of neither atomic nor mass equivalents [8]. Therefore, different studies have been realized for the production and characterization of h-BN in its forms such as nanotubes [9-11], fullerenes [12], nano-cones [13], nano-capsules [14,15], and nanoparticles [16,17] and the superior features of h-BN and the advantages of nanotechnology have been tried to be combined. Recently, limited studies have been published on the BN using PVA as a matrix. For example, Wang et al (2019) investigated the mechanical features and microstructures of PVA nanocomposites reinforced with boron nitride nanotubes (BNNTs). The authors claimed that BNNTs have excellent potential to design composite nanofillers in many applications [18]. Li et al. (2018) reported that, compared with pure PVA hydrogel, the thermal stability, mechanical features, and swelling behavior of BN

---

*Corresponding author: hazal.gergeroglu@ogr.deu.edu.tr nanosphere/PVA composite hydrogel are effectively enhanced [19]. Zhang et al. (2017) reported that BN-modified PVA aerogels can be successfully produced via the cheap frozen-drying method to use in environmental remediation applications [20]. Additionally, Zhang et al. (2018) showed that cellulose nanocrystals and boron nitride nanosheets enhanced the thermal conductivity, and the mechanical features of the PVA [21].

Among the reported h-BN nanostructures, the one-dimensional shape (1D) of h-BN (ie nanotubes, nanofibers) offers high performance in potential electronic and mechanical devices due to its axial ratio. Since the axial ratio plays a crucial role in the physical and chemical features of the 1D structures, it is desirable to being long in the nanostructures. Compared to other nanostructures, the longest axial ratio is found in nanofibers [7]. Therefore, many researchers have tried to produce h-BN nanofibers using complex procedures. The reported chemical synthesis methods are complex, it is very difficult to control the final product to be in the 1D form [7,8]. However, the electrospinning technique is renowned for its easy control of the size of the final product [22-24]. In this method, an electric field is used to produce fibers from polymers, composites, and ceramics to ultra-fine micro and nano scales, and nanofibers are produced efficiently [25]. Therefore, especially in the last decade, there are many studies investigating the production of h-BN nanofiber structures via the electrospinning technique, characterization of these structures, and indicating their potential in various application areas. For instance, multifunctional h-BN nanosheet/ poly(vinyl alcohol) (PVA) nanofiber membranes for use in electronic packaging and water treatment applications [26]; h-BN/poly (p-caprolactone) (PCL) composite nanofibers [27], and h-BN nanofibers [28] for aerospace and high-temperature filtration applications; h-BN/polyacrylonitrile (PAN) composite nanofibers [29] and h-BN/carbon composite nanofibers [30] as high-security low-cost electrolyte and electrode material for lithium-ion batteries applications; PCL, to use in bone-tissue engineering applications tricalcium phosphate (TCP) and h-BN composite nanofibers [31]; high-activity h-BN/titanium dioxide (TiO_2) composite nanofibers [32] as photocatalyst for use in photocatalytic applications have been significant investigation topics. Additionally, it has been stated that the h-BN/polymer composite nanofibers have a significant potential for body armor and protective clothing applications [33].

Body armor and protective clothing are very effective in defense and military forces, especially in reducing soldiers and police injuries and deaths. In today's technology, the armors and protective clothing have designed via considering the futuristic material options. However, academic and industrial studies have focused on reducing the weight of body armor systems and improve the comfort level. Additionally, considering the pricing of standard body armor systems up to several thousand dollars per set, cost reduction is an important factor in the studies. It has been reported that new materials, innovative designs, and lightweight systems that can meet these requirements need to be developed [34]. Although boron carbide is generally one of the strongest candidates for body armor applications, research continues to address basic problems such as cost and lightness [35-37]. Moreover, it is stated that protective clothing and body armors produced via electrospun nanofibers which have multifunctional features such as extremely lightness, cheap producibility, high breathable, and high elasticity can overcome these problems [38].

In this study, h-BN, known to have superior properties mentioned before, has played a role in improving mechanical properties. h-BN was combined then with PVA, which is widely used in body armor applications and the protective clothing industry, via the electrospinning method. Thus, coming together of the superior properties of h-BN with the advantages of nano-size was carried out. Moreover, the effect of adding h-BN on the mechanical features of PVA nanofibers is reported for the first time in the literature. The mechanical analysis was performed via the nano-indentation. Furthermore, resulted composite functionalized nanofibers were investigated for morphology, chemical interactions, and functional groups by performing SEM, XRD, and FTIR characterization.

2. Materials and methods

Poly(vinyl alcohol) (PVA, purity 95,40%) with molecular weight (MW) of (44.0526)n g/mol and 87.16% of hydroxyl groups was obtained from Zag Chemistry. Boron Nitride (BN, purity>99%, particle size 1 µm) was received from Sigma Aldrich. BN and PVA precursors were employed without any further treatment. The solvent was distilled water.

To prepare electrospinning solutions, firstly, an aqueous solution 8% by weight of (wt) of PVA was stirred at room temperature for 24 h. Then, h-BN (8% wt) was dissolved in distilled water at 95°C for 6 h. Aqueous h-BN solution added into pure PVA solution at 60°C via dropping technique and stirred for 2 h. Thus, PVA (pure), and PVA containing h-BN (PVA/BN) electrospinning solutions were prepared. The electrospinning process was performed using a commonly used simple electrospinning apparatus to obtain nanofibers. Nanofibers were obtained from the prepared solutions with the same electrospinning process parameters are applied as flow rate 1 mL/h, collector-syringe distance 20 cm, applied voltage 25 kV.

The morphological characterization of PVA (pure) and PVA/BN nanofibers was carried out by Philips XL 30S FEG scanning electron microscope (SEM) operat-

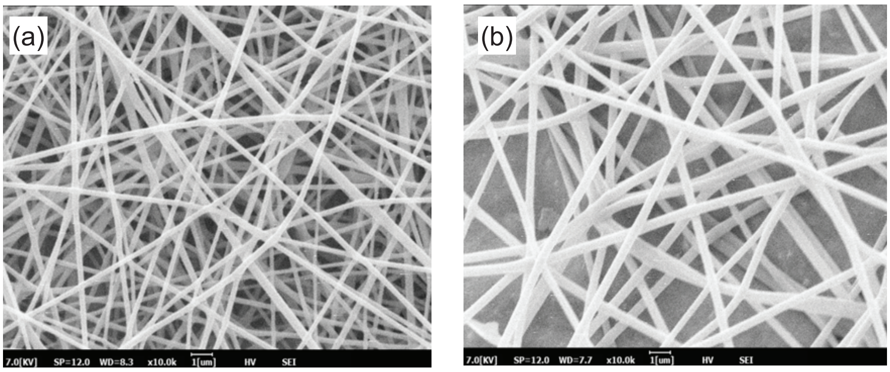

Figure 1. SEM photographs of (a) PVA (pure), (b) PVA/BN nanofibers.

ing at 7 kV voltage. From the SEM images obtained, the average fiber diameter was measured and calculated from 50 different locations using the Image J program. The phase identification and crystal structures of the obtained nanofibers were performed by Thermo Scientific ARL X-ray diffractometer (XRD) with Cu-Kα model (1.5405 Å) operating at 45 kV voltage and 44 mA current values. XRD data were recorded in the range of $10° \leq 2\theta \leq 80°$ in 0.02° steps at a rate of 2°/min. Fourier transform infrared spectroscopy (FTIR) studies were performed using (Thermoscientific Nicolet I10) device, with the wavenumber range of 4,000-500 cm^{-1}, to evaluate whether or not h-BN is integrated into the PVA structure without any chemical changes. Mechanical analysis of nanofibers was performed with IBIS DME Tools DS 95-50. The diamond conical surface with a half-tip angle of 70.3° was used to model the commonly used Berkovich indenter. Also, the thicknesses of PVA (pure) and PVA/BN nanofibers were several micrometers. 1 millinewton (mN) force was applied to five different locations for both samples and the penetration depth (μm) was measured. Nanoindentation load-penetration depth curves were obtained, and elastic modulus (E) and hardness values were calculated.

3. Results and discussion

The morphological structure and average fiber diameter were investigated by SEM. Figure 1 indicates that the average nanofiber diameter increases with the addition of BN. The average fiber diameter, which is measured at 50 different locations using the Image J program, is 223±50 nm for PVA (Figure 1a) and 326±72 nm for PVA/BN (Figure 1b). Although no change was made in the electrospinning process parameters, the diameter and standard deviation of the composite nanofibers increased by the addition of BN. The most important cause is probably integration of the BN into the fibers, and it is very significant evidence for the composite fibers which contain the h-BN.

BN is a chemically inactive ceramic material. Therefore, a chemical reaction between h-BN micron-size particles and PVA aqueous solution cannot be expected [16]. However, XRD analysis was performed to ensure that the h-BN micron particles used in this study were integrated into the PVA structure without any chemical reactions. Additionally, the effect of the electrospinning process was investigated by XRD characterization of initial PVA and BN used in nanofiber production. It has understood that the XRD pattern of the initial PVA indicates the amorphous structure whereas the PVA pure (pink graph) nanofibers produced via electrospinning shows the semi-crystalline structure (Figure 2) with two main peaks at around $2\theta \approx 14°$ and $2\theta \approx 17°$, respectively. Moreover, the initial h-BN pattern in Figure 2, indicates the typical peaks of h-BN with defined, intense peaks at $2\theta = 26.76°$ and $2\theta = 41.46°$ related to the (002) and (100) reflection (ICDD-PDF Card: 00-034-0421), respectively. The main peaks of the BN ceramics are visible in the XRD pattern of PVA/BN nanofibers, but not in the XRD pattern of PVA (pure) nanofibers. However, the fact that a specific peak in the diffraction pattern of PVA is also visible in the PVA/BN nanofiber pattern means that each component shows its own diffraction region. If there were any interactions, these peaks could be seen nested [39]. Therefore, it has been shown that BN is integrated into the PVA matrix without any chemical reaction.

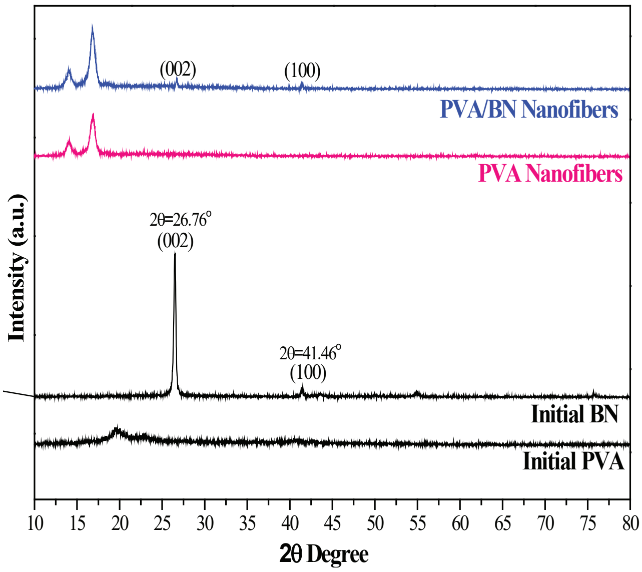

Figure 2. XRD patterns of the initial PVA, BN (Initial), PVA (pure), and PVA/BN nanofibers

As a result, it was considered in the XRD analysis that BN was not chemically affected by the electrospinning process. Although XRD is a highly reliable method of analysis for crystalline materials, the same may not apply to amorphous, semi-crystalline materials [16]. Due to the polymer used (PVA), FTIR characterizations were performed in addition to XRD studies. In the FTIR spectra (Figure 3a), the B-N bond represents two peaks of h-BN located at 767 and 1317 cm^{-1}, respectively, while the B-H bond corresponds to the two bands at 2331 and 2535 cm^{-1} [20]. Figure 3b shows that the main peaks of PVA (pure) nanofibers were observed at 845, 1093, 1260, 1434, 1734, 2930, and 3290 cm^{-1}. These peaks are appointed to the C-C stretching vibration, C-O stretching of acetyl groups, C-H deformation vibration, C-H bending vibration of CH_2, C=O carbonyl stretch, CH_2 asymmetric stretching vibration, and the O-H stretching vibration of the hydroxy group, accordingly [40]. For the PVA/BN nanofibers, similar peaks were observed (Figure 3c). The addition of BN is assigned to small shifts in the main peaks. Moreover, the FTIR spectra of PVA/BN confirms that the h-BN structure. In Figure 3 (blue curve), due to the B-N and BN-O bonds, which are attributed to the h-BN and B-OH bonds, respectively, peaks are observed at 804, 1088, 1374, and 3306 cm^{-1} [32,41]. Consequently, it has been demonstrated that BN has been successfully integrated without any chemical change in the structure of PVA.

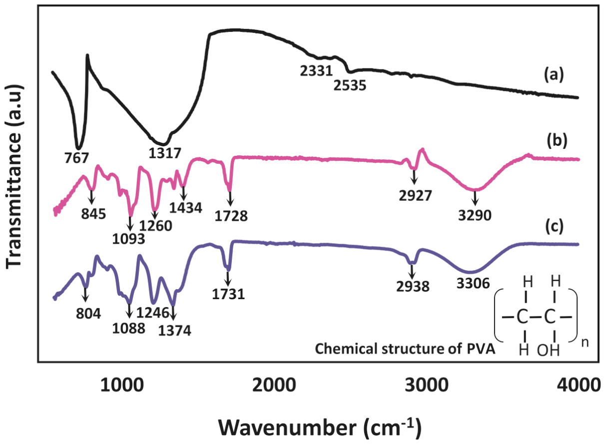

Figure 3. The FTIR spectra of (a) BN (Initial), (b) PVA (pure), (b) PVA/BN nanofibers.

To investigate the mechanical effect of BN integration into PVA nanofibers, nano-indentation tests were performed. For both samples (PVA and PVA/BN nanofibers), 1 mN of force was applied to five different locations and the penetration depth was measured. Thus, nanoindentation load- penetration depth curves were obtained (Figure 4). Comparing the load penetration depth curves of PVA (pure) nanofibers (Figure 4a) with the curves of PVA/BN nanofibers (Figure 4b), it is clear that PVA (pure) nanofibers have a deeper penetration depth to the surface under the same load. This means that the strength and hardness of PVA/BN nanofibers are higher than that of PVA (pure) nanofibers.

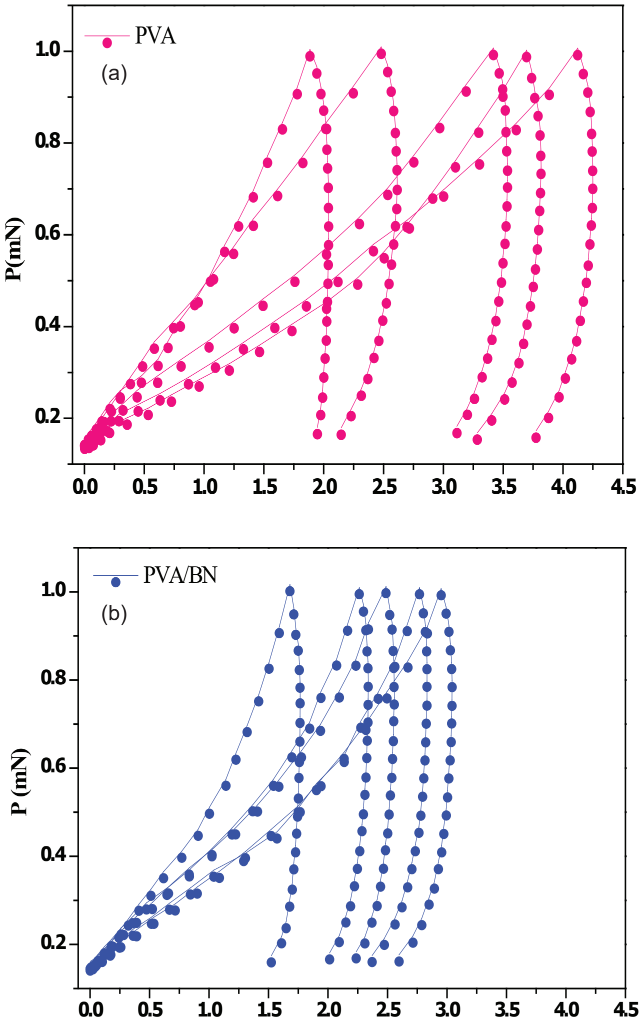

Figure 4. Nanoindentation load-penetration depth curves; (a) PVA (pink), (b) PVA/BN (blue) nanofibers.

To confirm the results obtained from the graphs, the elastic modulus (E) was calculated from the tilt of the first part of the unloading curve (S) (Figure 4) using Eq (1) and (2) [42,43].

$$S = 2\beta\sqrt{\frac{A}{\pi}}E_r \tag{1}$$

In (1), A is the projected area of the indentation, b is a constant dependent on the geometry of the indenter, and E_r is the reduced elastic modulus given by,

$$\frac{1}{E_r} = \frac{1-\nu^2}{E} + \frac{1-\nu_i^2}{E_i} \tag{2}$$

where ν and E are the Poisson's ratio and elastic modulus for the sample and ν_i and E_i are equal quantities for the indenter, respectively. On the other hand, in nanoindentation, hardness (H) is determined as the average contact pressure (P_{max}) and is acquired by dividing the peak force by the projected area (A) of the contact between the sample and tip using Eq(3) [44,45]. The values obtained from all calculations are shown in Table 1.

$$H = \frac{P_{max}}{A} \quad (3)$$

Results of calculations (Table 1) were confirmed the obtained nanoindentation load versus penetration depth curves (Figure 4). The existence of h-BN leads to increasing in E from 134 MPa to 238 MPa. Furthermore, the hardness values were calculated as 7.5 and 86.2 MPa for PVA and PVA/BN nanofibers, respectively (Table 1). Since the electrospinning process parameters for both of them were the same, the comparison indicates that the improvements in mechanical features were due to h-BN addition. Thus, it can be claimed that the critical enhancement in the elastic modulus and hardness of PVA nanofibers with the integration of h-BN is presumably due to as follows: (i) homogeneous distribution of h-BN additives in the PVA matrix via the electrospinning process, (ii) considerable increase in crystallinity of the PVA matrix, (iii) effective transfer of the load due to the intermolecular H-bond between the PVA matrix and h-BN, which is a powerful interaction that limits the chain mobility of the PVA.

Table 1. Results of nano-indentation.

Sample	Force (mN)	Elastic Modulus (MPa)	Indentation Hardness (MPa)
PVA	1	134	7.5
PVA/BN	1	238	86.2

Moreover, the increase in the elastic modulus and hardness values of PVA/BN composite nanofibers because of the existence of h-BN was similarly reported in PVA/BN nanocomposite films performed in previous studies [46-48]. For instance, Sreedhara et al., in 2018, with the addition of 0.2% wt h-BN sheets into PVA films, have reported that the elastic module and the hardness values increased from 4.3 GPa to 7.3 GPa, and from 76.7 MPa to 109.2 MPa, respectively [47]. In another study, it has been shown that the elastic modulus increased from 8.6 GPa to 12.9 GPa and the hardness value increased from 0.25 GPa to 0.6 GPa by the addition of two different sizes (0.5 and 1 μm) of BN nanoplate into PVA/tannic acid (TA) films [46]. However, according to our best knowledge, for the first time, the mechanical features of PVA/BN nanofibers and the mechanical effect of the existence of h-BN into the PVA nanofibers structure were investigated in this work. Furthermore, this study focused on the contribution of h-BN to improving the mechanical features of the PVA nanofibers with a uniform fiber morphology. Therefore, its use at the maximum possible concentration has been investigated. However, the concentration of additives that can be incorporated into the polymer in the electrospinning method is limited because when the optimum amount is exceeded, it makes production conditions difficult and bead structures may be formed in the fibers. In this case, the homogeneous fiber structure can be damaged. Also, the distribution of the particles inside the polymeric nanofibers is a significant parameter. Herein, the significant point is that particles tend to stand apart when a small amount of additive material was added, whereas when high amounts of additives are added, the particles tend to aggregate, in which case agglomeration occurs [8]. In light of this knowledge, the main purpose of this study is not only to obtain fibers with reinforced mechanical features but also to obtain a fiber morphology without bead structures. Therefore, the maximum amount of h-BN that we can use without damaging fiber morphology and obtain maximum improvement in mechanical features has been determined as 8% by weight.

4. Conclusion

h-BN is known to have superior properties such as non-toxic, lightweight, workability, high electrical resistance, and good thermal conductivity. It has been reported in previous studies that the addition of h-BN into the composite film form of PVA, which is widely used in textile and protective clothing applications, improves its mechanical properties [46,47,49,50]. In our study, unlike previous studies, the mechanical features of nanofiber morphology were examined; the elastic modulus and hardness of PVA (pure) nanofibers with the addition of h-BN increased from 134 MPa to 238 MPa and 7.5 MPa to 86.2 MPa, respectively. Moreover, the incorporation of h-BN into PVA nanofibers has been observed to develop a critical improvement in PVA nanofibers, similar to composite PVA/BN films. Thus, a substantial enhancement of the mechanical features can be attributed to the incorporation of h-BN into PVA nanofibers.

After adding the h-BN to the PVA matrix structure, the average diameter of electrospun composite nanofibers increased from approximately 223 nm to about 326 nm, increasing the diameter of the nanofibers probably due to integration of the h-BN into the fibers. Furthermore, this evidence is critically important in addition to FTIR analysis shows that the PVA/BN composite fibers contain the h-BN. Moreover, the h-BN was successfully incorporated into PVA nanofibers without any chemical change based on the FTIR and XRD results.

In this study, it has been shown that PVA/BN composite nanofibers offer high potential in body armor and protective clothing application areas with their lightness, cheapness, and high strength properties. Moreover, this work has suggested a novel approach for the building of cost-effective and light composite nanofiber-based structures that support body armor and protective clothing applications.

Acknowledgment

The authors appreciate to Center for Fabrication and Application of Electronic Materials Dokuz Eylul University, for which this study was carried out.

References

[1] Hey-Hawkins E., Teixidor C. V., Boron-based compounds: Potential and emerging applications in medicine, 1st edition, John Wiley&Sons Ltd., Sussex, UK, 2018.

[2] Venegas J. M., McDermott W. P., Hermans I., Serendipity in catalysis research: Boron-based materials for alkane oxidative dehydrogenation, Acc. Chem. Res., 51, 2556-2564, 2018.

[3] Jiang N., Li B., Ning F., Xia D., All boron-based 2D material as anode material in Li-ion batteries, J. Energy Chem., 27 (6), 1651-1654, 2018.

[4] Yu S., Wang X., Pang H., Zhang R., Song W., Fu D., Hayat T., et al., Boron nitride-based materials for the removal of pollutants from aqueous solutions: a review, Chem. Eng. J., 333, 343-360, 2018.

[5] Zheng Z., Cox M., Li B., Surface modification of hexagonal boron nitride nanomaterials: A review, J. Mater. Sci., 53 (1), 66-99, 2018.

[6] Bosak A., Serrano J., Krisch M., Watanabe K., Taniguchi T., Kanda H., Elasticity of hexagonal boron nitride: Inelastic x-ray scattering measurements, Phys. Rev. B: Condens. Matter, 73, 41402, 2006.

[7] Jiang S., Chen Y., Duan G., Mei C., Greiner, A., Agarwal, S., Electrospun nanofiber reinforced composites: a review, Polym. Chem., 9, 2685-2720, 2018.

[8] Hwang H. J., Barakat N. A. M., Kanjwal M. A., Sheikh F. A., Kim H. Y., Abadir M. F., Boron nitride nanofibers by the electrospinning technique, Macromol. Res., 18, 551-557, 2010.

[9] Ban C., Li L., Wei L., Electrical properties of O-self-doped boron-nitride nanotubes and the piezoelectric effects of their freestanding network film, RSC Adv., 8, 29141-29146, 2018.

[10] Mirhaji E., Afshar M., Rezvani S., Yoosefian M., Boron nitride nanotubes as a nanotransporter for anti-cancer docetaxel drug in water/ethanol solution, J. Mol. Liq., 271, 151-156, 2018.

[11] Jakubinek M. B., Ashrafi B., Martinez-Rubi Y., Guan J., Rahmat M., Kim K. S., Dénommée S., et al., Nanotube Superfiber Materials, Chap. 5: Boron Nitride Nanotube Composites and Applications, Elsevier Inc., Amsterdam, Hollanda, 2019.

[12] Esrafili M. D., Heydari S., Carbon-doped boron-nitride fullerenes as efficient metal-free catalysts for oxidation of SO_2: a DFT study, Struct. Chem., 29 (1), 275-283, 2018.

[13] Kvashnin D. G., Matveev A. T., Lebedev O. I., Yakobson B. I., Golberg D., Sorokin P. B., Shtansky D. V., Ultrasharp h-BN nanocones and the origin of their high mechanical stiffness and large dipole moment, J. Phys. Chem. Lett., 9 (17), 5086-5091, 2018.

[14] Oku T., Narita I., Tokoro H., Synthesis and magnetic property of boron nitride nanocapsules encaging iron and cobalt nanoparticles, J. Phys. Chem. Solids, 67 (5-6), 1152-1156, 2006.

[15] Oku T., Kuno M., Synthesis, argon/hydrogen storage and magnetic properties of boron nitride nanotubes and nanocapsules, Diam. Relat. Mater., 12 (3-7), 840-845, 2003.

[16] Türkez H., Arslan M. E., Sönmez E., Açıkyıldız M., Tatar A., Geyikoğlu F., Synthesis, characterization and cytotoxicity of boron nitride nanoparticles: emphasis on toxicogenomics, Cytotechnology, 71 (1), 351-361, 2019.

[17] Kıvanç M., Barutca B., Koparal A. T., Göncü Y., Bostancı S. H., Ay N., Effects of hexagonal boron nitride nanoparticles on antimicrobial and antibiofilm activities, cell viability, Mater. Sci. Eng., 91, 115-124, 2018.

[18] Wang W., Li Z., Prestat E., Hashimoto T., Guan J., Kim K. S., Kingston C. T., et al., Reinforcement of polymer-based nanocomposites by thermally conductive and electrically insulating boron nitride nanotubes, ACS Appl. Nano Mater., 3 (1), 364-374, 2019.

[19] Li R., Lin J., Fang Y., Yu C., Zhang J., Xue Y., Liu Z., et al., Porous boron nitride nanofibers/PVA hydrogels with improved mechanical property and thermal stability, Ceram. Int., 44 (18), 22439-22444, 2018.

[20] Zhang R., Wan W., Qiu L., Wang Y., Zhou Y., Preparation of hydrophobic polyvinyl alcohol aerogel via the surface modification of boron nitride for environmental remediation, Appl. Surf. Sci., 419, 342-347, 2017.

[21] Zhang J., Lei W., Chen J., Liu D., Tang B., Li J., Wang X., Enhancing the thermal and mechanical properties of polyvinyl alcohol (PVA) with boron nitride nanosheets and cellulose nanocrystals, Polymer, 148, 101-108, 2018.

[22] Avci H., Akkulak E., Gergeroglu H., Ghorbanpoor H., Uysal O., Sariboyaci A. E., Demir B., et al., Flexible poly(styrene-ethylene-butadiene-styrene) hybrid nanofibers for bioengineering and water filtration applications, J. Appl. Polym. Sci., 137 (26), 49184, 2020.

[23] Avci H., Gergeroglu H., Synergistic effects of plant extracts and polymers on structural and antibacterial properties for wound healing, Polym. Bull., 76, 3709-3731, 2019.

[24] Avci H., Ghorbanpoor H., Nurbas M., Preparation of origanum minutiflorum oil-loaded core-shell structured chitosan nanofibers with tunable properties, Polym. Bull., 75, 4129-4144, 2018.

[25] Raghavan P., Lim D. H., Ahn J. H., Nah C., Sherrington D. C., Ryu H. S., Ahn H. J., Electrospun polymer nanofibers: The booming cutting edge technology, React. Funct. Polym., 72 (12), 915-930, 2012.

[26] Yin C. G., Ma Y., Liu Z. J., Fan J. C., Shi P. H., Xu Q. J., Min Y. L., Multifunctional boron nitride nanosheet/polymer composite nanofiber membranes, Polymer, 162, 100-107, 2019.

[27] Cakmak Y., Canbolat M. F., Cakmak E., Dayik M., Production and characterization of boron nitride-doped nanofiber mats created through electrospinning, J. Ind. Text., 47 (6), 993-1005, 2018.

[28] Liu Z., Zhao K., Luo J., Tang Y., Electrospinning of boron nitride nanofibers with high temperature stability, Scr. Mater., 170, 116-119, 2019.

[29] Aydın H., Çelik S. Ü., Bozkurt A., Electrolyte loaded hexagonal boron nitride/polyacrylonitrile nanofibers for lithium ion battery application, Solid State Ionics, 309, 71-76, 2017.

[30] Chen M., Zhang S., Zhang J., Chen Q., Electrospun carbon nanofiber/boron nitride composites as flexible anodes for lithium-ion batteries, J. Nanosci. Nanotechnol., 19, 220-225, 2019.

[31] Ozbek B., Erdogan B., Ekren N., Oktar F. N., Akyol, S., Ben-Nissan, B., Sasmazel, H. T., et al., Production of the novel fibrous structure of poly(ε-caprolactone)/tri-calcium phosphate/hexagonal boron nitride composites for bone tissue engineering, J. Aust. Ceram. Soc., 54, 251-260, 2018.

[32] Nasr M., Viter R., Eid C., Habchi R., Miele P., Bechelany M., Enhanced photocatalytic performance of novel electrospun BN/TiO_2 composite nanofibers, New J. Chem., 41, 81-89, 2017.

[33] Economy J., Anderson R. V., Properties and uses of boron nitride fibers, Text. Res. J., 36 (11), 994-1003, 1966.

[34] Crouch I. G., Body armour–New materials, new systems, Def. Technol., 15 (3), 241-253, 2019.

[35] Lakov L., Shunqi Z., St, A., Study of the effectiveness of corundum and boron carbide ceramics in hybrid protection systems, Secur. Futur., 3, 63-65, 2019.

[36] Cegła M., Habaj W., Podgórzak P., Development of lightweight bulletproof vest inserts with increased protection capability, Problemy Mechatroniki: uzbrojenie, lotnictwo, inżynieria bezpieczeństwa, 5, 23-34, 2014.

[37] Agrawal B. J., High performance textiles for ballistic protection, Defense Science Research Conference and Expo (DSR), IEEE, Singapore- Republic of Singapore, 1-4, August 3-5, 2011.

[38] Gorji M., Bagherzadeh R., Fashandi H., Electrospun Nanofibers, Chap. 21: Electrospun Nanofibers in Protective Clothing, Elsevier Inc., Londra, UK, 2016.

[39] Jia Y. T., Gong J., Gu X. H., Kim H. Y., Dong J., Shen X. Y., Fabrication and characterization of poly (vinyl alcohol)/chitosan blend nanofibers produced by electrospinning method, Carbohydr. Polym., 67 (3), 403-409, 2007.

[40] Kharazmi A., Faraji N., Hussin R. M., Saion E., Yunus W. M. M., Behzad K., Structural, optical, opto-thermal and thermal properties of ZnS-PVA nanofluids synthesized through a radiolytic approach, Beilstein J. Nanotechnol., 6, 529-536, 2015.

[41] Singh B., Kaur G., Singh P., Singh K., Kumar B., Vij A., Kumar M., et al., Nanostructured boron nitride with high water dispersibility for boron neutron capture therapy, Sci. Rep., 6, 35535, 2016.

[42] Oliver W. C., Pharr G. M., An improved technique for determining hardness and elastic modulus using load and displacement sensing indentation experiments, J. Mater. Res., 7, 1564-1583, 1992.

[43] Tan E. P. S., Lim C. T., Mechanical characterization of nanofibers-a review, Compos. Sci. Technol., 66, 1102-1111, 2006.

[44] Hussainova I., Hamed E., Jasiuk I., Nanoindentation testing and modeling of chromium-carbide-based composites, Mech. Compos. Mater., 46, 667-678, 2011.

[45] Wimmer R., Lucas B. N., Oliver W. C., Tsui T. Y., Longitudinal hardness and Young's modulus of spruce tracheid secondary walls using nanoindentation technique, Wood Sci. Technol., 31, 131-141, 1997.

[46] Qi X., Yang L., Zhu J., Hou Y., Yang M., Stiffer but more healable exponential layered assemblies with boron nitride nanoplatelets, ACS Nano, 10, 9434-9445, 2016.

[47] Sreedhara M. B., Barua M., Chaturvedi A., Rao C. N. R., Ramamurty U., Borocarbonitride,$(BN)_X(C)_{1-X}$, nanosheet-reinforced polymer nanocomposites for high mechanical performance, Carbon, 140, 688-695, 2018.

[48] Duan Z. Q., Liu Y. T., Xie X. M., Ye X. Y., A simple and green route to transparent boron nitride/PVA nanocomposites with significantly improved mechanical and thermal properties, Chin. Chem. Lett., 24, 17-19, 2013.

[49] Dai L., Long Z., Ren X., Deng H., He H., Liu W., Electrospun polyvinyl alcohol/waterborne polyurethane composite nanofibers involving cellulose nanofibers, J. Appl. Polym. Sci., 131, 2014.

[50] Ma P., Wang X., Xu W., Cao G., Application of corona discharge on desizing of polyvinyl alcohol on cotton fabrics, J. Appl. Polym. Sci., 114, 2887-2892, 2009.

boren

BOR DERGİSİ

JOURNAL OF BORON

https://dergipark.org.tr/boron

Boron doped hydroxyapatites in biomedical applications

İdil Uysal[1], Bengi Yılmaz[2], Zafer Evis[1,3*]

[1]Middle East Technical University, Department of Biomedical Engineering, 06800, Ankara, Turkey,
ORCID ID orcid.org/0000-0002-9687-8787
[2]University of Health Sciences Turkey, Department of Biomaterials, 34668, Istanbul, Turkey,
ORCID ID orcid.org/0000-0001-7642-4684
[3]Middle East Technical University, Department of Engineering Sciences, 06800, Ankara, Turkey,
ORCID ID orcid.org/0000-0002-7518-8162

ARTICLE INFO

Article history:
Received May 9, 2020
Accepted October 30, 2020
Available online December 29, 2020

Review Article

DOI: 10.30728/boron.734804

Keywords:
Bone tissue engineering,
Boron,
Hydroxyapatite,
Ion-doping,
Morphology.

ABSTRACT

Hydroxyapatite has been widely used in biomedical applications as a coating material for implant surfaces, a drug carrier, a scaffold or composite for bone tissue engineering applications. The highly ionic structure of hydroxyapatite allows doping of various ions, resulting in an improvement in its properties. Boron is one of the elements which can be doped into hydroxyapatite structure by replacing phosphate (PO_4^{3-}) or hydroxyl (OH^-) sites to obtain scaffolds for bone tissue engineering applications or a coating material for metal substrates. Although the effects of supplemental boron on bone, liver, and brain metabolism have been shown to have important results as a nutrient, there are very few studies in the literature on the use of boron-doped hydroxyapatite in the biomedical field. In this review, the details of synthesis methods and functional groups of boron-doped hydroxyapatite were tabulated. Generally, the addition of boron leads to the formation of rod-like morphology, while the density and Vicker's microhardness of hydroxyapatite decrease. Thermal stability and electrical insulation properties were observed to improve with boron doping. Boron was also shown to increase biodegradability, bioactivity as well as cell proliferation and differentiation of different cell types on the surface of hydroxyapatite.

1. Introduction

Hydroxyapatite (HA,$Ca_{10}(PO_4)_6(OH)_2$), has been widely studied as a biomaterial in hard tissue applications. The structural, mechanical, biological, thermal, and electrical properties of HA can be tuned by doping different ions. HA was previously doped with various single elements, such as strontium [1], selenium [2], silicon [3], magnesium [4], silver [5]; also with binary elements, such as zinc and fluoride [6], yttrium and fluoride [7], iron and selenium [8], zinc and silver [9]; and also with ternary dopants, such as magnesium, strontium, and zinc [10].

Boron is a member of the 3rd periodic group and it is a non-metal element. According to current estimates, 73.4% of the world's boron reserves are located in Turkey [11]. It is becoming increasingly important as an additive in polymer and ceramic composites to provide high strength, lightweight, and thermal stability. Moreover, boron is widely used as a dopant in bioactive glasses not only due to its ability to form a glass network but also its crucial role in biological functions. It was previously shown to increase the rate of degradation and release of Si from a bioactive glass which facilitates HA precipitation in the simulated body fluid (SBF) [12]. Although it is widely used in the composite and glass industry, there is a limited number of studies that focus on the synthesis and characterization of boron-doped HA (borohydroxyapatite). The applications of boron-doped HA in literature are mostly limited to being a component of bone tissue engineering scaffolds and having a supportive function in phosphors for fluorescent lamps. Boron is normally present as boric acid and borate ions [13] in geothermal water and there are many studies that utilize HA for the removal of boron from geothermal and wastewater [11,14]. Moreover, boric acid is used as a neutron absorbent in nuclear reactors. Since the removal of boric acid, which is a neuron absorbent used in nuclear power plant accidents, is of great importance, a method based on precipitation in the form of HA by addition of $Ca(OH)_2$ was studied [15]. The methods used for the synthesis of boron-doped HA were solid-state reaction, sol-gel, and wet precipitation methods based on acid-base reactions in general. Microwave-assisted biomimetic methods were also used to obtain boron-doped HA.

The research profile of boron doped hydroxyapatite was analysed. The analysis was done by search engine of "Web of Science" with keywords "boron",

---

*Corresponding author: evis@metu.edu.tr

"doped", "containing" and "hydroxyapatite". According to the results; in last five years, the number of research articles increased with about 2.5 fold of the total number of research items published since 2001 (Figure 1).

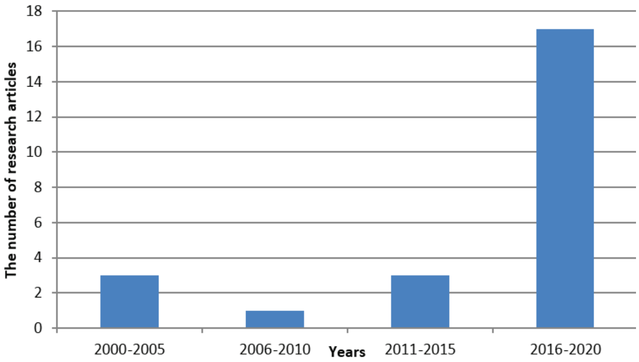

Figure 1. The number of research items published in periods consisted of five years.

The topics investigated were also analyzed. The results showed that new topics emerged such as mechanical properties and electrical properties in last five years. The weight of the research in biological properties did not differ much between the periods 2011-2015 and 2016-2020, whereas, the percentage of investigation related to structural properties decreased in last five years (Figure 2).

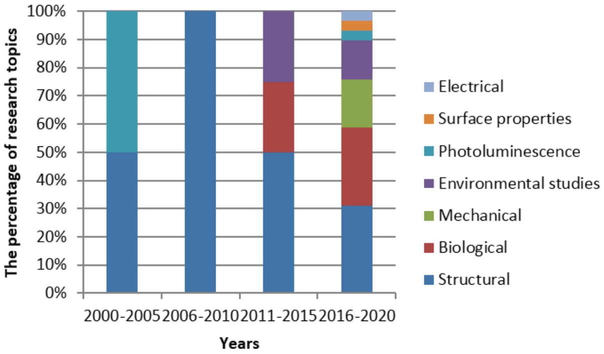

Figure 2. Percentage of research types based on periods consisted of five years.

In this review, the synthesis methods and the effects of boron doping into the structure of HA were evaluated based on studies published in the period from 2002 till now. The biological, mechanical, thermal, and electrical properties of HA affected by the addition of boron were summarized. Additionally, the influence on co-doping of boron with ions such as Sr^{2+}, Eu^{3+}, and Ce^{3+} was also reviewed.

2. The role of boron on biological functions

There are many pieces of evidence showing that boron can be a trace element for the human body [16]. The investigations related to the effects of boron on biological functions were mostly based on nutritional studies. The relationship between boron administration and biological responses in animals was widely documented [17]. The supplementary effect of boron on functions in brain and liver, bone metabolism, immune response, wound healing, and activities of hormones made boron a crucial element for metabolism [18].

Boron plays an important role in bone development, especially in terms of mineralization and bone growth. The studies related to osteogenesis revealed that boron has an important role in the mineralization function of osteoblasts by effecting related gene expressions and hormones such as 17β-estradiol (E2) and testosterone [18]. Moreover, the expression of mRNA, especially those encoding growth factors involved in angiogenesis and wound repair [19] is stimulated by boron. The affected proteins are not only bone-related proteins, such as bone morphogenic proteins (BMP-4, BMP-6, BMP-7), collagen type 1, osteopontin, bone sialoprotein, osteocalcin, but also wound healing enzymes such as elastase, collagenase, and alkaline phosphatase that are found in fibroblasts [20]. Boron induces absorption of magnesium which is an essential trace element and interacts with calcium and vitamin D, all of which play a role in bone metabolism [21].

Other functions of boron include increasing antioxidant enzymes, such as superoxide dismutase (SOD), catalase, and glutathione peroxidase, and decreasing the amount of inflammatory biomarkers. Furthermore, boron enhanced the formation and activity of essential biomolecules, such as nicotinamide adenine dinucleotide (NAD^+) [20].

3. Boron-doping in synthetic apatites

Boron is not one of the essential trace elements in bone [22]. However, as mentioned earlier, it has numerous functions in the regulation of bone metabolism. Therefore, researchers focused on synthesizing boron-doped HA and the investigation of its structural, mechanical, and biological properties as a candidate for biomedical applications.

The proposed formula of borohydroxyapatites is as follows:

$$Ca_{10}[(PO_4)_{6-x}(BO_3)_x][(BO_3)_y(BO_2)_z(OH)_{2-3y-z}] \quad (1)$$

There are three different sites of occupation in HA. These are (1) PO_4^{3-} site as triangular BO_3^{3-}, (2) OH^- site as triangular BO_3^{3-} which formed AB-type borohydroxyapatite and (3) OH^- site as two-fold coordinated linear BO_2^- (Figure 3) [23]. In a study aiming at removing boron in geothermal water with the use of HA, boron was reported to be located in OH^- site [11].

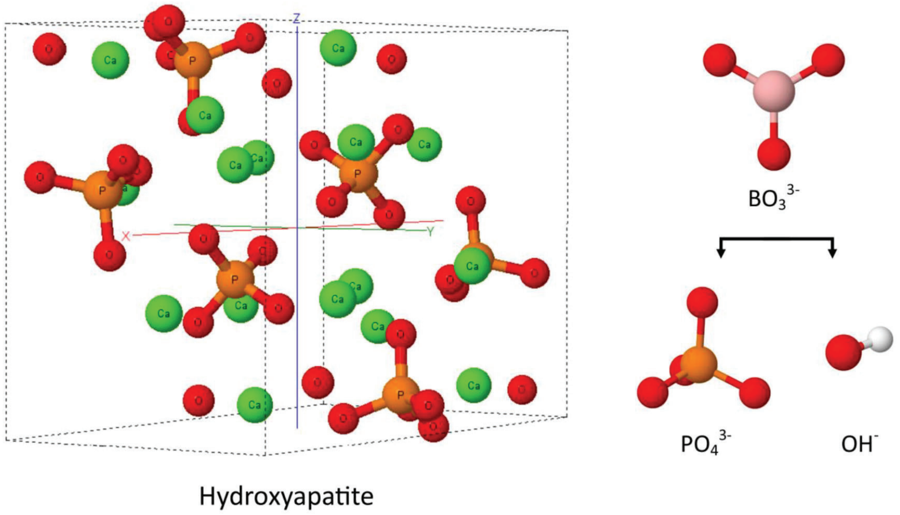

Figure 3. The lattice structure of hydroxyapatite with possible locations of BO_3^{3-}.

3.1. Synthesis and morphology of B doped HA

The synthesis methods of boron-doped HA were solid-state reaction, sol-gel, microwave-assisted biomimetic method, wet precipitation method, and acid-base method which was defined as a type of wet chemical synthesis method. Table 1 summarizes the production methods and boron amounts doped in HA structure.

Boron-doped HA with Ca/(P+B) molar ratio of 1.67 was previously synthesized by ultrasonic spray pyrolysis route for the incorporation of functional BO_2 groups [29]. BO_2^- ions were reported to replace OH^- ions and PO_4^{3-} ions were substituted with BO_3^{3-} after sintering. The dissociation of BO_2 groups into $B(OH)_3$, increased the amount of OH^- which resulted in the changes in surface properties, such as static contact angle of boron-doped HA.

Wet chemical precipitation method was also applied to synthesize boron-doped HA [30]. However, solid-state reaction was more effective in terms of the incorporation of boron ions when compared to wet chemical precipitation [24].

In addition to the precursors listed in Table 1, $Ca(OH)_2$ was used for the immobilization of borate with the aim of removing it from solutions [31]. The mechanism was explained in two stages which consisted of nucleation/crystallization in the presence of phosphate ions

Table 1. The synthesis methods and precursors for boron doped HA.

Method	**Precursors for production**			**Molar ratio Boron / Phosphate (B/P) (%)**	**Temperature and duration of heat treatment**
	Calcium	**Phosphate**	**Boron**		
Solid-state reaction [23],[24]	$CaCO_3$	$(NH_4)_2\ HPO_4$	H_3BO_3	3.4 5.3 9.1 13.2 15.4 20 50	1000°C / 24 h
Solid-state reaction [25]	$CaCO_3$	$Ca_2P_2O_7$	B_2O_3	9.1 18.2	1200°C / 6 h
Sol-gel [26]	$Ca(NO_3)_2.4H_2O$	$(NH_4)_2HPO_4$	H_3BO_3	1.7 3.3 5 6.7 8.3	800°C / 2 h
Sol-gel [27][a)]	$Ca(NO_3)_2{\cdot}4H_2O$	$(NH_4)_2HPO_4$	$B(OC_3H_7)_3$	26.7	1000°C / 2 h
Microwave-assisted biomimetic [28]	$CaCl_2{\cdot}2H_2O$	$NaH_2PO_4{\cdot}H_2O$	H_3BO_3	3.8 4.4 5 6.6 8.6 21	-
Wet precipitation [24]	$Ca(NO_3)_2{\cdot}4H_2O$	$(NH_4)_2HPO_4$	H_3BO_3	20	-

[a)] Approximate values are represented as % of B/P ratio and co-precipitation/co-sorption when there were no phosphate ions left in the system. In the nucleation/crystallization stage, the trigonal form of boron was preferable, whereas co-precipitation/co-sorption stage provided immobilization of boron in tetragonal form by co-sorption of $B(OH)_4^-$. Additional mechanism supported HA precipitation in nucleation/crystallization phase by dissociation of $(CaB(OH)_4)^+$ and $B(OH)_4^-$ ions as a result of decomposition of trigonal borate and $Ca(OH)_2$ complex. Maximum sorption density as denoted by B/Ca ratio was found to be 0.40 to keep single-phase HA. Above this ratio, amorphous CaB_2O_4 and HA were likely to form. It was also observed that when the borate species were captured in HA, the morphology changed from fibrous nano-sized rods to a more swollen structure.

For the samples synthesized by the biomimetic method, the size of the agglomerated spherical HA particles was previously reported to decrease from 50 nm to 30 nm with the addition of boron [28]. The HA nanoparticles exhibited a needle-like morphology while boron-doped HA had a rode-like form similar to biological apatite. However, in another study [15] where wet precipitation method was used to utilize boric acid as the boron source and $Ca(OH)_2$ as the calcium source, the particle size of boron-substituted HA was reported to increase approximately twofold in both dimensions with respect to HA without borate. The average length of the particles increased from 10 nm to nearly 20 nm and the width increased from 5 nm to 10 nm. Similarly, boron-doped samples synthesized by sol-gel method showed higher average particle size when compared to pure HA. Particle size increased from 537 nm to 1710 nm with the addition of boron [27].

3.2. Boron-doped HA as a coating material

Calcium phosphates, especially HA, are widely used in the coating of metallic biomaterials to combine their biocompatibility and bioactivity properties with the mechanical strength of metals. There are also numerous studies about various ion-doped HA coatings on metallic substrates, some examples are strontium-doped [1], selenium-doped [2], magnesium and silver co-doped [32], magnesium and fluoride co-doped [33] HA coatings on titanium or its alloys. However, the use of boron-incorporated HA as a coating material has been addressed in very few publications.

One study was reported that B_2O_3 doped HA was used as a coating material for Ti6Al4V substrate by applying high-velocity oxy fuel as the coating technique [34]. B_2O_3 doped HA was first synthesized by sol-gel method by using boron isopropoxide $[B(OC_3H_7)_3]$ as a precursor and the resulting B_2O_3 powder was mixed with HA during the HA production via sol-gel route, and then calcined before the coating process at 900°C for 2 hours. It was claimed that boron addition decreased deformation and delamination at the edges when compared to samples coated with pure HA. When the amount of boron increased from 1 wt.% to 3 wt.%, the scratch resistance of the coating also increased. Another important parameter for surface properties for biomedical applications is the contact angle due to cell to surface interaction. B_2O_3 addition decreased contact angle from 106.5 to 37.6 degrees when 3 wt.% B_2O_3 was added and the surface became highly hydrophilic when compared to pure HA.

3.3. Boron-doped HA as a scaffold

Since boron is an important trace element for bone metabolism, scaffolds including boron-doped HA were studied in order to observe its effects on bone repair. Tuncay et al. [28] coated boron-doped HA by using the microwave-assisted biomimetic method on a chitosan scaffold prepared by freeze-drying. The porosity of the boron-doped HA/chitosan scaffold was around 85.7%. No significant reduction in porosity of the scaffold was observed due to boron-doped HA coating. By using a similar synthesis method for boron-doped HA, a scaffold consisting of poly(butylenes adipate-co-terephthalate) and 5 wt.% of boron-doped HA was produced [35]. It was detected that boron doping increased fiber diameter by decreasing pore size. In another study, a bacterial cellulose/boron-doped HA/gelatin scaffold was produced by lyophilization technique [27]. A pore size between 45 to 210 µm was achieved. The pore size was in the range of 100 and 350 µm which was asserted as ideal pore size for tissue ingrowth.

3.4. Effect of Boron on microstructural characteristics of HA

Microstructural characteristics of boron-doped HA were investigated in terms of phase composition, crystallinity, lattice parameters, and functional groups in the structure.

3.4.1. Phase composition and crystallinity

The phase composition of HA ceramics is one of the most important properties because it has a determining effect on their biocompatibility, bioactivity, and mechanical characteristics. Phase transformations can occur due to the heat treatments applied during solid-state synthesis of boron-doped HA. For example, after heat treatment at 700°C for 24h, $CaCO_3$, $Ca_3(BO_3)_2$, CaO and β-TCP phases appeared in the system [23]. However, sintering at 1000°C for 24h resulted in X-ray diffraction (XRD) peaks that are only related to the apatite space group of $P6_3/m$ since the reaction is complete. Besides, β-TCP phase was detected at above 700°C in samples synthesized with wet precipitation method due to the thermal decomposition of HA [30]. Boron incorporation into HA occurred at above 900°C via the chemical reaction between HA and $B(OH)_3$ and β-TCP appeared as a second phase.

The phase transformation from β-TCP to α-TCP was detected at above 1200°C. In another study, boron-doped HA samples with 9.1 mol % boron synthesized by solid-state reaction and heated up to 1200°C for 6 h, a trace amount of CaO and α-TCP phases were detected [25]. The increase in borate content in co-precipitation of borate with HA resulted in the formation of different calcium metaborates such as $CaO{\cdot}B_2O_3$ (CaB_2O_4), $2CaO{\cdot}B_2O_3$($Ca_2B_2O_5$) and $3CaO{\cdot}B_2O_3$($Ca_3B_2O_6$) after calcination at 850°C [15]. It was also stated that calcination improved the crystallinity of HA without any mass loss of immobilized boron species. When wet and dry production methods were compared, wet precipitation method yielded less crystalline products. The XRD peaks in samples synthesized with wet precipitation were broadened as boron addition was increased [24,25]. However, no significant change in crystallinity was observed with the addition of boron in samples synthesized with solid-state reaction [24].

Another important factor for the formation of different phases was the P/B ratio. It was determined that a complete apatitic structure was formed at P/B=7.22 while $Ca_3(BO_3)_2$ was observed below this value [23]. At P/B=11, the phases detected were biphasic borohydroxyapatite, and $Ca(OH)_2$ and boron incorporation was limited to a ratio of P/B=7.22. $Ca_3(BO_3)_2$ and CaO phases occurred above P/B=7.22 [23]. Biphasic calcium phosphate samples consisting of HA and β-TCP were obtained by addition of boron with approximate amounts between 0.5 and 2 wt.% after sintering at 1000°C, 1100°C and 1200°C for 2h [36]. It was detected that as boron content increased from 0 to 2 wt.%, the amount of HA phase decreased from 85 to 69.7 wt.% and the remaining phase was β-TCP. Similarly, the percentage of HA phase decreased as the sintering temperature increased from 1000°C to 1200°C while keeping the amount of boron constant.

3.4.2. Lattice parameters

The process of removing borate by co-precipitation with HA by using $Ca(OH)_2$ results in the formation of boron-doped HA. As the boron content increased in the calcined product, the lattice parameter *a* decreased, and the lattice parameter *c* increased up to a point where the amount of boron was 1.41 mmol/g [15]. Since the decrease in *a* was more dramatic than the increase in *c*, the unit cell volume showed a decreasing trend. Calcination at 850°C resulted in dehydration of borate and the formation of BO_2 trigonal structure which increased lattice parameter *c* and decreased lattice parameter *a*. When boron content was further increased, the lattice parameters *a* and *c* in boron-doped HA gradually approached the values of pure HA due to the formation of calcium borate compounds as secondary phases.

Table 2 lists the changes in lattice parameters and unit cell volumes based on the amount of boron added to HA. When wet precipitation and solid-state reaction methods were compared in terms of lattice parameters of boron-doped HA obtained, wet precipitation method yielded products with no significant difference with HA [24]. However, the lattice parameter *a* decreased and the lattice parameter *c* increased with boron addition in samples synthesized with solid-state reaction. Moreover, Barheine et al. stated that *a* slightly decreased and *c* slightly increased with the increased amount of boron in samples synthesized by solid-state reaction [25]. However, due to the formation of trace amounts of CaO and α-TCP as second phases, the lattice parameter a did not follow *a* linear relationship.

3.4.3. Functional groups

The functional groups of boron-doped HA as detected by Fourier transform infrared (FTIR) spectroscopy analysis are summarized in Table 3. Small shifts in IR bands were observed according to some factors such as the amount of boron and the synthesis method.

Some of the bands were detected due to impurity phases in the structure such as $Ca_3(BO_3)_2$ and $Ca(OH)_2$. Bands detected at 717 (ν_2), 794 (ν_2), 903 (ν_1), 1228-1229 (ν_3) and 1280 (ν_3) cm^{-1} were assigned to BO_3^{3-} in $Ca_3(BO_3)_2$.

3.5. Effect of Boron on biological properties of HA

Boron addition increased in vitro biodegradability of HA and boron-doped HA reported to degrade quicker than β-TCP. Moreover, apatite forming ability in SBF was improved with boron addition [25].

Table 2. Lattice parameters and unit cell volume of boron-doped HA.

Production method	Nominal composition Ca/P+B molar ratio	Boron content[a)]	Lattice parameter *a* (Å)	Lattice parameter *c* (Å)	Unit cell volume ($Å^3$)
Solid-state reaction [23]	1.665	x=0.2	9.413	6.888	528.5
	1.664	x=0.3	9.409	6.893	528.4
	1.638	x=0.5	9.399	6.900	527.9
Solid-state reaction [25]	1.67	B/P=0.091	9.389	6.904	527.1
	1.54	B/P=0.182	9.389	6.927	528.8
	1.50	B/P=0.091	9.400	6.917	529.3

[a)] where x is the amount of borate (BO_3) substituted in HA structure

Table 3. FTIR bands detected for the boron-doped HA.

Functional groups	Vibration mode	Wavenumbers (cm^{-1})	Ref
PO$_4^{2-}$	ν$_2$	472	[37]
BO$_3^{3-}$	ν$_4$	571	[23]
		616	
PO$_4^{2-}$	ν$_4$	600-603	[23, 25, 34]
OH$^-$	librational	630	[23]
BO$_3^{3-}$	ν$_2$	743-744	[23, 25, 26, 34, 37]
		755	
		770-772	
		782-784	
PO$_4^{2-}$	ν$_1$	960- 963	[23, 26, 34, 37]
PO$_4^{2-}$	ν$_3$	1040-1050	[23, 25, 26, 34]
		1090-1100	
BO$_3^{3-}$	ν$_3$	1204-1208	[23, 25, 26, 34, 37]
		1250-1253	
		1304	
		1312	
BO$_2^-$	ν$_3$	1930-1933	[23, 25, 34]
		2002-2005	
OH$^-$	stretching	3570	[23]

Osteoinductive property of bone tissue engineering scaffolds with boron-substituted HA, which was synthesized by the biomimetic method and containing 1.15 wt.% boron, was studied previously [38]. The chitosan hydrogel scaffolds with boron-doped HA claimed to have higher mineralized matrix formation rates when compared to the scaffolds with bone-like HA precipitated in SBF. In another study about the effect of nano boron-doped HA on the adhesion, proliferation, and differentiation of human bone marrow-derived mesenchymal stem cells (MSC), boron addition was found to enhance cell adhesion and proliferation [39]. On the other hand, no change was observed in adipogenic or osteogenic differentiation of MSCs cultured with nano-sized pure HA and boron-doped HA with the molecular formula of Ca$_{10}$(PO$_4$)$_5$·8(BO$_4$)$_{0.2}$(OH)$_{1.6}$.

When compared with scaffolds containing only gelatine and bacterial cellulose, the addition of boron-doped HA to the scaffold composition, in which the ratio of boron-doped HA/gelatin was 1/5 wt./wt., slightly decreased the degradation rate after 4 weeks in phosphate buffered saline (PBS) solution [27]. Boron-doped HA, which was coated on chitosan by using the biomimetic method, significantly increased the proliferation of MC3T3-E1 osteoblastic cells on the 5th and 7th days of culture compared to pure chitosan [28]. Gene expression related to collagen type I as a marker of the initial stage of differentiation increased significantly on boron-doped HA/ chitosan scaffold on day 14. Late-stage differentiation marker osteocalcin, which is related to the mineralization, was measured the highest for boron-doped HA/ chitosan sample. Other differentiation markers, such as RunX2 and osteopontin gene expression, showed no significant differences on both HA/chitosan scaffold and boron-doped HA/chitosan scaffold [28]. Moreover, nanometer-sized boron-doped HA affected Saos-2 human osteosarcoma cells' Wnt and transforming growth factor-β (TGF-β) signaling pathways, which have a crucial role to overcome cell stress, by releasing boron within 1h [40]. According to the results of ALP activity and intracellular calcium amount determination tests, boron-doped HA in gelatin/bacterial cellulose scaffolds increased osteogenic activity of Saos-2 cells significantly after 14 days in cell culture [27].

In poly(butylenes adipate-co-terephthalate) (PBAT)/ boron-doped HA composite scaffold, although all scaffolds improved attachment and proliferation, an enhancement in the differentiation of human bone MSCs was observed for scaffolds containing boron-doped HA when compared to scaffolds with pure HA [35]. The study on Saos-2 cell line also showed that the addition of boron-doped HA brought a proliferative effect to the scaffolds consisting of gelatin and bacterial cellulose [27]. Mitochondrial activity, lactate dehydrogenase activity, and DNA quantity of Wharton's jelly-derived MSCs were not affected by boron substitution into the structure of HA [24].

3.6. Effect of Boron on thermal properties of HA

There is a very limited number of studies that directly examine how boron affects the thermal properties of HA. Thermogravimetric analysis was previously performed on the scaffolds consisting of bacterial cellulose, gelatin, and boron-doped HA [27]. When the samples were compared with pure HA, the samples included boron-doped HA had higher thermal stability after heating above 200°C. Moreover, the total mass loss of boron-doped HA was approximately 0.81%, whereas it was detected as 1.89% for HA. According to differential scanning calorimetry (DSC) analysis, the evaporation temperature range of absorbed water increased from 100-150°C to 170-200°C with boron addition which claimed that water retention capability of the scaffolds increased.

3.7. Effect of Boron on mechanical properties of HA

Ion substitutions generally change the structural, mechanical, and biological properties of HA. Not only biocompatibility but also mechanical properties of HA biomaterial play a crucial role in fulfilling the desired task within the body. Suchanek et al. tested several sintering additives in HA, such as H_3BO_3, $CaCl_2$, KCl, and $Na_2Si_2O_5$, and they determined that the density of the HA decreased significantly with the addition of 5 wt.% H_3BO_3 after sintering at 1000°C and 1100°C for 2h [41]. The inhibition of densification in groups with reduced density was attributed to the inhomogeneous distribution of the additive and the larger particle size of the additive compared to sintered HA. However, according to scanning electron microscopy (SEM) results, no inhomogeneous distribution was observed for samples with 5 wt.% H_3BO_3. Moreover, transgranular fracture was observed in the samples that are sintered at 1000°C. Similarly, a gradual decrease in density was observed in 0.5, 1, and 2 wt.% boron-doped HA [37]. The density of pure HA, which was sintered at 1200°C, was measured as 2.92 g/cm^3 and decreased to 1.93 g/cm^3 with the addition of 2 wt.% boron. From the SEM images of the fractured pellets of samples synthesized using 0.5% boron by weight, it was observed that a denser structure was achieved with the increase of sintering temperature, as expected. The decrease in density with the increasing amount of boron was linked to voids formed in HA structure by boron substitution.

The effect of boron-doped HA on compressive strength and Young's Modulus was examined previously in the scaffolds consisting of bacterial cellulose, boron-doped HA, and gelatine [27]. Compressive strength increased from 75.3 MPa to 94.9 MPa with boron addition. On the other hand, Young's modulus decreased from 11.3 MPa to 10.0 MPa. According to the compression test results of 0.5, 1, and 2 wt.% boron-doped HA, compressive strength decreased from 39.5 MPa to 29.1 MPa with boron addition for samples sintered at 1000°C [37]. As sintering temperature increased to 1200°C, compressive strength values of 0.5 wt.% boron-doped HA samples highly improved and reached to 161.2 MPa [37].

Vicker's microhardness test was applied to samples doped with 0.5, 1, and 2 wt.% boron [37]. Vicker's microhardness values decreased drastically with boron addition. Increasing sintering temperature from 1000°C to 1200°C resulted in an improvement of approximately 16-fold as a maximum.

3.8. Co-doping of Boron and other ions in HA

Co-doping of boron with other ions, such as Ce^{3+} and Eu^{3+}, was studied for applications as phosphors in fluorescent lamps. Rare-earth ions showed suitable spectroscopic properties for use in lasers [42,43]. Two different cerium ion concentrations, namely 1 and 0.8 mol% Ce^{3+}, were added to HAs with 3.3% and 5.5% moles of boron, respectively. [42]. Nuclear magnetic resonance (NMR) studies revealed that boron increased disorder in the structure and resulted in shifts of wavelengths to longer values in laser-induced emission bands. Moreover, luminescence intensity increased due to the addition of boron. In another study, in which the photoluminescence excitation (PLE) spectra of boron introduced Ce^{3+}-doped HA was studied, the mechanism behind the increase in the intensity of blue emission was explained with a decrease in OH^- ions around Ce^{3+} ion due to boron substitution [44]. Ternane et al. also studied co-doping of 1 mol % Eu^{3+} and 5.5 mol % B^{3+} into HA and showed that boron substitution increased perturbations in luminescence features of Eu^{3+} [43].

Co-doping of Sr^{2+} and BO_3^{3-} into HA was carried out by both wet precipitation and solid-state reaction routes [24]. Inductively coupled plasma optical emission spectroscopy (ICP-OES) was used to detect the strontium and boron contents in the structure of HA. Wet precipitation yielded 0.22 mol boron and 0.52 mol strontium while the dry method was more efficient in terms of the incorporation of ions as the boron content was 0.92 mol and the amount of strontium was 0.88 mol. The comparison between the production methods revealed that BO_3^{3-} was located on the hydrated surface layer in the samples synthesized by wet precipitation method and only Sr^{2+} influenced the lattice parameters. On the other hand, in samples synthesized by solid-state reaction, lattice parameter c increased significantly whereas lattice parameter a increased less than that of only Sr^{2+}-doped HA which indicated the incorporation of BO_3^{3-} in the structure.

3.9. Effect of Boron on electrical properties of HA

The electrical properties of bioceramic materials are of great interest due to the increased biological response on the polarized surfaces. Like the structural properties of HA, its electrical properties can be improved by adding foreign cations [45]. The dielectric constant of boron-doped HA was investigated and a decrease in the electric dipole moment of OH^- ions, which were substituted by boron ions, was observed [26]. Oscillation due to electric field and polarization decreased which resulted in a decrease in the dielectric constant of HA. In terms of alternating electrical conductivity, boron addition enhanced the insulation properties of HA. Therefore, it can be proposed as a material for bioelectronics.

3.10. Future perspectives

There is a limited number of studies related to boron-doped HA as a candidate for biomedical applications. Researchers mainly focused on the elimination of boron from geothermal water by precipitation in the form of boron-doped HA and supportive effect of boron on luminescence properties of Ce^{3+} and Eu^{3+} doped HA. In terms of incorporation mechanism two sites were proposed (OH^-, PO_4^{3-} sites). No detailed information about the substitution mechanism at atomic level was found in the literature. Moreover, the information related to lattice parameters is very limited. Most of the limited number of studies concentrated on phase composition, FTIR studies and biological properties such as bioactivity in SBF, cell proliferation and differentiation. There is a literature gap in many topics, such as the anti-bacterial effect of boron-doped HA and the maximum amount of doping in terms of biological response. Since it was known that boron compounds has an antibacterial effect via direct contact or as a constituent of dental composites, boron-doped HA may be investigated in terms of its anti-bacterial properties as a biomaterial for dental applications [46,47].

Generally, boron-doped HA was used as a constituent of tissue engineering scaffolds. However, the use of boron-doped HA as a coating material or a constituent of a composite is not very common. As stated before, boron affects the biological functions of many organs, especially bone. Therefore, more biomaterial prototypes in the form of scaffolds and coating materials are needed to be studied. The number of *in vivo* studies performed on boron-doped HA should be increased since its positive effect on cell differentiation was known [38]. Boron was also used as a supplementary element for many organ metabolisms other than bone, like liver and brain. Therefore, boron-doped HA can be integrated into a system for drug delivery purposes.

4. Conclusion

In this review, the studies on boron-doped HA were summarized by focusing on biomedical applications. The synthesis methods were evaluated and the effects of boron doping on phase composition, crystallinity, lattice parameters, and functional groups were analyzed. The phase composition was dependent on the P/B ratio and heat treatment during synthesis. It was also noted that boron incorporation occurred after calcination at above 900ºC. The phases detected other than HA were CaO, $Ca_3(BO_3)_2$, β-TCP, α-TCP, and metaborates. In general, boron substitution decreased the lattice parameter *a* and increased the lattice parameter *c*. The unit cell volume decreased depending on the lattice parameter *a*. Crystallinity has been shown to be affected by the synthesis method, for example, crystallinity decreased with boron addition in wet precipitation method whereas no change in crystallinity was observed with boron addition in samples synthesized by solid-state reaction. There was also a difference in morphology between pure and boron-doped HA. Rod-like morphology was observed in boron-doped HA. Boron doping increased the thermal stability and insulation properties of HA. Biological properties of boron-doped HA have been studied relatively more extensively in the literature. Boron doping into HA was reported to increase biodegradability, apatite forming ability, cell proliferation, and osteogenic activities in general. However, cell proliferation and osteogenic activities can change based on the cell type. Boron addition decreased the density of HA due to the formation of voids in the structure. Moreover, Vicker's microhardness also decreased with boron substitution. The most studied forms of boron-doped HA in the biomedical field were listed as a constituent of a scaffold and a coating material on the titanium alloy (Ti6Al4V) substrates. There were no studies that utilized boron-doped HA in a drug delivery system although the supportive effect of boron on metabolic functions of bone, liver, and brain.

5. Conflict of interest

The authors declare no sources of support or conflict of interest.

References

[1] Avci M. , Yilmaz B., Tezcaner A., Evis Z., Strontium doped hydroxyapatite biomimetic coatings on Ti6Al4V plates, Ceram. Int., 43 (12), 9431-9436, 2017.

[2] Yilmaz B., Evis Z., Tezcaner A., Banerjee S., Surface characterization and biocompatibility of selenium-doped hydroxyapatite coating on titanium alloy, Int. J. Appl. Ceram. Technol., 13 (6), 1059-1068, 2016.

[3] Thian E. S., Huang J., Best S. M., Barber Z. H., Bonfield W., Novel silicon-doped hydroxyapatite (Si-HA) for biomedical coatings: An *in vitro* study using acellular simulated body fluid, J. Biomed. Mater. Res., 76B (2), 326-333, 2006.

[4] Tampieri A., Celotti G. C., Landi E., Sandri M., Magnesium doped hydroxyapatite: Synthesis and characterization, Key Eng. Mater., 264, 2051-2054, 2004.

[5] Ciobanu C. S., Iconaru S. L., Chifiriuc M. C., Costescu A., Le Coustumer P., Predoi D., Synthesis and antimicrobial activity of silver-doped hydroxyapatite nanoparticles, BioMed Res. Int., 2013, 1-10, 2013.

[6] Uysal I., Severcan F., Evis Z., Characterization by Fourier transform infrared spectroscopy of hydroxyapatite co-doped with zinc and fluoride, Ceram. Int., 39 (7), 7727-7733, 2013.

[7] Toker S. M., Tezcaner A., Evis Z., Microstructure, microhardness, and biocompatibility characteristics of yttrium hydroxyapatite doped with fluoride, J. Biomed. Mater. Res. Part B, 96 (2), 207-217, 2011.

[8] Alshemary A. Z., Pazarceviren A. E., Tezcaner A., Evis Z., Fe^{3+}/SeO_4^{2-} dual doped nano hydroxyapatite: A novel material for biomedical applications, J. Biomed. Mater. Res., 106 (1) 340-352, 2018.

[9] Samani S., Hossainalipour S. M., Tamizifar M., Rezaie H. R., In vitro antibacterial evaluation of sol-gel-derived Zn^{+2}, Ag^+, and (Zn^{+2} Ag^+)-doped hydroxyapatite coatings against methicillin-resistant Staphylococcus aureus, J. Biomed. Mater. Res. Part A, 101 (1), 222-230, 2013.

[10] Bodhak S., Bose S., Bandyopadhyay A., Influence of MgO, SrO, and ZnO dopants on electro-thermal polarization behavior and *in vitro* biological properties of hydroxyapatite ceramics: Electro-thermally polarized doped hydroxyapatite ceramics, J. Am. Ceram. Soc., 94 (4), 1281-1288, 2011.

[11] Sasaki K., Hayashi Y., Toshiyuki K., Guo B., Simultaneous immobilization of borate, arsenate, and silicate from geothermal water derived from mining activity by co-precipitation with hydroxyapatite, Chemosphere, 207, 139-146, 2018.

[12] Liu Y., Xue K., Yao S., Structure, degradation and hydroxyapatite conversion of B-doped 58S bioglass and glass-ceramics, J. Ceram. Soc. Jpn., 127 (4), 232-241, 2019.

[13] Choi W. W., Chen K. Y., Evaluation of boron removal by adsorption on solids, Environ. Sci. Technol., 13 (2), 189-196, 1979.

[14] Yoshikawa E., Sasaki A., Endo M., Removal of boron from wastewater by the hydroxyapatite formation reaction using acceleration effect of ammonia, J. Hazard. Mater., 237, 277-282, 2012.

[15] Sasaki K., Toshiyuki K., Guo B., Ideta K., Hayashi Y., Hirajima T., Miyawaki J., Calcination effect of borate-bearing hydroxyapatite on the mobility of borate, J. Hazard. Mater., 344, 90-97, 2018.

[16] Bose S., Fielding G., Tarafder S., Bandyopadhyay A., Trace element doping in calcium phosphate ceramics to understand osteogenesis and angiogenesis, Trends Biotechnol., 31 (10), 594-605, 2013.

[17] Abdelnour S. A., Abd El-Hack M. E., Swelum A. A., Perillo A., Losacco C., The vital roles of boron in animal health and production: A comprehensive review, J. Trace Elem. Med. Biol., 50, 296-304, 2018.

[18] Khaliq H., Juming Z., Ke-Mei P., The physiological role of boron on health, biol. Trace Elem. Res., 186, 31-51, 2018.

[19] Dzondo-Gadet M., Mayap-Nzietchueng R., Hess K., Nabet P., Belleville F., Dousset B., Action of boron at the molecular level, effects on transcription and translation in an acellular system, Biol. Trace Elem. Res., 85 (1), 23-33, 2002.

[20] Swager T. M., Luppino S. P., Nothing boring about this borylation, Synfacts, 11 (3), 0266-0266, 2015.

[21] Lakhkar N. J., Lee I. H., Kim H. W., Salih V., Wall I. B., Knowles J. C., Bone formation controlled by biologically relevant inorganic ions: Role and controlled delivery from phosphate-based glasses, Adv. Drug Delivery Rev., 65 (4), 405-420, 2013.

[22] Jakob F., Seefried L., Kitz C., Stich A., Sponholz B., Raab P., Ebert R., Nutritional Influences on Bone Health, Chap. 11: Trace Elements and Bone, Springer-Verlag London Limited, London, 2010.

[23] Ternane R., Cohen-Adad M. T., Panczer G., Goutaudier C., Kbir-Ariguib N., Trabelsi-Ayedi M., Florian P., Massiot D., Introduction of boron in hydroxyapatite: Synthesis and structural characterization, J. Alloys Compd., 333 (1-2), 62-71, 2002.

[24] Kolmas J., Velard F., Jaguszewska A., Lemaire F., Kerdjoudj H., Gangloff S. C., Ka A., Substitution of strontium and boron into hydroxyapatite crystals : Effect on physicochemical properties and biocompatibility with human Wharton-Jelly stem cells, Mater. Sci. Eng. C, 79, 638-646, 2017.

[25] Barheine S., Hayakawa S., Ja C., Shirosaki Y., Osaka A., Effect of disordered structure of boron-containing calcium phosphates on their *in vitro* biodegradability, J. Am. Chem. Soc., 94 (8), 2656-2662, 2011.

[26] Alhammad M. S., Nanostructure hydroxyapatite based ceramics by sol gel method, J. Alloys Compd., 661, 251-256, 2016.

[27] Atila D., Karataş A., Evcin A., Keskin D., Tezcaner A., Bacterial cellulose-reinforced boron-doped hydroxyapatite/gelatin scaffolds for bone tissue engineering, Cellulose, 26, 9765-9785, 2019.

[28] Tuncay E., Demirtaş T. T., Gümüşderelioğlu M., Microwave-induced production of boron-doped HAp (B-HAp) and B-HAp coated composite scaffolds, J. Trace Elem. Med. Biol., 40, 72-81, 2017.

[29] Nakamura M., Zhuang Z., Aizawa M., Fabrications of boron-containing apatite ceramics via ultrasonic spray-pyrolysis route and their surface properties, Key Eng. Mater., 529-530, 109-113, 2012.

[30] Satoshi H., Akihito S., Tsuru K., Osaka A., Fujii E., Kawabata K., Jaeger C., Preparation and Characterization of Boron-Containing Hydroxyapatite, Key Eng. Mater., 361-363, 191-194, 2007.

[31] Sasaki K., Toshiyuki K., Ideta K., Miki H., Hirajima T., Miyawaki J., Murayama M., et al., Removal mechanism of high concentration borate by co-precipitation with hydroxyapatite, J. Environ. Chem. Eng., 4 (1), 1092-1101, 2016.

[32] Ke D., Vu A. A., Bandyopadhyay A., Bose S., Compositionally graded doped hydroxyapatite coating on titanium using laser and plasma spray deposition for bone implants, Acta Biomater., 84, 414-423, 2019.

[33] Cao J., Lian R., Jiang X., Magnesium and fluoride doped hydroxyapatite coatings grown by pulsed laser deposition for promoting titanium implant cytocompatibility, Appl. Surf. Sci., 515, 146069, 2020.

[34] Evcin A., Buyukleblebici B., Ti6A14V coating with B_2O_3 and Al_2O_3 containing hydroxyapatite by HVOF technique, Sci. Iran., 26,1980-1989, 2019.

[35] Arslan A., Çakmak S., Gümüşderelioğlu M., Enhanced osteogenic activity with boron-doped nanohydroxyapatite-loaded poly(butylene adipate-co-terephthalate) fibrous 3D matrix, Artif. Cells Nanomed. Biotechnol., 46, 790-799, 2018.

[36] Albayrak O., Materials characterization structural and mechanical characterization of boron doped biphasic calcium phosphate produced by wet chemical method and subsequent thermal treatment, Mater. Charact., 113, 82-89, 2016.

[37] Albayrak Ö., Uğurlu M., Bor katkili hidroksiapatit üretimi ve karakterizasyonu: Bor orani ve sinterleme sicakliğinin yapi ve mekanik özellikler üzerindeki etkisi, Journal of the Faculty of Engineering and Architecture of Gazi University, 31(3), 749-761, 2016.

[38] Calis M., Demirtas T. T., Vatansever A., Irmak G., Sakarya A. H., Atilla P., Ozgur F., et al., A Biomimetic alternative to synthetic hydroxyapatite: “Boron-containing bone-like hydroxyapatite” precipitated from simulated body fluid, Ann. of Plast. Surg., 79 (3), 304-311, 2017.

[39] Ciftci E., Sevil K., Korkusuz P., Timuçin M., Korkusuz F., Boron containing nano hydroxyapatites (B-n-HAp) stimulate mesenchymal stem cell adhesion, proliferation and differentiation, Key Eng. Mater., 631, 373-378, 2014.

[40] Gizer M., Kose S., Karaosmanoglu B., Taskiran E. Z., Berkkan A., Timucin M., Korkusuz F., et al., The effect of boron-containing nano-hydroxyapatite on bone cells, Biol. Trace Elem. Res., 193, 364-376, 2020.

[41] Suchanek W., Yashima M., Kakihana M., Yoshimura M., Hydroxyapatite ceramics with selected sintering additives, Biomaterials, 18 (13), 923-933, 1997.

[42] Ternane R., Cohen-Adad M. T., Panczer G., Goutaudier C., Dujardin C., Boulon G., Kbir-Ariguib N., et al., Structural and luminescent properties of new Ce^{3+} doped calcium borophosphate with apatite structure, Solid State Sci., 4 (1), 53-59, 2002.

[43] Ternane R., Panczer G., Cohen-Adad M. T., Goutaudier C., Boulon G., Kbir-Ariguib N., Trabelsi-Ayedi M., Relationships between structural and luminescence properties in Eu^{3+}-doped new calcium borohydroxyapatite, Opt. Mater., 16 (1-2), 291-300, 2001.

[44] Zhang X., Zhang J., Ma W., Liao S., Zhang X., Wang Z., Yu L., et al., From nonluminescence to bright blue emission: Boron-induced highly efficient Ce^{3+}-doped hydroxyapatite phosphor, Inorg. Chem., 58 (19), 13481-13491, 2019.

[45] Al-Hazmi F. E., Synthesis and electrical properties of Bi doped hydroxyapatite ceramics, J. Alloys Compd., 665, 119-123, 2016.

[46] Demirci S., Kaya M. S., Doğan A., Kalay Ş., Antibacterial and cytotoxic properties of boron-containing dental composite, Turk. J. Biol., 39, 417-426, 2015.

[47] Sayin Z., Ucan U. S., Sakmanoglu A., Antibacterial and antibiofilm effects of boron on different bacteria, Biol. Trace Elem. Res., 173 (1), 241-246, 2016.